Squeezed and Entangled Light:
From Foundations of Quantum Mechanics
to Quantum Sensing

Dissertation
zur Erlangung des Doktorgrades
an der Fakultät für Mathematik, Informatik, und Naturwissenschaften
Fachbereich Physik
der Universität Hamburg

vorgelegt von

M.Sc. Jascha Zander

Hamburg 2021

Gutachter/innen der Dissertation:	Prof. Dr. Henning Moritz
	Prof. Dr. Roman Schnabel
Zusammensetzung der Prüfungskommission:	Prof. Dr. Roman Schnabel
	Prof. Dr. Henning Moritz
	Prof. Dr. Michael Rübhausen
	Prof. Dr. Oliver Gerberding
	Prof. Dr. Ludwig Mathey
Vorsitzende/r der Prüfungskomission:	Prof. Dr. Michael Rübhausen
Datum der Disputation:	01.04.2021
Vorsitzender Fach-Promotionsausschusses PHYSIK:	Prof. Dr. Wolfgang Hansen
Leiter des Fachbereichs PHYSIK:	Prof. Dr. Günter H. W. Sigl
Dekan der Fakultät MIN:	Prof. Dr. Heinrich Graener

Disclaimer

Throughout the thesis, I use different pronounces to describe the results. When I use “we” or “our” (as in “we obtained the result”), it is to acknowledge that this result was obtained in collaboration with other authors. Correspondingly, whenever I use “I” in the context of accomplished experiments, it is to highlight, I am the only person bearing the full responsibility for any mistakes in the statements, acquiring the data, or the data evaluation. In some cases, in a descriptive context, where no new insights are presented, I use “we”, assuming it to be “the reader and me”.

Abstract

Squeezed and entangled states have proven to be valuable resources in optical quantum sensing and pushing forward measurement sensitivities. However, their potential is not yet fully explored.

In the first part of my thesis, I show the experimental quantum enhancement of a squeezed light operated Mach-Zehnder interferometer. I measured a non-classical sensitivity improvement of more than a factor of ten, corresponding to (10.5 ± 0.1) dB, which is the equivalent of a 11.2-fold increase in coherent light power.

Further, my thesis proposes a novel concept on direct absorption (loss) measurements within the Mach-Zehnder topology. The technique uses quantum correlated bipartite squeezed light beams to measure the transmission through a sample placed in one arm of the Mach-Zehnder interferometer. My proof-of-principle experiment demonstrates, that the loss is independent of the used photodiodes' quantum efficiency. Beyond that, the concept may become a powerful tool for optical measurements in biosensing with integrated quantum photonic devices. Light-sensitive samples are particularly vulnerable to high powers under illumination by bright light, and such measurements will benefit from the extremely low intensity of squeezed light.

In the second part of my thesis, I demonstrate how to surmount quantum uncertainty in sensing dynamical systems. For the first time, a phase space trajectory with sub-Heisenberg indeterminacy with respect to an entangled quantum reference is realized. The time evolution is unconditionally monitored with a precision ten times higher than any quantum mechanical system without correlations. I measured the phase and amplitude quadrature simultaneously with a remaining indeterminacy of $\Delta X(t)\Delta Y(t) \approx 0.1\hbar/2$. The result supports quantum technologies for entanglement-enhanced sensors and substantiates an enhanced physical description of quantum uncertainty relations. From this perspective, I revisit Heisenberg's uncertainty relation and conclude that it sets a lower bound to the indeterminacy of two conjugate observables with respect to a reference system that has been coupled to the environment.

Kurzfassung

Gequetschte und verschränkte Lichtzustände haben sich auf dem Gebiet der optischen Sensorik als wichtige Resourcen erwiesen. Dennoch ist ihr Potential nicht vollständig erforscht.

Im ersten Teil meiner Arbeit, zeige ich experimentell die Quantenverbesserung durch ein mit gequetschtem Licht betriebenes Mach-Zehnder Interferometer. Ich habe eine nicht-klassische Verbesserung von (10.5±0.1) dB erreicht, welches einer 11.2-fachen Erhöhung der Lichtleistung entspricht.

Im weiteren wird in meiner Arbeit ein neuartiges Konzept zur Absorptionsmessung (bzw. Verlustmessung) im Rahmen der Mach-Zehnder Topologie vorgeschlagen. Das Prinzip basiert auf der Korrelation zwischen den gequetschten Lichtzuständen in den beiden Armen des Interferometers. Diese wird ausgenutzt, um die Transmission durch eine Probe in einem der beiden Armen zu messen. Zum Beweis der zugrundeliegenden Idee habe ich ein Experiment durchgeführt, bei dem gezeigt wird, dass die Absorption unabhängig von der Quanteneffizienz der verwendeten Photodioden ist. Darüber hinaus kann dieses Konzept als ein wirkungsvolles Instrument im Bereich der Biosensorik in optischen Messungen mit integrierten photonischen Bauelementen eingesetzt werden. Insbesondere betrifft das solche Messungen, bei denen Proben, die äußerst empfindlich auf starke Beleuchtung mit hoher Lichtleistung reagieren, von der sehr niedrigen Intensität des gequetschten Lichtes profitieren.

Im zweiten Teil meiner Arbeit zeige ich, wie die Quantenunschärfe bei der Erfassung von dynamischen Systemen überwunden werden kann. Zum ersten mal wurde eine Trajektorie mit einer sub-Heisenberg Unbestimmtheit, in Bezug zu einer verschränkten Quantenreferenz, realisiert. Die zeitliche Entwicklung wurde ohne vorherige Informationen direkt beobachtet, die zudem eine zehnmal höhere Präzision erreichte im Vergleich zu einem quantenmechanischen System ohne Korrelationen. Ich habe die Phasen- und Amplituden-Quadraturen mit einer verbleibenden Unbestimmtheit von $\Delta X(t)\Delta Y(t) \approx 0.1\,\hbar/2$ gleichzeitig gemessen. Dieses Ergebnis eröffnet nicht nur neue Wege zur Anwendung von Quantentechnologien mit verschränkungsbasierten Sensoren, sondern bestärkt eine erweiterte physikalische Beschreibung von quantenmechanischen Unschärferelationen. Aus dieser Perspektive heraus reflektiere ich die Heisenbergsche Unschärferelation und schließe daraus, dass sie eine untere Grenze der Unbestimmtheit zweier konjugierter Observablen in Bezug zu einem Referenzsystem setzt, dass an die Umgebung gekoppelt ist.

Contents

1. Introduction

The existence of the Heisenberg uncertainty relation (HUR) is one of the most distinctive features of quantum mechanics that mark a sharp line to classical physics. The idea of a characteristic *uncertainty* between the accuracy of the position measurement of a particle and its momentum was introduced by Heisenberg in an article 1927, in which he concludes: "the more precisely the position is determined, the less precisely the momentum is known, and vise versa" [1]. In his line of argumentation, he illustrates the approach along with the detection of an electron observed with an optical microscope. In accordance with the Abbe diffraction limit [2], the electron's interaction with the illuminating light of a sufficiently short wavelength λ will define the accuracy of the position observed by the microscope, that is $\delta q \sim \lambda$. In addition, the electron will undergo an unavoidable Compton recoil, which involves a disturbance in the momentum of magnitude $\delta p \sim h/\lambda$. From this more heuristic derivation, Heisenberg formulated a limit of measurement imprecision, what was later phrased as *the uncertainty principle* and is dictated by the product of imprecisions to be ideally of the order of Planck's constant

$$\delta q \delta p \sim h. \tag{1.1}$$

Here δq and δp are merely remarked as 'approximately the average error' of the position q and the momentum p of the electron. As announced in the seminal paper, Heisenberg intended to provide an intuitive picture of the new matrix mechanics, which postulated that the canonical position and momentum variables are represented by infinite self-adjoint matrices **Q** and **P**, and considered it in particular as clear evidence of the fundamental commutation rule **QP - PQ** = i$\hbar$ of the new quantum formalism [3, 4]. However, a precise mathematical definition of the quantities was not given.

A few months later, after Heisenberg presented the vague concept of an indeterminacy relation, the general idea was mathematically confirmed by Kennard [5] and independently by Weyl [6], who proofed the theorem for any normalized state vector $|\Psi\rangle$. In the elaborated formulation, the quantities δq and δp are substituted by the precise defined standard deviation Δq and Δp of the position and momentum that possesses the inequality:

$$\Delta q \Delta p \geq \hbar/2. \tag{1.2}$$

This is the modern version of the uncertainty relation, and most familiar standard expression introduced in textbooks today or taught in beginner courses on quantum mechanics. A generalization for any pair of observables was derived by Robertson [7] and Schrödinger [8], while their more general expression reduces to the inequality 1.2 as mentioned above for canonical conjugate pairs.

When designing precision experiments that are dominated by quantum uncertainties, scientist go into a moment of quiet pondering about what the Heisenberg uncertainty relation allows to do and what not. Particularly concerning the experimental requirements, it is a common consensus to distinguish between different uncertainty relations (although they have the same origin), to adequately capture a set of 'dos' and 'don'ts' that defines the technical preconditions we have to fulfill for applications in quantum metrology. Also, it is motivated by the fact that an increasing number of experiments reach sensitivities of the detection process that is limited by fundamental quantum noise which confines the performance of current measurement apparatus.

The modern version of Heisenberg's uncertainty relation is undisputed and refers to the intrinsic uncertainty as an inherent part of any quantum state that is independent of performing a measurement on it or not; this is sometimes denoted as *preparation uncertainty*. Usually, measurements are performed on an ensemble of individual but identical systems prepared in the same initial state. If no interaction with a thermal bath occurs before detection, repeated measurement of position, energy, or angular momentum results in different quantum system eigenvalues characterized by probability density functions. In practice, if we obtain a deviation of the position Δq

close to zero, the deviation of the conjugate variable, the momentum Δp, has to be a very large value. Mathematically, this results from the Fourier transformation that connects the spaces of conjugate observables, such as the position and momentum space, in combination with quantization [9]. If one quantity is precisely determined, the other is undetermined and vice versa.

Nevertheless, there are existing effects related to Heisenberg's original formulation we have to be aware of. In the recent decades the original formulation is revisited in terms of measurement and the disturbance it must create in connection to continuous monitoring of a single quantum system [10]. Therefore, when we attempt to observe the phase space trajectory of the electron, this effectively comprises a joint measurement of position and momentum. As a consequence, a trade-off between the inaccuracies of both quantities is necessary, satisfying a *Measurement-Disturbance-Relation* and giving rise to its best balance at the *Standard Quantum Limit* [11]. Therefore it is widely accepted that the detection apparatus causes unpredictable perturbations on the system being measured and influences later measurements that exclude assigning arbitrary precise information to a pair of canonical conjugate quantities simultaneously for all times t.

In the first instance, it may therefore come at a surprise that quantum uncertainties in sensing of phase space displacements can in principle be fully avoided. A. Einstein, B. Podolsky, and N. Rosen (EPR) were puzzled by this in 1935 and conjectured on the assumption of 'local realism' that the quantum theory does not provide a complete description of the actual reality [12]. The Bell inequalities clarify the discussion on the EPR argument with correlated systems [13]. They predict that any 'local hidden variables theory' must result in a special type of inequality for the measurement outcomes. The existence of such theories was excluded by Aspect et al. in 1982 by demonstrating a violation of these inequalities [14].

Indeed, it is a well-known fact that the commutator of the difference and the sum of non-commuting observables of two quantum systems A and B is zero, from which follows that such a sum and difference (or vice versa) are simultaneously determined precisely without a limitation by a Heisenberg uncertainty relation, as pointed out by E. Schrödinger [15]. Employing the lack of indeterminism of phase space sensing, however, requires entanglement between two subsystems A and B.

This was theoretically reformulated in the framework of quantum estimation theory by G. D'Ariano et al. [16].

From this perspective I will remark on two important subtle aspects:

1. It is not necessary that both quantities Δq and Δp are equally balanced. Thus there is no limit to which we can resolve the position of the electron (or any physical system) at any specific instance of time, since $\Delta q \rightarrow 0$ and $\Delta p \rightarrow \infty$.

2. Such quantities of the electron can be simultaneously determined arbitrary precisely with respect to another quantum system at any time t, which indeed allows us to observe phase space trajectories without being disturbed by the measurement apparatus.

Squeezing and EPR-Entanglement of field quadratures

To examine (simultaneous) measurements of canonical conjugate variables in quantum optics we consider the momentum and position-like quadratures of the quantized electromagnetic light field. They are the dimensionless field amplitudes at phases $90°$ apart from each other, usually defined as the amplitude quadrature amplitude $\hat{X}$ and the phase quadrature amplitude $\hat{Y}$.

The eigenvalue spectra are represented by a Gaussian distributions. The ground state, coherent states and (pure) squeezed states minimize the product of the standard deviation and achieve equality of equation 1.2.

A well-established method to reduce the uncertainty of a single quantity is to utilize non-classical states to 'squeeze' the imprecision, e.g. in the amplitude quadrature below its zero-point-fluctuation, which implies an increase in the orthogonal phase quadrature. This leads to an arbitrarily precisely defined amplitude at a certain time, while the phase is entirely undefined at the same moment. Hence, in this way we are able to prepare the initial state with a well-defined value for all times t in one quadrature. The first experiments producing squeezed light were performed in 1985 by Slusher et. al. [17] using four wave mixing in sodium atoms in an optical cavity and only a few months later by degenerated parametric down-conversion in a second order non-linear crystal [18]. Ever since the technical progress in 'cavity-enhanced optical-parametric amplification (OPA)' induces modern direct

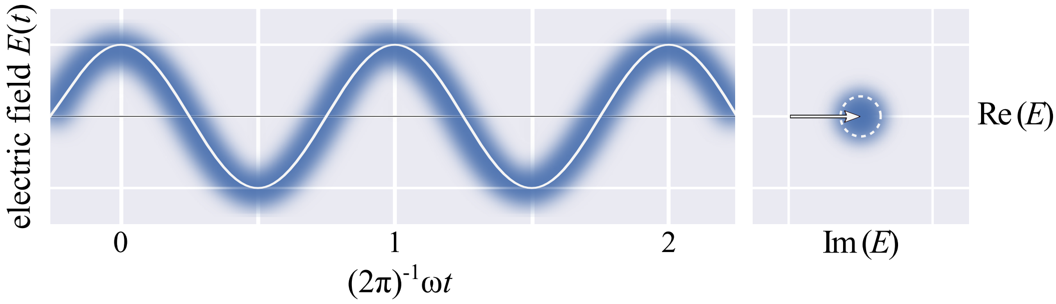

Figure 1.1.: Quasi-monochromatic oscillations of an electrical field and its phase space representation. Left: electric field $\hat{E}(t) = [E + \hat{X}]\cos\omega t + \hat{Y}\sin\omega t$ as function of time. Classically, the field amplitude E can be precisely determined at each instant of time (solid curve). The Heisenberg uncertainty relation, however, limits the measurement precision of amplitude and phase and shows uncertainty (blurred blue area). Right: uncertainty in the phase space in rotating frame at frequency ω. The white arrow indicates the classical amplitude E; the dashed white circle encloses the zero-point-fluctuations of the quadrature $\hat{X}$ and $\hat{Y}$.

observation of squeeze factors of more than 10 dB in many experiments [19–22]. Squeezed states of light are a powerful resource in application for laser interferometers and contribute significantly to the field of gravitational wave astronomy [23–27]. This is impressively demonstrated after upgrading the gravitational wave detectors (GWD) AdvancedLIGO and AdvancedVIRGO and starting the third observation run (O3). Since April 2019 both detectors observe gravitational wave signals with an improved sensitivity due to squeezed light. The quantum enhancement increase the observatories' detection rates by as much as 50 %, allowing to detect a new gravitational wave event nearly every week [28, 29]. Apart from its most prominent application in GWD we are coming to more compact experiments also endemic with quantum noise. As reported in [30], squeezed light can be used to improve the sensitivity in photo-sensitive measurements of biological probes using coherent light to track micro particles. In those cases, increasing the light power to enhance the signal-to-noise ratio is not possible since the investigated samples would be partially or completely destroyed. Likewise, probing the spatiodynamics of molecular bonds with stimulated Raman-spectroscopy relies on low laser intensities [31]. Furthermore, developments in the field of quantum information requires strong non-classical correlations between two or more parties, that can be attained with quadrature entangled states revealing strong EPR-entanglement [32]. Many experiments take advantage of generating entanglement by superimposing two orthogonal squeezed vacuum states. In particular, secure communication by distributing quantum keys (QKD)[33, 34], its application in quantum memories [35, 36] or entanglement distillation [37, 38].

Although all of the previous experiments perform measurements utilizing quantum correlations, the role of Heisenberg's uncertainty relation remains a subject of discussions to date. The scope of this thesis is focusing on restrictions in quantum measurements demanded by quantum formalism. The motivation is to provide an intuitive physical picture on quantum uncertainty in sensing and to demonstrate this on the basis of non-classical approaches, like quadrature EPR-entangled states, which provide an improvement upon the precision of current classical measurement techniques in metrology.

Structure of this thesis

The thesis is divided into the following parts:

Chapter 2 is a theoretical description of the quantization of light and Gaussian wave optics.

Chapter 3 describes the experimental techniques for sensing, which are used throughout this thesis.

Chapter 4 presents the experimental results of a 10 dB non-classical improvement of the phase sensitivity in a Mach-Zehnder interferometer using a vacuum squeezed state.

Chapter 5 demonstrates a novel concept on direct absorption measurements, exploiting the correlation of bipartite squeezed vacuum states in the two arms of a Mach-Zehnder interferometer.

Chapter 6 proves the principle that the dynamics of phase space trajectories can be monitored without quantum uncertainty. Moreover it provides a graphical illustration of the field quadratures to promote an elaborated statement of the Heisenberg uncertainty relation.

Chapter 7 gives a conclusion and summary about the aforementioned experimental results of the thesis.

2. Quantum States of Light

Usually performing highly sensitive measurements on a quantum system in quantum sensing experiments with continuous-variable optical fields requires squeezed and entangled states of light. Their properties can only be explained on the basis of a purely quantum mechanical description. As a consequence, the optical fields show quantum uncertainties and thus quantum noise. These are described by Gaussian statistics. The corresponding operators of those physical systems are called the '*amplitude quadrature amplitude* $\hat{X}$' and the '*phase quadrature amplitude* $\hat{Y}$'. Although these are associated to the system's wave property, the detection process of the measured observables features the quantized interaction of photons and electron particles. Since the optical frequency ω is typically on the order of 10^{14} Hz, it is not possible to measure the eigenvalues of the quantities directly. Instead, any measurement of $\hat{X}$ or $\hat{Y}$ is related to a modulation mode at angular frequency Ω of the optical field around the central frequency ω_0; thus $\omega = \omega_0 \pm \Omega$. The classical analogy is that the optical field carry amplitude and phase modulation with angular modulation frequency Ω measured over the frequency band $\Delta\Omega$.

The following chapter introduces briefly the concept of quadrature fields, which actually suffice to define the properties of the physical system that is characterized. As it remains the primary focus as a subject of this thesis, squeezing and entanglement of quadrature fields are introduced. This chapter is mainly based on the book [39] and the review article [24]. Initially, the principle of modulation theory in the two-photon formalism for the quantized field as developed by C. Caves and B. Schumaker [40, 41] will be introduced.

2.1. Quantization of the electric field

The quantization of the classical electro-magnetic field can be rewritten by replacing the electric and magnetic field components by its operator representation, e.g. $\hat{E}(\vec{r},t)$ and $\hat{B}(\vec{r},t)$. In further treatment, the magnetic field is neglected. This is justified by our experiments' focus on the electric field properties, which are measured in the photo-electric detection process. For ease of notation the explicit spatial dependence will be omitted and we concentrate on a fixed point in space. The quantum mechanical electric field operator can be decomposed as the sum of positive and negative Fourier frequencies and takes the form

$$\begin{aligned} \hat{E}(t) &= \hat{E}^{+}(t) + \hat{E}^{-}(t) \\ &= \sqrt{\frac{2\pi\hbar}{\mathcal{A}c}} \int_0^\infty \sqrt{\omega}\left(\hat{a}_\omega e^{-i\omega t} + \hat{a}_\omega^\dagger e^{i\omega t}\right) \frac{d\omega}{2\pi}, \end{aligned} \tag{2.1}$$

where the (+) indicates the positive and (-) indicates the negative frequency part of the mode. Here $\mathcal{A}$ is the effective cross section area of the beam, c is the speed of light in vacuum and $\hbar$ the reduced Planck constant. Also introduced are the annihilation operator $\hat{a}_\omega$ and the creation operator $\hat{a}_\omega^\dagger$. Notice that these operators are given in the Heisenberg picture, determined by the explicit time dependence factored out by the $e^{i\omega t}$ term. These operators obey the commutation relations

$$[\hat{a}_\omega, \hat{a}_{\omega'}] = 0, \text{ and } \quad [\hat{a}_\omega, \hat{a}_{\omega'}^\dagger] = 2\pi\delta(\omega - \omega'), \tag{2.2}$$

where the operator acts on the number state $|n_\omega\rangle$ to create or annihilate a photon:

$$\hat{a}_\omega |n_\omega\rangle = \sqrt{n_\omega}\,|n_\omega - 1\rangle, \tag{2.3a}$$

$$\hat{a}_\omega^\dagger |n_\omega\rangle = \sqrt{n_\omega + 1}\,|n_\omega + 1\rangle. \tag{2.3b}$$

The annihilation and creation operators are non-Hermitian, implying that they have complex eigenvalues. These operators represent no physical variables, hence they are not observable.

2.1.1. Two-photon quadrature operators

In general squeezed states rely on correlation between pairs of photons. In the two-photon formalism a way to describe these correlations between the modes in each pair is to formulate the field operators in terms of a modulation. Conventionally a phase or an amplitude modulation is described in the sideband picture. A carrier field with the fundamental frequency ω_0 that carries a modulation with frequency Ω is expressed by correlated excitation of the sideband fields at frequencies $\omega_0 \pm \Omega_i$ (where the subscript i denotes the i-th modulation frequency). Replacing the frequency $\omega = \omega_0 \pm \Omega$ with carrier frequency ω_0 and modulation sidebands at frequencies Ω we introduce the new operators

$$\hat{a}_+ = \lambda_+ \hat{a}_{\omega_0+\Omega}, \quad \hat{a}_- = \lambda_- \hat{a}_{\omega_0-\Omega}, \tag{2.4}$$

which describe the annihilation of photons at the sideband frequencies $\pm\Omega$.

The parameter $\lambda_\pm = \sqrt{(\omega_0 \pm \Omega)/\omega_0}$ re-scales the different energies of the carrier at Fourier frequency ω_0 and sideband photons at Fourier frequencies $\omega_0 \pm \Omega$. Nevertheless in the following the factor $\lambda_\pm$ is neglected, since $\omega_0 \gg \Omega$: usually optical frequencies are of the order of several hundreds of THz, while a modulation occurs in the MHz regime. Thus $\lambda_\pm$ is approximately equal to unity. Additionally, we consider a noise characteristic that possesses symmetric modulation sidebands. It is practical to introduce the symmetric two-photon quadratures [40]

$$\hat{X}_\Omega = \hat{a}_+ + \hat{a}_-^\dagger, \quad \hat{Y}_\Omega = -i(\hat{a}_+ - \hat{a}_-^\dagger), \tag{2.5}$$

which create a photon at the upper sideband and annihilate a photon at the lower sideband at the same time. For the corresponding quadrature $\hat{X}$ we get:

$$\begin{aligned} \hat{X}_\Omega \left| n_\omega \right\rangle &= (\hat{a}_+ + \hat{a}_-^\dagger) \left| n_\omega \right\rangle \\ &= \sqrt{n_{\omega_0+\Omega}} \left| n_{\omega_0+\Omega} - 1 \right\rangle + \sqrt{n_{\omega_0-\Omega} + 1} \left| n_{\omega_0-\Omega} + 1 \right\rangle , \end{aligned} \tag{2.6}$$

hence the origin of the term ’two-photon’. Concerning the non-vanishing commutation relation between the quadratures reads:

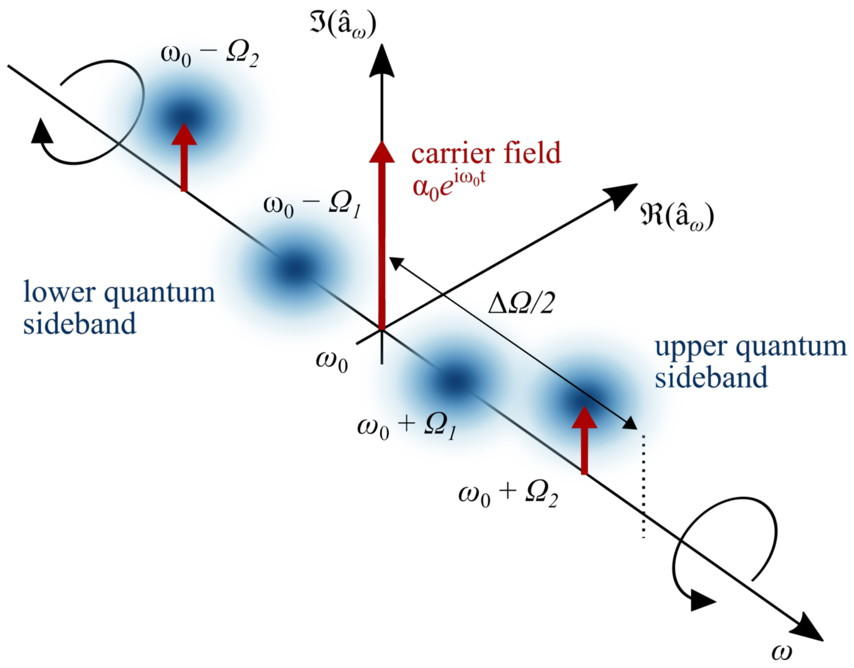

Figure 2.1.: Double sided spectrum of quantum noise sideband fields. The picture depicts the sideband phasors in the rotating frame reference of a carrier field (red arrow at ω_0). The expanded frequency axis shows exemplary the vacuum noise sidebands at frequencies of $(\pm\Omega_1, \pm\Omega_2)$ in the frequency band $\pm\Delta\Omega/2$. The $(\pm)$ determined the direction of rotation with respect to the carrier field. Additionally, the sideband at $\pm\Omega_2$ carries a coherent displacement corresponding to a classical phase modulation. In principle there exists an infinite number vacuum noise sidebands within the bandwidth, each oscillating with random phase and amplitude.

$$[\hat{X}_\Omega, \hat{Y}^\dagger_{\Omega'}] = [\hat{X}^\dagger_{\Omega'}, \hat{Y}_\Omega] = 2i \times 2\pi\delta(\Omega - \Omega'), \tag{2.7}$$

Similar to equation 2.1, we define the positive and negative frequency part of the electric field in terms of the quadratures $\hat{X}_\Omega$ and $\hat{Y}_\Omega$ by

$$\hat{E}^\pm = \frac{1}{2}(\hat{X}_\Omega \pm i\hat{Y}_\Omega)e^{\mp i\omega_0 t}, \tag{2.8}$$

where $\hat{X}_\Omega \pm i\hat{Y}_\Omega$ is the complex amplitude of the electric field, which is defined with respect to the carrier frequency ω_0.

With these operators let us now quantify the electric field in terms of the quadratures, thus it becomes

$$\hat{E}(t) = \hat{X}_\Omega \cos(\omega_0 t) + \hat{Y}_\Omega \sin(\omega_0 t), \tag{2.9}$$

where $\hat{X}_\Omega$ and $\hat{Y}_\Omega$ describe modulations of the light field in two orthogonal quadratures 'cos' and 'sin'. They often referred to as *quadrature phase operators*. With respect to their Fourier components the quadratures can be rewritten as:

$$\hat{X}_\Omega(t) = \sqrt{\frac{2\pi\hbar\omega_0}{\mathcal{A}c}} \int_0^\infty \left(\hat{X}_\Omega e^{-i\Omega t} + \hat{X}_\Omega^\dagger e^{i\Omega t}\right) \frac{d\Omega}{2\pi}, \tag{2.10a}$$

$$\hat{Y}_\Omega(t) = \sqrt{\frac{2\pi\hbar\omega_0}{\mathcal{A}c}} \int_0^\infty \left(\hat{Y}_\Omega e^{-i\Omega t} + \hat{Y}_\Omega^\dagger e^{i\Omega t}\right) \frac{d\Omega}{2\pi}. \tag{2.10b}$$

The phase quadratures are typically observed with a balanced homodyne detection using interference with a bright (classical) local oscillator field (cf. section 3.2.3). When the local oscillator $E = E_{\mathrm{LO}} \cos(\omega_0 t)$ serves as a reference, from superposition with the electric field of 2.9 we obtain [42]

$$\hat{E}(t) = (E_{\mathrm{LO}} + \hat{X}_\Omega) \cos(\omega_0 t) + \hat{Y}_\Omega \sin(\omega_0 t), \tag{2.11}$$

and therefore $\hat{X}_\Omega$ describe the classical analogues of the depth of the lights amplitude modulation, whereas $\hat{Y}_\Omega$ describes the depth of the lights phase modulation. The fundamental operators that induced the modulations are the *amplitude quadrature amplitude operator* $\hat{X}_\Omega$ and the *amplitude quadrature phase operator* $\hat{Y}_\Omega$ at a angular modulation frequency Ω. In real quantum optical experiments the interrogated physical system is determined by the limited time resolution $\Delta\tau$ of the photodetectors [24]. Thus the measured quadratures are usually defined over the integration time $\Delta\tau = 1/\Delta\Omega$:

$$\hat{X}_{\Omega,\Delta\Omega}(t) = \frac{\Delta\Omega}{2}\int_{t-1/\Delta\Omega}^{t+1/\Delta\Omega}\hat{X}_{\Omega}(\tau)\,\mathrm{d}\tau\,, \tag{2.12a}$$

$$\hat{Y}_{\Omega,\Delta\Omega}(t) = \frac{\Delta\Omega}{2}\int_{t-1/\Delta\Omega}^{t+1/\Delta\Omega}\hat{Y}_{\Omega}(\tau)\,\mathrm{d}\tau\,. \tag{2.12b}$$

Thus the resolution bandwidth defines the light mode that is detected. It describes the electrics field modulation in the respective frequency band $\Omega \pm \Delta\Omega/2$.

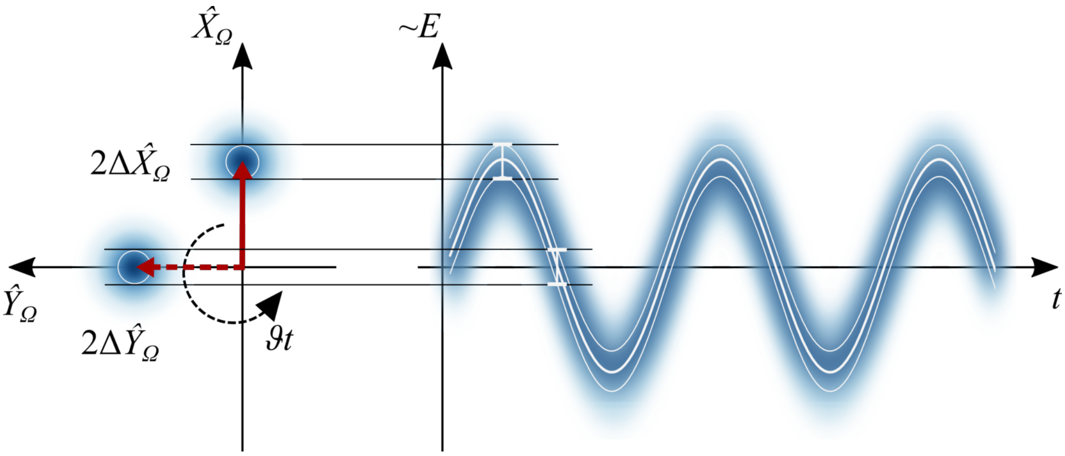

Figure 2.2.: Phase space representation and time dependent coherent modulation field. Left: Phase space representation of a coherent modulation state at frequency Ω for a specific resolution bandwidth $\Delta\Omega$. The displacement (red arrow) corresponds to a classical modulation with an amplitude of $\alpha = \alpha_0 M/2$, where M is the modulation depth. Also pictured are the quantum uncertainties as a result of the superposition of uncorrelated quantum sidebands of the ground state uncertainty (blue shaded area). The white circle enclosed the standard deviation of $2\Delta\hat{X}_\Omega$ and $2\Delta\hat{Y}_\Omega$. By rotating the modulation in phase space, a pure amplitude modulation is converted into a phase modulation, and vice versa. The projection on a fixed axis is proportional to the electric field strength as shown on the right side. The light field that carries the modulation field is not shown.

In general, quantum uncertainty and thereby the quadratures are time-independent. The explicit time dependence points out the time evolution of a varying signal. For the detection of the quadratures by balanced homodyne detection, it is convenient to introduce the *generic quadrature phase* $\hat{X}^{\vartheta}_{\Omega,\Delta\Omega}(t)$ defined as

$$\begin{aligned} \hat{X}^{\vartheta}_{\Omega,\Delta\Omega}(t) &= \hat{X}_{\Omega,\Delta\Omega}(t)\cos(\vartheta) + \hat{Y}_{\Omega,\Delta\Omega}(t)\sin(\vartheta) \\ &= \hat{a}_{+}e^{-i\vartheta} + \hat{a}^{\dagger}_{-}e^{i\vartheta}\,, \end{aligned} \tag{2.13}$$

where any linear combination can be measured between an arbitrary angle $\vartheta \in [0,2\pi]$ by applying a rotation, as depicted in figure 2.2. Especially it clearly shows that $\hat{X}^{\vartheta=0}_{\Omega,\Delta\Omega}(t)$ corresponds to the amplitude quadrature $\hat{X}_{\Omega,\Delta\Omega}(t)$ and that $\hat{Y}^{\vartheta=\pi/2}_{\Omega,\Delta\Omega}$ corresponds to the phase quadrature $\hat{Y}_{\Omega,\Delta\Omega}(t)$. For simplifying the notation, the sideband information $(\Omega, \Delta\Omega)$ will be omitted if no specific modulation state is intended. Also, when the operators are almost not changing with time, the explicit time dependence is skipped, and the quadratures simply are denoted as $\hat{X}$ and $\hat{Y}$.

2.1.2. Vacuum state

Generally the *vacuum state* is described by the absence of any photons on average, e.g. $\hat{n}_{\omega} = 0$, and is defined as

$$\hat{a}_{\omega}\,|\hat{n}_{\omega} = 0\rangle = 0. \tag{2.14}$$

It is the ground state of the quantized harmonic oscillator and therefore the state of the lowest possible energy. Considering a specific mode of light at optical frequency ω the Hamiltonian of the mode is given by

$$\hat{H}_{\omega} = \hbar\omega\left(\hat{a}_{\omega}\hat{a}^{\dagger}_{\omega} + \frac{1}{2}\right) \equiv \hbar\omega\left(\hat{n}_{\omega} + \frac{1}{2}\right), \tag{2.15}$$

which describes the energy of this mode. Furthermore the equation 2.15 describes the energy of a harmonic oscillator. The expectation value of the annihilation operator in the ground state of the single mode as well for the corresponding (two-photon) quadrature operators are

$$\langle 0|\,\hat{a}_\omega\,|0\rangle = \langle \hat{a}_\omega\rangle = \langle \hat{a}^\dagger_\omega\rangle = 0\,, \tag{2.16}$$

$$\langle \hat{X}\rangle = \langle \hat{Y}\rangle = 0\,, \tag{2.17}$$

while the uncertainty contributes to the overall energy, which I verify for the quadratures below. To obtain the energy of a particular sideband frequency Ω the transition to the rotating frame of the fundamental frequency ω_0 is required. The corresponding Hamiltonian of the modulation mode is found by applying the unitary transformation $\hat{U} = \exp(i\omega_0\hat{a}^\dagger\hat{a}t)$ resulting in the Hamiltonian $\hat{H}_\Omega = \hat{U}^\dagger\hat{H}_{\omega_0}\hat{U} - i\hbar\hat{U}\partial\hat{U}^\dagger/\partial t$. The energy of the modulation mode reads

$$\hat{H}_\Omega = \hbar\Omega\left(\hat{a}_\Omega\hat{a}^\dagger_\Omega + \frac{1}{2}\right) \equiv \hbar\Omega\left(\hat{n}_\Omega + \frac{1}{2}\right) \equiv \hbar\Omega\left(\hat{X}^2 + \hat{Y}^2\right)\,, \tag{2.18}$$

that also allows to define the energy in terms of the quadratures at the sideband frequency Ω. Although the vacuum state contains no quanta, the energy does not vanish, since

$$\langle 0|\,\hat{H}\,|0\rangle = \frac{1}{2}\hbar\Omega = \hbar\Omega\,\langle \hat{X}^2 + \hat{Y}^2\rangle\,. \tag{2.19}$$

To show the equivalence in equation 2.19, an appropriate normalization of the quadrature satisfies the commutation relation $[\hat{X},\hat{Y}] = i/2$. Then the ground state energy of the amplitude quadrature is

$$\begin{aligned}\langle 0|\,\hat{X}^2\,|0\rangle &= \frac{1}{4}\,\langle 0|\,(\hat{a}_+ + \hat{a}^\dagger_-)^2\,|0\rangle \\ &= \frac{1}{4}(\langle 0|\,\hat{a}_+\,|1\rangle\,\langle 0|\,\hat{a}^\dagger_-\,|1\rangle) = \frac{1}{4}\end{aligned} \tag{2.20}$$

and similar for $\langle 0|\,\hat{Y}^2\,|0\rangle = 1/4$. This result coincidence exactly with the variance of the corresponding quadrature, since $\langle \Delta^2\hat{X}\rangle = \langle \hat{X}^2\rangle - \langle X\rangle^2 = \langle \hat{X}^2\rangle = 1/4 = \langle \hat{Y}^2\rangle$ (cf. equation 2.49).

Note, that the quadrature operators are obtained by normalization to dimensionless variables. In general, there exists no common normalization, and throughout this thesis the normalization is used that corresponds to the commutation relation of equation 2.5, which results in a variance of the vacuum state of unity.

Usually, to access the quantum properties of the quadrature fields in typical quantum-optics experiments, laser light is used. Thus to ensure the correct description of the physical properties, the class of *coherent states* will be introduced in the next section.

2.1.3. Coherent state

Because laser light does not contain a precisely defined photon number, it is necessary to introduce coherent states. They are eigenstates of the annihilation operator and obtain the eigenvalue equation:

$$\hat{a}\,|\alpha\rangle = \alpha\,|\alpha\rangle\ . \tag{2.21}$$

A coherent excitation at frequencies ω can be obtained by applying the *displacement operator*

$$\hat{D}(\alpha) = e^{\alpha\hat{a}^\dagger - \alpha^*\hat{a}}, \tag{2.22}$$

where α is a complex number that describe the coherent excitation, on the vacuum state

$$\begin{aligned} |\alpha\rangle &\equiv \hat{D}(\alpha)\,|0\rangle \\ &= \exp\left[\int_{-\infty}^{\infty}\left(\alpha_\omega\hat{a}_\omega^\dagger - \alpha_\omega^*\hat{a}_\omega\right)\frac{d\omega}{2\pi}\right], \end{aligned} \tag{2.23}$$

that displaces the vacuum state to a particular point α in phase space. This is known as coherent state [43]. To get coherent excitation's in the two-photon formalism of sideband modulation at frequencies $\pm\Omega$ can be obtained by applying a combination of displacement operators

$$|\alpha_+,\alpha_-\rangle = \hat{D}_+(\alpha_+)\hat{D}_-(\alpha_-)\,|0\rangle\ . \tag{2.24}$$

The displacement operator is unitary with property

$$\hat{D}^\dagger(\alpha)\hat{a}\hat{D}(\alpha) = \hat{a}+\alpha, \quad \hat{D}^\dagger(\alpha)\hat{a}^\dagger\hat{D}(\alpha) = \hat{a}^\dagger+\alpha^*, \tag{2.25}$$

that allows to evaluate the quadratures phases in terms of its quantum fluctuations. The coherent displacement α is closely linked to the expectation values of the quadrature phase operators,

$$\langle\hat{X}\rangle = \alpha + \alpha^* = 2\mathrm{Re}(\alpha)\,, \tag{2.26}$$

$$\langle\hat{Y}\rangle = i(\alpha - \alpha^*) = 2\mathrm{Im}(\alpha)\,, \tag{2.27}$$

which is equivalent to $\alpha = \frac{1}{2}(\langle\hat{X}\rangle + i\,\langle\hat{Y}\rangle)$ with $\langle X\rangle = \langle\alpha|\hat{X}\,|\alpha\rangle$ and $\langle Y\rangle = \langle\alpha|\hat{Y}\,|\alpha\rangle$. In phase space, as depicted in figure 2.2 of the quadrature fields, the coherent modulation amplitude $\alpha = |\alpha|e^{i\vartheta}$ is represented by a *phasor* with length $\alpha = \sqrt{\langle\hat{X}\rangle^2 + \langle\hat{Y}\rangle^2} = \alpha_0\,\mathrm{M}/2$ at an angle ϑ and the modulation depth M. Such a coherent excited modulation is illustrated in figure 2.1 together with the equally distributed uncertainty in both quadratures which have to obey

$$\Delta^2\hat{X} = \Delta^2\hat{Y} = 1 \tag{2.28}$$

normalized to unity.

The probability distribution, which describes the indefinite number of quanta contained in the coherent states is given by the Poissonian distribution

$$P(n) = |\,\langle n|\alpha\rangle\,|^2 = \frac{|\alpha|^{2n}e^{-\alpha^2}}{n!}\,, \tag{2.29}$$

where the mean photon number is proportional to the electric field power as measured by a photodetector, and is given by expectation value of the number operator

$$\bar{n} = \langle\alpha|\,\hat{a}^\dagger\hat{a}\,|\alpha\rangle = |\alpha|^2\,. \tag{2.30}$$

An important property of the Poissonian distribution is that the variance $\Delta^2\hat{n} = \bar{n}$. Thus by comparing the fluctuations of the photon number with its mean value, results in the fractional uncertainty

$$\frac{\Delta\hat{n}}{\bar{n}} = \frac{1}{\sqrt{\bar{n}}}. \tag{2.31}$$

With increasing number of photons leads to decreasing relative uncertainty. As we will see in chapter 4, the scaling is an important issue for the sensitivity in high precision phase measurements, e.g. in interferometers.

2.1.4. Squeezed state

If the modulation sidebands in equation 2.2 show non-classical correlation, the uncertainties at the sidebands $\omega_0 \pm \Omega$ are not independent anymore. Such correlation produces *squeezed states of light* and are expressed by the correlated excitation process described by the squeeze operator

$$\hat{S}(\zeta) = \exp\left[\int_{-\infty}^{\infty} \frac{1}{2}\left(\zeta^* \hat{a}_+ \hat{a}_- - \zeta \hat{a}_+^\dagger \hat{a}_-^\dagger\right) \frac{\mathrm{d}\Omega}{2\pi}\right], \tag{2.32}$$

where $\zeta = r\exp(i\Theta)$ is the squeeze parameter, which describes the strength of squeezing upon the vacuum state. The phase angle Θ determines the direction of the squeezed quadrature. Therefore to generate a squeezed vacuum state the squeeze operator is applied on the vacuum state:

$$|\zeta\rangle = \hat{S}(\zeta)\,|0\rangle\,. \tag{2.33}$$

In accordance to the quadratures, the effect of the squeeze operator mixes the annihilation and creation operator of lower and upper sideband photons, which evolution is defined by:

$$\hat{S}^\dagger(\zeta)\hat{a}\hat{S}(\zeta) = \hat{a}_+ \cosh(r) + \hat{a}_-^\dagger e^{i\Theta} \sinh(r)\,, \tag{2.34a}$$

$$\hat{S}^\dagger(\zeta)\hat{a}^\dagger\hat{S}(\zeta) = \hat{a}_+^\dagger \cosh(r) + \hat{a}_- e^{i\Theta} \sinh(r)\,. \tag{2.34b}$$

To manage the quadrature phases under this specific transformation, simultaneously, it is useful to combine them into a state vector

$$\hat{\boldsymbol{x}} = \begin{pmatrix} \hat{X} \\ \hat{Y} \end{pmatrix}. \tag{2.35}$$

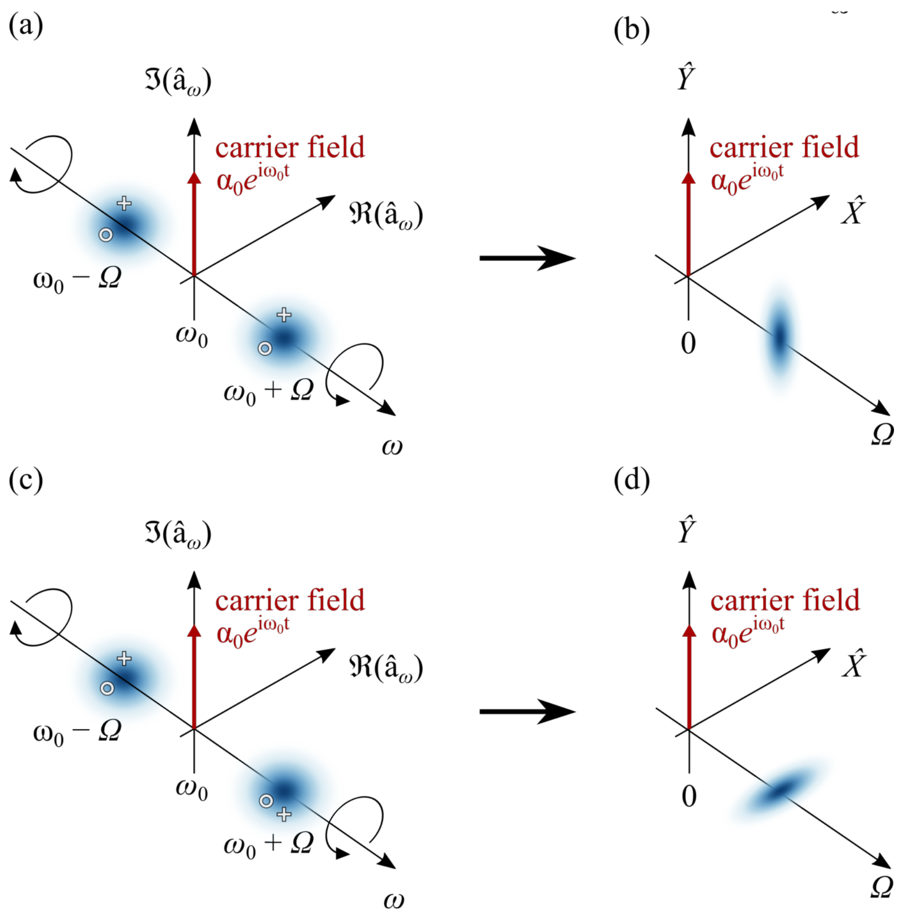

Figure 2.3.: Double-sided and single-sided phasor pictures of modulation fields. Left: Illustration of the quantum correlated noise sidebands at optical frequency of $\omega_0 \pm \Omega$ in the double-sided picture. The sign determines the direction of rotation with respect to the rotating frame of the local oscillator (carrier field) at frequency ω_0. The quantum correlation are marked with the white crosses and circles. The figure (a) shows an amplitude squeezed state with a fixed relative phase of $\Theta = 0$ between the upper and lower sideband. In contrast in (c) the sidebands are phase shifted by $\Theta = \pi$ to each other, resulting in a phase squeezed state. Right: Shows the corresponding single-sided spectrum to visualizes the squeezed fields arising due to the quantum correlation. (b) amplitude squeezed (d) phase squeezed.

Applying the squeezed operator to the state vector $\hat{\boldsymbol{x}}$ generates a matrix transformation according to [41]

$$\hat{S}^\dagger(\zeta)\hat{\boldsymbol{x}}\hat{S}(\zeta) = \boldsymbol{S}(\zeta)\hat{\boldsymbol{x}}, \tag{2.36}$$

with

$$\boldsymbol{S}(\zeta) = \begin{pmatrix} e^{-\zeta} & 0 \\ 0 & e^{+\zeta} \end{pmatrix}. \tag{2.37}$$

when choosing the relative phase $\Theta = 0$ between the upper and lower sidebands. The effect of the squeeze operator on the vacuum state is illustrated in figure 2.3. The squeeze operator transforms the quadrature vector state as

$$\hat{\boldsymbol{x}}^a_{sqz} = \boldsymbol{S}(\zeta = r)\hat{\boldsymbol{x}} = \begin{pmatrix} e^{-r} & 0 \\ 0 & e^{+r} \end{pmatrix} \begin{pmatrix} \hat{X} \\ \hat{Y} \end{pmatrix} = \begin{pmatrix} \hat{X}e^{-r} \\ \hat{Y}e^{+r} \end{pmatrix}, \tag{2.38}$$

which results in an *amplitude squeezed vacuum state*, while the orthogonal phase quadrature is anti-squeezed at the same moment. The quantum fluctuation of the squeezed quadratures become

$$\langle\zeta|\Delta^2\hat{\boldsymbol{x}}^a_{sqz}|\zeta\rangle = \begin{pmatrix} e^{-2r} \\ e^{+2r} \end{pmatrix}, \tag{2.39}$$

where the uncertainty of the amplitude squeezed vacuum state is reduced by the factor e^{-r} below the vacuum uncertainty of the ground state, while the orthogonal phase quadrature is simultaneously enlarged by the same factor. A squeezed state in an arbitrary direction can be realized by applying a rotation $\boldsymbol{R}(\Theta)$. A *phase squeezed state* is realized by a rotation of π:

$$\hat{\boldsymbol{x}}^p_{sqz} = \boldsymbol{R}(-\pi)\boldsymbol{S}(r)\boldsymbol{R}(\pi)\hat{\boldsymbol{x}} = \begin{pmatrix} \hat{X}e^{+r} \\ \hat{Y}e^{-r} \end{pmatrix}, \tag{2.40}$$

with

$$\boldsymbol{R}(\Theta) = \begin{pmatrix} \cos(\Theta) & \sin(\Theta) \\ -\sin(\Theta) & \cos(\Theta) \end{pmatrix}, \tag{2.41}$$

where the identity $\boldsymbol{R}^\dagger(\Theta) = \boldsymbol{R}(-\Theta)$ is satisfied.

2.2. Gaussian states and quasi-probabilities

Squeezing is best visualized by means of Wigner function, which is the quantum analogue of the phase space probability density. Since the above introduced coherent and squeezed states have Gaussian quantum statistic, the first and second statistical moments are sufficient for their full description. The first moments describe the displacement of the mean value $\boldsymbol{\mu}$, while the second moment is given by the covariance matrix γ. They read

$$\mu_i = \langle \hat{V}_i \rangle\,, \tag{2.42}$$

$$\gamma_{ij} = \mathrm{cov}(\hat{V}_i, \hat{V}_j)\,, \tag{2.43}$$

where the covariance matrix is defined as $\mathrm{cov}(\hat{V}_i, \hat{V}_j) = \frac{1}{2}\langle \hat{V}_1\hat{V}_2 + \hat{V}_2\hat{V}_2\rangle - \langle \hat{V}_1\rangle \langle \hat{V}_2\rangle$. It represents the correlation measure for two random variables. From this follows for two operators $\hat{V}_1$ and $\hat{V}_2$ the covariance matrix:

$$\gamma = \begin{pmatrix} \mathrm{Var}(\hat{V}_1) & \mathrm{cov}(\hat{V}_1, \hat{V}_2) \\ \mathrm{cov}(\hat{V}_1, \hat{V}_2) & \mathrm{Var}(\hat{V}_2) \end{pmatrix}, \tag{2.44}$$

The Wigner function of a Gaussian state is defined as

$$W(\boldsymbol{x}) = \frac{1}{2\pi\sqrt{\det\gamma}} \exp\left[-\frac{1}{2}(\boldsymbol{x}-\boldsymbol{\mu})\gamma^{-1}(\boldsymbol{x}-\boldsymbol{\mu})^T\right], \tag{2.45}$$

which is normalized to unity

$$\int_{-\infty}^{\infty} d\boldsymbol{x}\, W(\boldsymbol{x}) = 1. \tag{2.46}$$

The marginal distributions can be calculated by integrating the Wigner function over the respective quadrature, providing the probability density of eigenvalues of the other observable, and vice versa. The corresponding projections are

$$\int_{-\infty}^{\infty} W(\boldsymbol{x})\, dY = \mathrm{P}(X) \quad , \int_{-\infty}^{\infty} W(\boldsymbol{x})\, dX = \mathrm{P}(Y). \tag{2.47}$$

The distribution are depicted in figure 2.4.

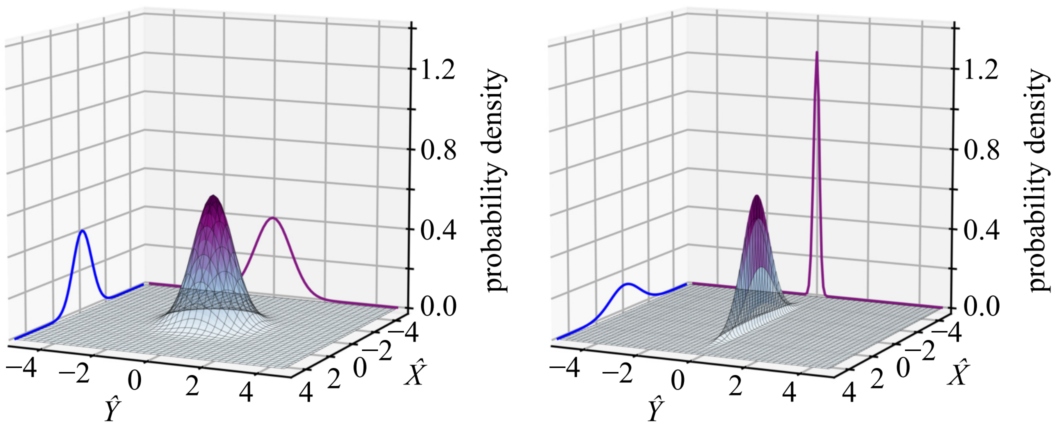

Figure 2.4.: Wigner function and its marginal distributions of the vacuum state (a) and a squeezed state (b). The quasi probability density of the Wigner function (center) can be reconstructed from Gaussian projections onto the amplitude quadrature $\hat{X}$ (blue lines) and of the phase quadrature $\hat{Y}$ (purple lines) axes. Their probability densities P(X) and P(Y) are also displayed on the vertical axes. (a) The Wigner representation of a vacuum state with $\boldsymbol{\mu} = (0,0)^T$ and variances of $\Delta^2\hat{X} = \Delta^2\hat{Y} = 1$. (b) The Wigner representation of a phase squeezed vacuum state with $\Delta^2\hat{Y} = 0.1$, corresponding to a squeeze parameter of $r = 1.15$. The statistics for the phase quadrature clearly shows a smaller variance in comparison to the probability distribution of the vacuum state. Likewise, the amplitude quadrature shows a broader distribution of the same factor.

2.2.1. Husimi-Q function

Another important phase space representation of a probability density for quantum states is the Q function. In an ideal measurement, it is necessary to perform a sequential measurement on one copy of a system, to obtain $\hat{X}$ and on a second copy to obtain the $\hat{Y}$ values, which lead to the Wigner function. However, measurement of both quadratures simultaneously involves an equal splitting of the system, which emerges directly in the phase space representation of the Q function. This probability distribution can be understood as the convolution of the Wigner function $W(\boldsymbol{x})$ with the ground state uncertainty distribution. We obtain the following distribution:

$$Q(\boldsymbol{x}) = \frac{1}{\pi}\int_{-\infty}^{\infty} W(\boldsymbol{x}')\exp\left[-(\boldsymbol{x}-\boldsymbol{x}')^2\right] d\boldsymbol{x}'. \tag{2.48}$$

Therefore we see, its a smoothing of the Wigner function applying a Gaussian filter. The measured phase space probability is a non-negative smoothed Wigner function. Exactly this phase space probability Q function is measured with the two homodyne detectors in chapter 6.

2.3. Quantum uncertainty and entanglement

Shortly after Heisenberg introduced the characteristic uncertainty of the precision of simultaneous position and momentum measurement performed on a quantum particle, the mathematical description was given by E.H. Kennard [5], H. Weyl [6] and, H.P. Robertson [7]. A generalized uncertainty-relation of a pair of conjugate operators was given on the grounds of quantum theory by E. Schrödinger [8]. The aim is to relate the variances of two hermitian operators Q and P with their commutator. Define the operator $\Delta\mathcal{O} \equiv \mathcal{O} - \langle\mathcal{O}\rangle$. Then the variance of an arbitrary operator is

$$\langle\Delta^2\mathcal{O}\rangle = \langle\mathcal{O}^2\rangle - \langle\mathcal{O}\rangle^2. \tag{2.49}$$

For two Hermitian operators Q and P the product $\Delta Q\Delta P$ can be symmetrical splitted into a commutator part and an anti-commutator part [8, 44]

$$\Delta Q\Delta P = \frac{1}{2}[\Delta Q,\Delta P] + \frac{1}{2}\{\Delta Q,\Delta P\}, \tag{2.50}$$

where the anti-commutator is defined as $\{Q,P\} = QP + PQ$. To relate the variance to the commutator, we have to consider the expectation value of $\Delta Q\Delta P$. Since the anti-commutator is a Hermitian operator it has a real expectation value. In contrast any anti-Hermitian operator (the conjugate is the negative of the operator) has an imaginary expectation value. Thus the right side of the equation 2.50 is in general a complex number and is expressed as the real and imaginary part, like $u+iv$. It follows immediately that the magnitude of the squared of its expectation value is

$$\langle|\Delta^2 Q \Delta^2 P|\rangle = \frac{1}{4}|\langle[Q,P]\rangle|^2 + \frac{1}{4}|\langle\{\Delta Q, \Delta P\}\rangle|^2, \tag{2.51}$$

where the identity

$$\begin{aligned}[\Delta Q, \Delta P] = &QP - Q\langle P\rangle - \langle Q\rangle P + \langle Q\rangle\langle P\rangle \\ &- PQ + P\langle Q\rangle + \langle P\rangle Q - \langle P\rangle\langle Q\rangle = [Q,P],\end{aligned} \tag{2.52}$$

is used. This allows us now to apply the Schwarz inequality to two kets $|\Psi_a\rangle$ and $|\Psi_b\rangle$, for which hold $\langle\Psi_a|\Psi_a\rangle\langle\Psi_b|\Psi_b\rangle \geq |\langle\Psi_a|\Psi_b\rangle|^2$. Setting $|\Psi_a\rangle = \Delta Q|\Psi\rangle$ and $|\Psi_b\rangle = \Delta P|\Psi\rangle$ for any $|\Psi\rangle$ results in

$$\langle\Delta^2 Q\rangle\langle\Delta^2 P\rangle \geq \langle|\Delta^2 Q \Delta^2 P|\rangle = \frac{1}{4}|\langle[Q,P]\rangle|^2 + \frac{1}{4}|\langle\{\Delta Q, \Delta P\}\rangle|^2. \tag{2.53}$$

The last term on the right side in 2.53 takes the correlation between the quantities Q and P into account; it describes the covariance $\{\Delta Q, \Delta P\} \equiv \mathrm{cov}(Q,P)$. Assuming that the two random quantities are statistical independent one from another, is a necessary (but not sufficient) condition providing a vanishing covariance. The generalized inequality 2.53 takes the simpler form

$$\langle\Delta^2 Q\rangle\langle\Delta^2 P\rangle \geq \frac{1}{4}|\langle[Q,P]\rangle|^2, \tag{2.54}$$

and coincidence with the Robertson-Uncertainty-Relation. Accordingly, equation 2.54 sets fundamentally a lower bound to the precision of any pair of Hermitian operators that is related to their commutator $[Q,P]$. Considering the commutator 2.7 of the quadrature operators $\hat{X}$ and $\hat{Y}$, the product of their variances satisfies an uncertainty relation of the following form:

$$\Delta^2\hat{X}\Delta^2\hat{Y} \geq 1. \tag{2.55}$$

The vacuum state, coherent states and squeezed states minimize the right side of the inequality 2.54 and are known as minimum uncertainty states.

2.3.1. Einstein-Podolsky-Rosen entanglement

The conclusive interpretation of this relation states that the observables of non-commuting operator pairs are not precisely defined simultaneously. With contradiction to the HUR, the seminal article by A. Einstein, B. Podolsky and N. Rosen (EPR) from 1935 described a quantum correlated system, consisting of two partial systems, which seemingly lead to a paradox situation. They pointed out a startling quantum phenomenon: *entanglement*.

Since the position and the momentum operators have a non zero-commutator, it implies that one cannot simultaneously attach a precisely defined value to both canonical conjugate quantities of a individual system with respect to the environment. In accordance with EPRs criterion of ‘physical reality’ they conclude that only one of these operators ascribe as part of reality at any time. The apparent contradiction emerges when they considered a particle that is entangled with a another one. They showed that such a system possesses quantum correlations between the two quantities, that have a simultaneously precisely defined position and momentum with respect to each other. Without any disturbance, this allows to predict either the position or the momentum of the first particle with certainty by a measurement on the second particle. This would suggest that the first particle had simultaneously precisely defined position and momentum before the measurement, contrary to the initial assumption. Therefore EPR wrongly conjectured that quantum mechanics is incomplete. In fact, their contradiction discloses only in their strong requirement on the premise of local realism, which demand that a measurement at location B does not influence the system at spatially separated location A.

2.3.2. Bi-partite squeezed states

To recreate the discussed entangled EPR-states of the previous section in quantum optics, we consider a bi-partite squeezed state that is composed of two spatially separated subsystems A and B. Experimentally this can be realized by overlapping two squeezed states on an symmetric (50:50) beam splitter with a relative phase shift of $\pi/2$ to each other. The states are corresponding to an amplitude squeezed and a phase squeezed state with squeeze parameter r and q, respectively. The observables that are *entangled* according to the EPR-paradox are $\hat{X}_A \pm \hat{X}_B$ and $\hat{Y}_A \mp \hat{Y}_B$. Those quantities are well determined (in the sense of 'defined') with respect to each other. The generation of a bipartite squeezed EPR-entangles state is illustrated in figure 2.5.

A criterion to quantify the strength of entanglement in the regime of continuous variables with quadrature phase measurements was introduced by Reid [45]. Observing the EPR-Reid criterion

$$\mathcal{E}^2 = \Delta^2 \hat{X}_{\text{cond}} \Delta^2 \hat{Y}_{\text{cond}} \leq 1\,, \tag{2.56}$$

with the minimum conditional variance $\Delta^2 \hat{\mathcal{O}}_{\text{cond}}|_{\text{min}} = \Delta^2(\hat{\mathcal{O}}_A - g\hat{\mathcal{O}}_B)$ of the observable $\hat{\mathcal{O}}$ implies the EPR-Paradox. The real-valued scaling parameter g is accordingly adjusted to minimize the conditional variance of A's quantity $\hat{X}_A(\hat{Y}_A)$ based on the result of $\hat{X}_B(\hat{Y}_B)$ for a measurement at system B. We consider a bipartite Gaussian entangled state consisting of two partial systems A and B represented by their quadratures $\hat{X}_{A,B}$ and $\hat{Y}_{A,B}$. For this state the optimum value g = $\text{cov}(\hat{X}_A, \hat{X}_B)/\Delta^2\hat{X}_B$. Then the predicted minimum variances become

$$\Delta^2 \hat{X}_{\text{cond}}|_{\text{min}} = \Delta^2 \hat{X}_A - \frac{\text{cov}(\hat{X}_A, \hat{X}_B)^2}{\Delta^2 \hat{X}_B}\,, \tag{2.57a}$$

$$\Delta^2 \hat{Y}_{\text{cond}}|_{\text{min}} = \Delta^2 \hat{Y}_A - \frac{\text{cov}(\hat{Y}_A, \hat{Y}_B)^2}{\Delta^2 \hat{Y}_B}\,. \tag{2.57b}$$

The conditional variances solely depend on the covariance matrix γ as defined in 2.2. This also includes the cross-correlations terms $\Delta^2(\hat{X}_A - \hat{X}_B)$ and $\Delta^2(\hat{Y}_A + \hat{Y}_B)$, which are important as I show below. Therefore the variances are related to the uncertainties with which system A's quantities $\hat{X}_A$ and $\hat{Y}_A$ can be predicted conditioned, respectively, on the measurement results of system B's quantities $\hat{X}_B$ and $\hat{Y}_B$.

To prepare the bipartite squeezed state, the following state vector $\hat{\boldsymbol{x}} = (\hat{X}_1, \hat{Y}_1, \hat{X}_2, \hat{Y}_2)^T$ is considered. The state A is in an amplitude squeezed state, while state B is in phase squeezed state. The resulting covariance matrix of the two input states in then given

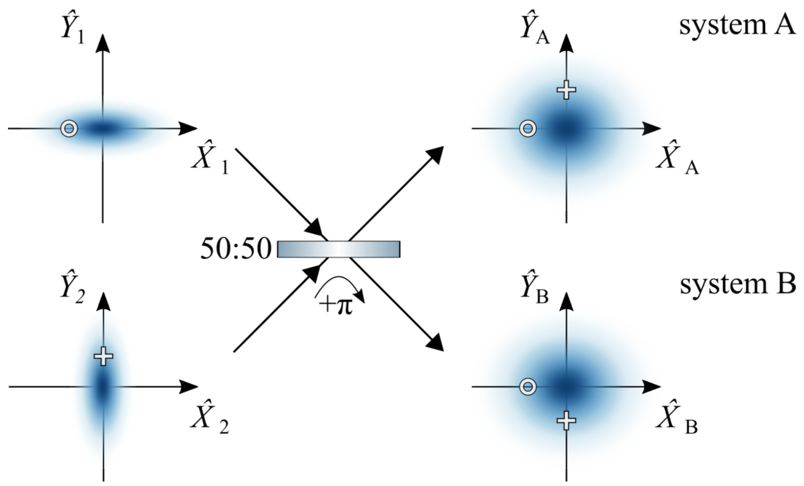

Figure 2.5.: Preparation of bipartite squeezed EPR-entangled state. The picture shows the phase space representation of the Wigner-function indicated by the blue shaded regions. Shown is a single modulation frequency Ω with a bandwidth $\Delta\Omega$. The two parties A and B at the output ports of the beam splitter are entangled and being locally in a thermal state. Also pictured are the uncertainties correlations and anti-correlations, here marked by the white circles and crosses. Performing a measurement on either $\hat{X}_A$ or $\hat{Y}_B$ lead to a prediction of System B's corresponding quantities with an uncertainty smaller than the ground state uncertainty.

by

$$\gamma = \begin{pmatrix} e^{+2q} & 0 & 0 & 0 \\ 0 & e^{-2q} & 0 & 0 \\ 0 & 0 & e^{+2r} & 0 \\ 0 & 0 & 0 & e^{-2r} \end{pmatrix}. \tag{2.58}$$

By interfering the two input states on the balanced beam splitter transforms according to $\hat{\boldsymbol{x}}' = \hat{U}\hat{\boldsymbol{x}}\hat{U}^\dagger = \boldsymbol{B}\hat{\boldsymbol{x}}$, with

$$\boldsymbol{B} = \frac{1}{\sqrt{2}} \begin{pmatrix} 1 & 0 & 1 & 0 \\ 0 & 1 & 0 & 1 \\ 1 & 0 & -1 & 0 \\ 0 & 1 & 0 & -1 \end{pmatrix}. \tag{2.59}$$

The resulting output state vector is given by

$$\hat{\boldsymbol{x}}' = \frac{1}{\sqrt{2}}\begin{pmatrix} \hat{X}_A e^{+q} - \hat{X}_B e^{+r} \\ \hat{Y}_A e^{-q} - \hat{Y}_B e^{-r} \\ \hat{X}_A e^{+q} + \hat{X}_B e^{+r} \\ \hat{Y}_A e^{-q} + \hat{Y}_B e^{-r} \end{pmatrix} . \tag{2.60}$$

Similarly, the covariance matrix transforms according to $\gamma' = \boldsymbol{B}\gamma\boldsymbol{B}^T$, thus

$$\gamma' = \frac{1}{2}\begin{pmatrix} e^{+2q}+e^{-2r} & 0 & e^{+2q}-e^{-2r} & 0 \\ 0 & e^{-2q}+e^{+2r} & 0 & e^{-2q}-e^{+2r} \\ e^{+2q}-e^{-2r} & 0 & e^{+2q}+e^{-2r} & 0 \\ 0 & e^{-2q}-e^{+2r} & 0 & e^{-2q}+e^{+2r} \end{pmatrix} , \tag{2.61}$$

where the variance of each output is described by a thermal state

$$\Delta^2\hat{X}_A = \Delta^2\hat{X}_B = \frac{e^{-2q}+e^{+2r}}{2} > 1 , \tag{2.62}$$

$$\Delta^2\hat{Y}_B = \Delta^2\hat{Y}_B = \frac{e^{+2q}+e^{-2r}}{2} > 1 . \tag{2.63}$$

However, if the correlations of the quadrature operators are considered, e.g. the difference $\hat{X}^- = \hat{X}_A - \hat{X}_B$ of the amplitude quadratures and the sum $\hat{Y}^+ = \hat{Y}_A + \hat{Y}_B$, the quadratures show the initial squeezed variances,

$$\Delta^2\hat{X}_{\text{cond}} = \Delta^2\hat{X}^- = e^{-2r} \tag{2.64}$$

$$\Delta^2\hat{Y}_{\text{cond}} = \Delta^2\hat{Y}^+ = e^{-2q}, \tag{2.65}$$

and their variance product is finally given by

$$\Delta^2\hat{X}_{\text{cond}}\Delta^2\hat{Y}_{\text{cond}} = e^{-2r}e^{-2q} < 1. \tag{2.66}$$

The generation of bipartite squeezed state demonstrates the EPR-Reid inequality for all positive squeeze values r and q, which coincidence with the entangled state of two systems as considered by EPR. Even if only one input state is vacuum squeezed (e.g. $q > 0$, $r = 0$) the inequality is maintained.

In chapter 6 such a bipartite squeezed state is used to investigate whether it is possible to precisely determine a trajectory with respect to another system in the case both systems are not coupled to the environment.

2.4. Decoherence: influence of optical loss

Non-classical properties like entanglement and squeezing are quantified by their purity. Decoherence due to the coupling to the environment reduces the states' purity and therefore the strength of non-classically. In a realistic quantum optical experiment the main effect of decoherence is affected by optical loss when photons get lost. When light is propagating along the optical path, it experiences absorption in optical materials, imperfect detection efficiency or non-optimal fringe contrast between two modes at a beam splitter. The influence of losses on a squeezed

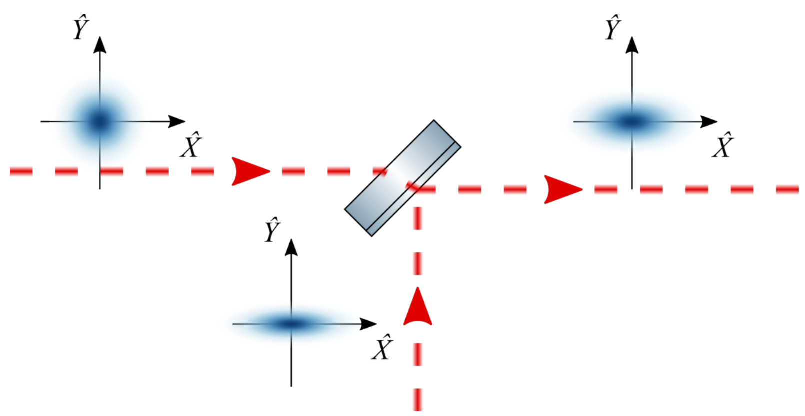

Figure 2.6.: Decoherence due to optical loss. The optical loss ε is visualized by its effect on an amplitude squeezed state in phase space. The virtual beam splitter admixture a fraction of vacuum state (from left) to the squeezed state (from bottom), as a result the output is a squeezed state with reduced squeeze parameter r.

light field can be mathematically modeled by a virtual beam splitter operation, which contributes a fraction $\sqrt{1-\varepsilon}$ of the vacuum state to a squeezed state as it is visualized in figure 2.6. Here ε denotes the power reflectivity of the beam splitter, which directly corresponds to the amount of loss. The unitary transfer matrix of the beam splitter is described by

$$\boldsymbol{BS}_{\text{loss}} = \begin{pmatrix} \sqrt{1-\varepsilon} & \sqrt{\varepsilon} \\ -\sqrt{\varepsilon} & \sqrt{1-\varepsilon} \end{pmatrix}, \tag{2.67}$$

whereby the evolution under this matrix is mixing the squeezed state and vacuum state.

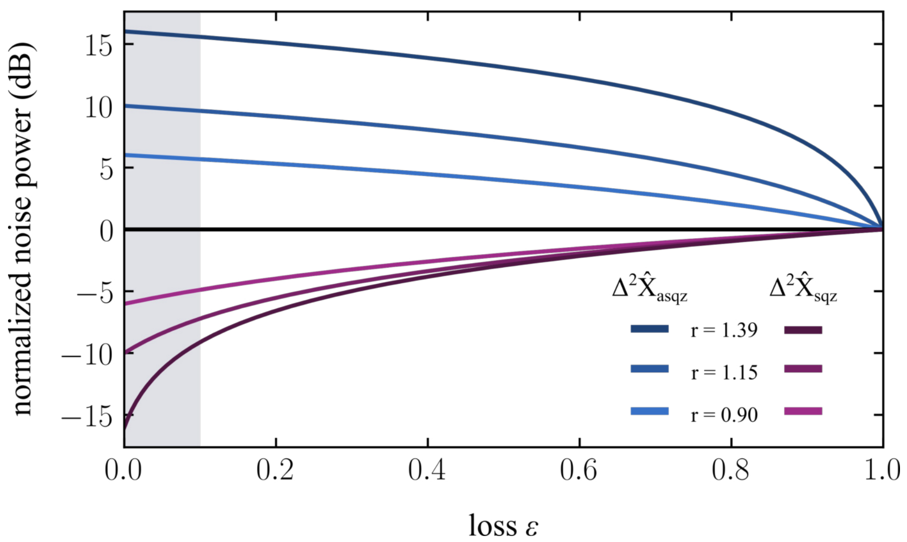

Figure 2.7.: Influence of optical loss on squeezed states with r = (1.39, 1.15, 0.90). The initial squeezed variances $\Delta^2\hat{X}_{\text{sqz}}(\Delta^2\hat{X}_{\text{asqz}})$ are normalized to the vacuum variance $\Delta^2\hat{X}_{\text{vac}} = 1$ and correspond to a noise power of -6 dB, -10 dB, and -16 dB, respectively. The variances of the squeezed quadrature are pictured in purples, while the respective anti-squeezed quadratures are pictured in blues. According to equation 2.68 the squeezed quadrature is more strongly effected by optical loss then the anti-squeezed quadrature. Therefore the overall loss in the experiment is a crucial factor for detecting high squeeze values. To reach a 10 dB non-classical noise reduction, less then 10 % loss is required (gray shaded region), which is independent on the initial squeezing.

The variance of the squeezed state affected by the loss ε is therefore

$$\Delta^2\hat{X}_{\vartheta} = (1-\varepsilon)\Delta^2\hat{X}_{\mathrm{sqz}} + \varepsilon\Delta^2\hat{X}_{\mathrm{vac}}. \tag{2.68}$$

Revisiting that the generation of a squeezed state relies on the correlation between the upper and lower sideband of photon pair, loss can also be understood in the following way: If one of the photon pair gets lost, e.g. due to absorption, the correlation to the second photon is destroyed and is replaced by an uncorrelated vacuum photon.

Ultimately the loss determined the detectable squeeze value. Figure 2.7 displays the resulting squeezed noise variance normalized to the variance vacuum noise as function of loss ε. The squeezed quadrature (purple) is more fragile to the optical loss than the anti-squeezed quadrature (blue). The robustness of the latter is explained by its much larger noise variance compared to the vacuum uncertainty, while the squeezed variance is relative small.

Normally one attempts to prevent this unwanted effect by reducing the optical loss. Therefore figure 2.7 demonstrates the essential requirement for low-loss experiments when employing quantum correlated systems. To detect 10 dB squeezed light, maximal loss of 10 % is barely acceptable. Nevertheless there are a few applications which indeed benefit from the high sensitivity of squeezed states to optical loss. One example is presented in chapter 4, where this feature is exploited to estimate the absorption of a sample.

3. Foundations of experimental methods

Quantum experiments in sensing utilizing squeezed states of light are used to investigate the quantum enhancement of the noise characteristic compared to its classical counterpart. The common ground is predominately the production process known as degenerated parametric down-conversion in second order non-linear crystals [18]. It is usually followed by characterization in balanced homodyne detection of the generated states. The goal of this chapter is to present the pool of common tools developed in previous works (see e.g. [46, 47]). I roughly describe the typical experimental techniques required for the generation of squeezed light and give an overview about the setup implemented during this thesis.

3.1. Squeezed light generation by parametric down-conversion in an optical cavity

For the squeezing operator introduced in section 2.32, a correlated two-photon pair interaction is required. The continuous vacuum squeezed states of light in this thesis are generated by the process of degenerated parametric down-conversion (PDC) in optical parametric amplifiers (OPAs) [48–50]. The correlated photon pairs are created at the fundamental wavelength of 1550 nm in a non-linear medium. For this purpose light at the second harmonic wavelength (775 nm) is sent into a birefringent periodically poled potassium titanyl phosphate (PPKTP) crystal.

$$\mathcal{P}(\mathcal{E}(t)) = \varepsilon_0 \left(\chi^{(1)}\mathcal{E}(t) + \chi^{(2)}\mathcal{E}^2(t) + \chi^{(3)}\mathcal{E}^3(t) + ...\right), \tag{3.1}$$

where $\chi^{(i)}$ is the i-th order dielectric susceptibility and ε_0 is the dielectric permittivity of vacuum. Typical values for the electric susceptibilities are $\chi^{(1)} \approx 1$, $\chi^{(2)} \approx 10^{-12}\frac{m}{V}$, $\chi^{(3)} \approx 10^{-24}\frac{m^2}{V^2}$, and hence for low field intensities only the linear and quadratic term accounts for the effect of OPA. Therefore in the further discussion it is suffice to consider non-linearities up to the 2$^{\text{nd}}$-order.

Because of the quadratic term of the electric field, a fundamental field $\mathcal{E}(t) = \mathcal{E}_0 \cos(\omega_0 t)$ oscillating at a frequency of ω_0 interferes with a harmonic field of twice the frequency

$$\mathcal{E}^2(t) = \frac{\mathcal{E}_0^2}{2}(1 + \cos(2\omega_0 t)). \tag{3.2}$$

In order to fulfill energy conservation, the process has to involve the interaction of three photons. Two photons of the frequencies $\omega_+ = \omega_0 + \Omega$ and $\omega_- = \omega_0 - \Omega$ interact with one photon at the sum frequency $2\omega_0$. Degeneracy is achieved for $\Omega = 0$. These down-conversion process comply with the requirement for the creation of correlated photon pairs, described as sidebands of $\pm\Omega$ with respect to the carrier field at frequency ω_0 (see section 2.1.1).

A graphical illustration of the process of degenerate type I parametric down-conversion (PDC) to produce squeezed states of light in a non-linear crystal shows figure 3.1 [51]. The process itself is solely located to a short segment of the crystal, when it is pumped with a bright laser light of optical frequency $2\omega_0$. Also vacuum states at frequency ω_0, which are spatially overlapping with the fundamental field, enter the crystal. The figure 3.1 pictures the electric field of the incoming light $\mathcal{E}^{\text{in}}$ that induces a non-linear response of the dielectric polarization $\mathcal{P}(\mathcal{E})$ that is proportional to the radiated total electric field output $\mathcal{E}^{\text{out}}$. The pump field at $2\omega_0$ periodically drives the vacuum field at ω_0 between (phase-dependent) amplification and deamplification along the characteristic polarization curve. This process transfers the input vacuum state into a squeezed vacuum state $\mathcal{E}_{\text{sqz},\omega_0}$ at the output. The decomposition of the output field $\mathcal{E}^{\text{out}}$ also reveals classical fields at frequencies of $2\omega_0$ and $4\omega_0$ leaving the non-linear medium. The amplitude at the frequency component $2\omega_0$ correspond to the pump field's first-order polarization $\mathcal{P}^{(1)}(\mathcal{E}_{2\omega_0})$, while the amplitude at the frequency component at $4\omega_0$ corresponds to the second-

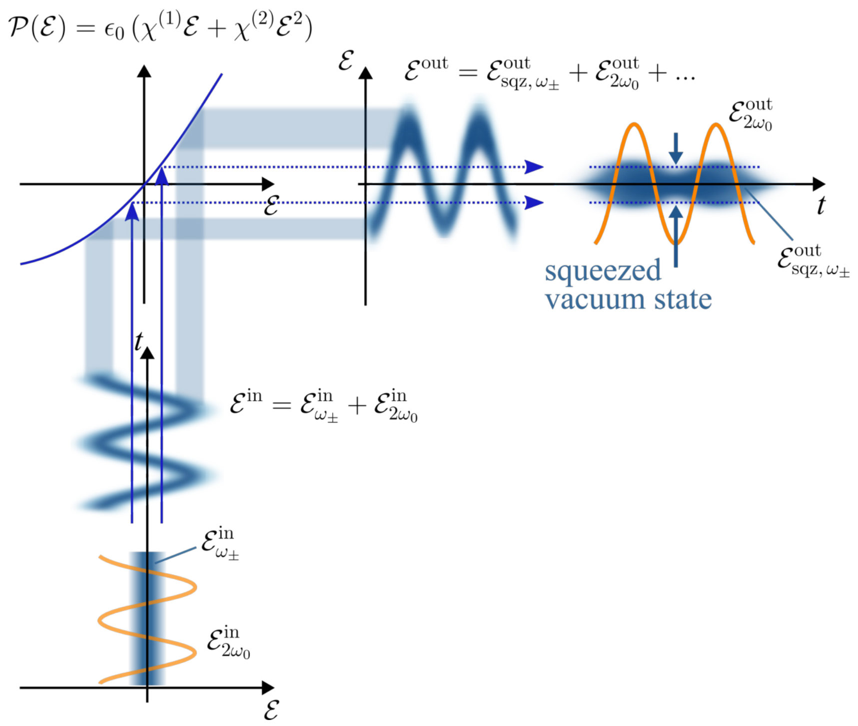

Figure 3.1.: Squeezed vacuum state generation in non-linear crystals. (Upper left corner) The crystals polarization $\mathcal{P}(\mathcal{E}) = \varepsilon_0 (\chi^{(1)}\mathcal{E} + \chi^{(2)}\mathcal{E}^2)$ describes the oscillations of electrons in a non-linear material excited by an electro-magnetic field $\mathcal{E}$. This plot illustrates how the input quantum field (from below) is converted into an output quantum field (towards the right). The input field is composed of a classical pump field $\mathcal{E}_{2\omega_0}$ at frequency $2\omega_0$ and vacuum fluctuations of a field $\mathcal{E}_{\omega_\pm}$ at frequency $\omega_\pm$. The superposition $\mathcal{E}^{\text{in}}$ of these two fields is transferred into a time dependent dielectric polarization. The latter is directly proportional to the electric component of the output field $\mathcal{E}^{\text{out}}$. The quantum uncertainty of the output fields show a phase dependent (parametric) amplification at frequency $2\omega_0$. The figure is adapted from [24, 51].

order polarization $\mathcal{P}^{(2)}(\mathcal{E}_{2\omega_0})$.

The OPA process occurs only in a small region of the crystal; the non-linear effect has to accumulate over the whole crystal length. Note that figure 3.1 displays the OPA process in such a small segment of the crystal. When all infinitesimal contributions of each segment constructively interfere, a noticeable conversion from

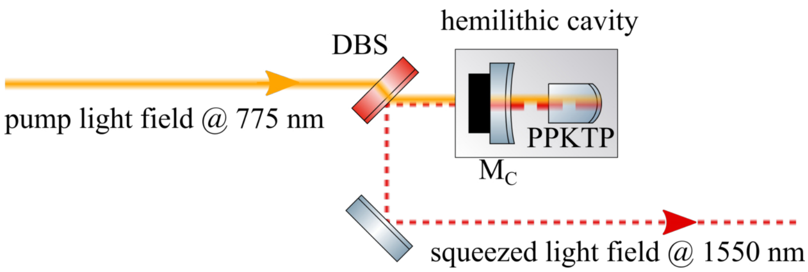

Figure 3.2.: Hemilithic cavity setup for squeezed light generation. The high reflective coated curved endface of the nonlinear crystal forms a hemilithic cavity with the coupling mirror M_c. This mirror is attached to a piezo-electric transducer to stabilize the cavity resonance to the fundamental field. The second harmonic pump field at a wavelength of 775 nm enters the cavity through the coupling mirror. The interaction of the polarizability with the electric field of the pump field inside the crystal generates the squeezed light at the fundamental wavelength of 1550 nm. Both fields are separated at a dichroic beam splitter (DBS), which is placed before the squeezed light source. The quasi phase matching condition between the fields is achieved by a periodically poling of the potassium titanyl phosphate (PPKTP). The conversion process is optimized by an active temperature stabilization of the crystal. This is achieved by surrounding the crystal with a copper block and thermally conducted with a thermo-electric cooler (TEC). Monitoring the temperature with a NTC-sensor and in combination with a temperature controller, a feed-back loop is implemented for the crystal phase-matching temperature (not shown).

the fundamental to the harmonic field is realized. This is achieved in the case of *phase matching*.

To ensure interaction of the fundamental and the second harmonic light field, they have to be co-propagating inside the crystal with the same speed. Only then the fields have a constant phase relation and are overlapping over the whole length of the crystal. Because the used material shows dispersion, the refractive index n for different frequencies are not equal $n(\omega_1) \neq n(\omega_2)$. If both fields are perfectly phase matched at the input of the crystal, the phases drift apart while propagating through the crystal. The created field at a point z_1 interferes destructively with a field created at another point z_2 inside the crystal. When c is the speed of light in vacuum, the conversion process is inverted after a coherence length

$$l_{\mathrm{coh}} = \frac{c}{4\omega_1(n(\omega_1) - n(\omega_2))}, \tag{3.3}$$

from which follows that the light power is back converted to the fundamental field. The *phase matching* condition is achieved, if all involved wave vectors $\vec{k}_i$ vanish, thus:

$$|\vec{k}_{\omega_+} + \vec{k}_{\omega_-} - \vec{k}_{2\omega}| = 0. \tag{3.4}$$

The subscripts ($\omega_\pm$) denotes the down-converted sideband photons from the parametric down-conversion process.

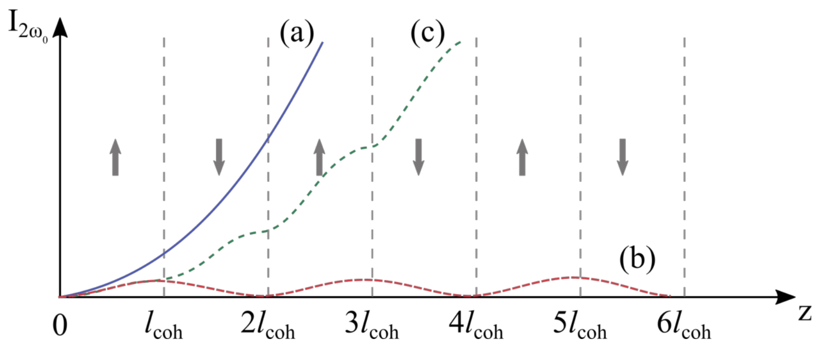

Figure 3.3.: Quasi phase matching condition for periodically poled birefringent crystals. The intensity $I_{2\omega}$ of the second harmonic field depends on the position z in the crystal. The curve (a) shows a perfect phase matching temperature. Ideally the intensity continuously increases over the whole crystal length. If instead no phase matching is present (b), the phases of the fundamental and second harmonic field drift apart while propagating along the crystal. After the coherence length l_{coh} the conversion process is inverted. The light power of the second harmonic is back converted to the fundamental field. The technique of quasi phase matching (c) counteracts this effect by using a periodically poled crystal. The poling is indicated by the arrows, which show the susceptibility relative to each other. Since the width of the poling matches the coherence length l_{coh}, the phase mismatches decreases and the conversion start to rise again (adapted from [52]).

Since the second order susceptibility is many orders of magnitudes smaller then first order, the intensity of the light is increased by a cavity. Thus the process of parametric amplification is enhanced. A schematic of the ordinary cavity design for squeezed light generation is shown in figure 3.2. The hemilithic cavity consisting of the high reflective coated and curved end face of the crystal and the coupling mirror $\mathrm{M_c}$. In contrast the front face of the crystal is plane and anti-reflective (AR) coated for both wavelength to reduce the intra-cavity losses. The second harmonic field at 775 nm (pump light field) is fully transmitted through the dichroic beam splitter (DBS), which is high reflective for 1550 nm at the same time, and entering the cavity through the coupling mirror. The exiting squeezed light is reflected on the DBS and available for subsequent experiments.

There are commonly used techniques to achieve phase matching in birefringent materials (*Type I (II) phase matching*) with different polarization of the fundamental and the harmonic light. Here the temperature dependence of the refractive index for the two wavelengths is exploited. In contrast, both the squeezed light source and the second harmonic generation in this thesis use the type-0 conversion. The involved fields are polarized in the same direction. In this case *quasi-phase matching* with a periodically poled medium enables the possibility of phase matching. The figure 3.3 shows the effect of quasi phase matching in a periodically poled birefringent crystal. It is composed of alternating sections with inverted susceptibility to each other. This is indicated by the arrows. The width matches the coherence length l_{coh}. Instead of the back conversion after the length l_{coh}, the phase mismatch is compensated due to the poling. The intensity of the fundamental field is continuously increased while propagating through the crystal over the whole length. Since the medium expands with temperature, the sections depending also on temperature. At the 'phase matching temperature' each length of the sections is equal to the coherence length, which provide the best conversion efficiency.

3.2. Preparation of squeezed light

The following section shows the schematic of the experimental laser preparation to create (entangled) squeezed states of light, which is set up during this thesis.

The overview displays the common foundation for the experiments performed and presented in chapter 4, 5 and 6. Essential different experimental requirements are presented in the respective chapter. This also includes technical details for the stabilization schemes.

3.2.1. Laser light preparation

The setup in figure 3.4 is segmented into several preparation stages, where different colored boxes highlight each step.

Laser preparation (light gray box): The first stage of the setup contains the main laser light source, which is a fiber laser at the telecommunication wavelength of 1550 nm and which provides about 700 mW of laser power. The combination of the quarter and the half wave plates eliminates any residual elliptical polarization of the fiber output laser light and is adjusted to the linear polarization of the input polarization beam splitter of a Faraday isolator (FI). It protects the laser from back-reflected light, which would otherwise causes disturbances, e.g. in form of frequency instabilities (in fact before any cavity a FI is placed). This is followed by a triangular cavity (premode cleaner) used as a spatial filter and a passive low pass filter suppressing the initial amplitude and phase noise of the laser above the resonance line width of the cavity. The resulting beam is in a well-defined TEM_{00}-mode. After that the laser light is distributed to the next stages via two polarization beam splitters (PBS_1 and PBS_2).

Second harmonic generation (blue box): Most of the light (about 600 mW) is sent via PBS_2 to the second harmonic generation (SHG) that provides the pump light for the squeezed light source. The setup is similar to the squeezer design (see figure 3.2) but used as an optical parametric amplifier above the threshold, which generates bright laser light at 775 nm. The beam splitter BS_2 distributes the (mode filtered) pump light to operate two squeezed light sources with a maximum pump power of 180 mW each.

Balanced homodyne detection (green box): About 30 mW is used for the local oscillator (LO) at the balanced homodyne detectors, to measure the light from the squeezed light source. In fact, the light propagates through many optical elements that cause distortion of the mode's shape. To achieve an optimal mode overlap at the 50:50 beamsplitter, we also use an additional mode cleaner before the LO reaches the detector. Optionally, the symmetric beam splitter BS_1 sends half of the light to a second balanced homodyne detector.

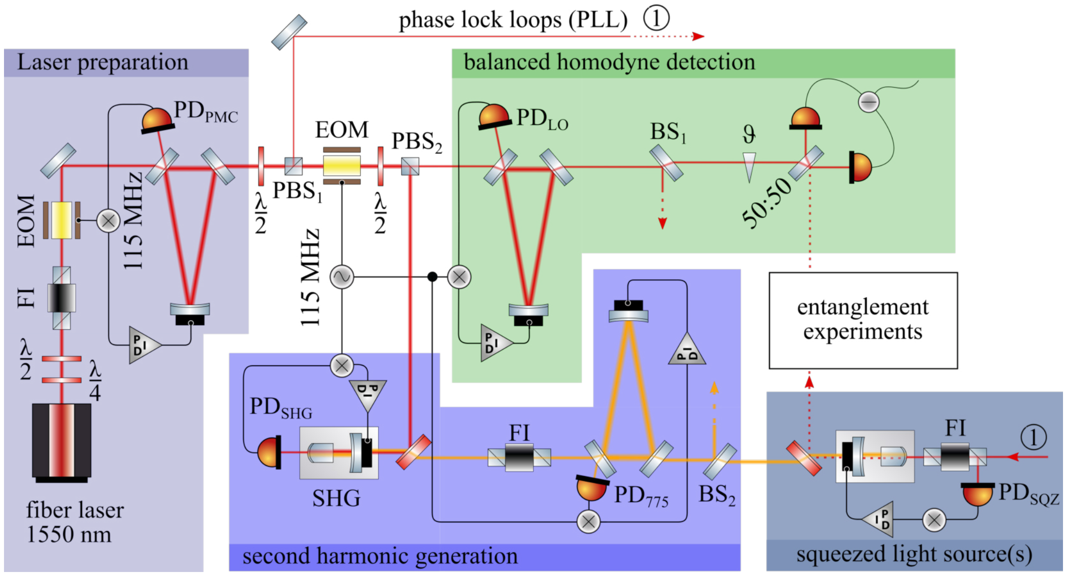

Figure 3.4.: Schematic diagram of the squeezed light preparation. The experimental setup shows the laser light preparation to produce and detect squeezed states of light. It consists of different steps, which are highlighted by different colored boxes (see main text). The first stage contains the preparation and distribution of the main laser source. Most of the light (600 mW) is sent to the second harmonic generation that provides the pump light fields for two squeezed light sources. About 30 mW is used for the local oscillator at the balanced homodyne detectors. A tiny fraction is tapped off at PBS_1 and sent to acoustic optical modulators (AOMs) to implement phase lock loops for the phase stabilization of the pump field, and readout phase of the homodyne detectors (not shown here, see 3.2.2 and 3.2.3).

Squeezed light source (dark grey box): A tiny fraction of sub-milliwatt laser light is tapped off at PBS_1 for the single sidebands and control beams. Those are employed for further phase lock loops (PLL), realizing stabilization schemes for the squeezed light source(s) and the readout phase ϑ of the homodyne detector as presented in the next sections. For the experiments presented in chapter 4 and 5 a single squeezed light source is sufficient, while for the experiment in chapter 6 two are necessary.

The cavities lengths are stabilized to the resonance for the 1550 nm light using Pound-Drever-Hall locking scheme [53]. This is realized with a feedback loop, detecting the phase modulated light with the respective photodiode PD_{PMC}, PD_{SHG}, PD_{LO}, and PD_{SQZ}. An exception is the mode cleaner for the pump light, which is stabilized to 775 nm light using PD_{775}. The generated squeezed light is guided to the downstream experiment, which is subsequently analyzed with the balanced homodyne detector.

3.2.2. Squeezed light source

With the setup depicted in figure 3.5 an electro-optical phase stabilization is established for the squeezed light source(s). A control beam carried a phase modulation at a sideband frequency of 33.9 MHz (35.5 MHz for the second squeezed light source), which is coupled into the cavity through the high-reflective coupling mirror M_c. The reflectivity is 90 % for 1550 nm and 20 % for 775 nm. The back reflected light is separated from the incoming light by a combination of a Faraday isolator and a polarizing beam splitter. The light is detected with the resonant photodiode $PD_{33.9\,(35.5)}$. Demodulating the photodiodes signal at the same frequency (33.9 MHz or 35.5 MHz) provides an error signal, whose zero crossing corresponds to the cavities' resonance for the pump field. By demodulating the signal in the orthogonal quadrature (indicated by the 'sin' and 'cos' next to the demodulation symbol) an error signal for the phase of the pump field with respect to the control beam is generated. The phase of the pump is actuated by the phase shifter PS_{pump} and set to a phase angle, where the control beam is deamplified. Additionally two tap-offs of a few µW are shifted with an acoustic-optic modulator (AOM) by 78 MHz and 82 MHz, respectively.

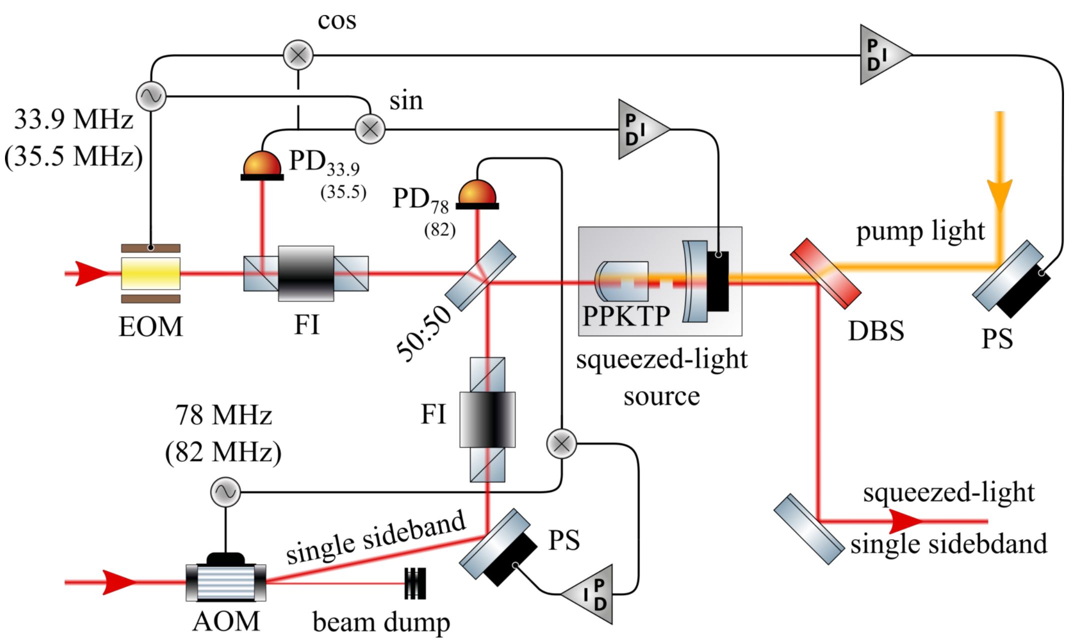

Figure 3.5.: Electro-optical phase stabilization of a squeezed light source. The cavity length is stabilized to resonance for the 1550 nm field using a Pound-Drever-Hall locking scheme. A control beam carrying a phase modulation from an electro-optical modulator (EOM) at a side band frequency of 33.9 MHz (or 35.5 MHz for second source). Those are coupled into the cavity and the back reflected light is separated from the incoming light with a Faraday isolator (FI) and detected with the resonant photodiode $PD_{33.9}$. Thus a Pound-Drever-Hall locking scheme is implemented to stabilize the length of the squeezed light source cavity to resonance of the 1550 nm light. Additionally, by demodulating the photodiodes signal 90 degrees out of phase with respect to the cavity lock, the pump lights phase could also be stabilized with the same photodiode. The single sideband is generated by an acousto-optical modulator (AOM), which is superimposed with the control light and phase locked to it. Thereby a phase reference for the squeeze angle is established. A similar figure is published in [20].

These single sidebands (SSB) are superimposed with one of the respective control beams of the squeezed-light source at 50:50 beam splitter in front of the cavity. The interference is measured at the second output with the resonant photodetector $PD_{78\,(82)}$ and demodulated at the corresponding sideband frequency. Using the phase shifter PS_{SSB} the generated sinusoidal error signal established a phase lock between the SSB and the control beam. Because the pump phase is the reference for the squeeze angle and is also phase locked to the control field, a fixed phase relation between the SSB and the squeezed quadrature is established.

3.2.3. Balanced homodyne detection

Due to electronic limitations in photo-electric detection, it is challenging to resolve optical light fields, oscillating at frequencies of several hundreds of terahertz. Instead, we can measure variations around the averaged optical field oscillation on longer time-scales. However, in order to access the noise properties of the quadratures fields $\hat{X}$ and $\hat{Y}$, introduced in chapter 2, a rather simple interference setup is used; the technique of balanced homodyne detection, as it is depicted in figure 3.6.

To analyze the quadratures of the signal field at a frequency $\omega_0 \pm \Omega$ with this method, it is superimposed on a symmetric (50:50) beam splitter with a strong coherent field at the carrier frequency ω_0 with the same mode parameters. This is the so called *local oscillator* (LO). After the fields interfere, the two output ports' intensities $\hat{i}_1$ and $\hat{i}_2$ are simultaneously monitored with two PIN photodetectors. The photo currents are subsequently electronically subtracted. Hence, this is proportional to the respective quadrature measurement of the signal field. To see that mathematically, we need to remember that any field operator $\hat{O}$ can be decomposed into its coherent classical part with the amplitude $O = \langle \hat{O} \rangle$ and its quantum fluctuation part $\delta\hat{O}$. Therefore the signal field is given by $\hat{a}_\mathrm{s} = \alpha_\mathrm{s} + \delta\hat{a}_\mathrm{s}$ and the the LO is given by $\hat{a}_\mathrm{LO} = (\alpha_\mathrm{LO} + \delta\hat{a}_\mathrm{LO})e^{\mathrm{i}\vartheta}$. By separating the relative phase ϑ between the LO and the signal field due to the additional factor $e^{\mathrm{i}\vartheta}$ explicitly assigned to the LO, the complex amplitudes α and α_LO now are made real.

The interference of the input states at the beam splitter transforms according to equation 2.59, so that the outputs states are

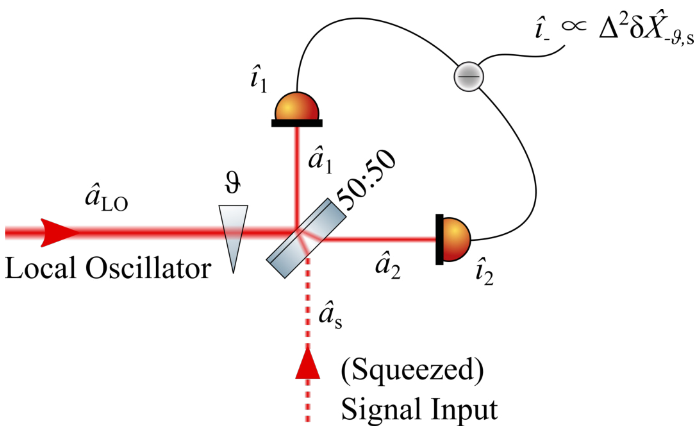

Figure 3.6.: Balanced Homodyne Detection scheme. The quadrature of the signal field $\hat{a}_s$ is measured by superimposing it with a strong local oscillator $\hat{a}_{\rm LO}$ with equal mode parameters on a 50:50 beam splitter. Subsequently, the current of the detected output fields $\hat{a}_1$ and $\hat{a}_2$ from two PIN photodiodes are subtracted. In the approximation of a strong local oscillator the subtracted current is proportional to the noise characteristic of the signal field, whereas the choice of quadrature is selected by the relative phase angle $\vartheta \in [0, \pi/2]$.

$$\hat{a}_1 = \frac{1}{\sqrt{2}}\left(\hat{a}_{\rm LO}e^{\mathrm{i}\vartheta} + \hat{a}_{\rm s}\right), \tag{3.5}$$

$$\hat{a}_2 = \frac{1}{\sqrt{2}}\left(\hat{a}_{\rm LO}e^{\mathrm{i}\vartheta} - \hat{a}_{\rm s}\right). \tag{3.6}$$

The induced photo current $\hat{\imath}_1$ and $\hat{\imath}_2$ of the photo diodes are proportional to the number of photons contained in the light field, thus the intensities can be approximated by

$$\begin{aligned}\hat{\imath}_1 \propto \hat{a}_1\hat{a}_1^\dagger = &\frac{1}{2}\left(\hat{a}_{\rm LO}e^{\mathrm{i}\vartheta} + \hat{a}_{\rm s}\right)\left(\hat{a}_{\rm LO}e^{-\mathrm{i}\vartheta} + \hat{a}_{\rm s}\right)\\ \approx &\frac{1}{2}\Big[\alpha_{\rm s}^2 + \alpha_{\rm LO}^2 + 2\alpha_{\rm s}\alpha_{\rm LO}\cos(\vartheta)\\ &+ \alpha_{\rm s}\left(\delta\hat{X}_1^a + \delta\hat{X}_{-\vartheta}^b\right) + \alpha_{\rm LO}\left(\delta\hat{X}_1^b + \delta\hat{X}_\vartheta^a\right)\Big],\end{aligned} \tag{3.7}$$

and

$$\begin{aligned}\hat{i}_2 \propto \hat{a}_2\hat{a}_2^\dagger &= \frac{1}{2}\left(\hat{a}_{\mathrm{LO}}e^{\mathrm{i}\vartheta} - \hat{a}_{\mathrm{s}}\right)\left(\hat{a}_{\mathrm{LO}}e^{-\mathrm{i}\vartheta} - \hat{a}_{\mathrm{s}}\right)\\ &\approx \frac{1}{2}\Big[\alpha_{\mathrm{s}}^2 + \alpha_{\mathrm{LO}}^2 - 2\alpha_{\mathrm{s}}\alpha_{\mathrm{LO}}\cos(\vartheta)\\ &\qquad + \alpha_{\mathrm{s}}\left(\delta\hat{X}_1^a - \delta\hat{X}_{-\vartheta}^b\right) + \alpha_{\mathrm{LO}}\left(\delta\hat{X}_1^b - \delta\hat{X}_{\vartheta}^a\right)\Big]. \end{aligned} \tag{3.8}$$

Here we used the definition of the quadratures in 2.5 and the generic quadrature in 2.13. Additionally, we considered a linearization of the detected fields in the form that all higher order terms are neglected, like the quadratic fluctuation terms $\delta\hat{a}_{\mathrm{s}}\delta\hat{a}_{\mathrm{s}}^\dagger$. This is justified because the fluctuation terms are small compared to the intense local oscillator light field. In the last step the subtracted photo current is

$$\hat{i}_- \propto \hat{a}_1\hat{a}_1^\dagger - \hat{a}_2\hat{a}_2^\dagger = 2\alpha_{\mathrm{s}}\alpha_{\mathrm{LO}}\cos(\vartheta) + \alpha_{\mathrm{s}}\delta\hat{X}_{\vartheta,b} + \alpha_{\mathrm{LO}}\delta\hat{X}_{-\vartheta,a}, \tag{3.9}$$

that relates the detection to the quadrature of the signal. Since the first term of the above equation describes the interference between the DC parts of both fields, they do not contribute to the noise. The variance of $\hat{i}_-$ is given by

$$\Delta^2\hat{i}_- \propto \alpha_{\mathrm{s}}\Delta^2\delta\hat{X}_{\vartheta,\mathrm{LO}} + \alpha_{\mathrm{LO}}\Delta^2\delta\hat{X}_{-\vartheta,s}, \tag{3.10}$$

which shows the significant aspects of balanced homodyne detection. Each fluctuation term of its corresponding field is amplified by the other field's coherent excitation, respectively. By adjusting the relative phase ϑ between the signal and LO field, one can observe $\hat{X}$ or $\hat{Y}$ individual in a single measurement or any linear combination $\hat{X}_\vartheta = \hat{X}\cos(\vartheta) + \hat{Y}\sin(\vartheta)$. To set the homodyne detector to any angle ϑ, the phase is precisely controlled using the SSB, accompanying the squeezed light, and beating with the LO (cf. figure 6.5).

Since the interesting property is the signals noise characteristic, we should choose a regime where the LO is much stronger than the amplitude of the signal, such that $|\alpha_{\mathrm{LO}}| \gg |\alpha_{\mathrm{s}}|$. Then the noise contribution of the first term is negligible. In the case of detecting squeezed vacuum fields with $|\alpha_{\mathrm{s}}| = 0$ this condition is fulfilled. However, in reality, in some of our experiments, we have control beams co-propagating with the squeezed field. Therefore the noise contribution of the LO field can influence the detected noise again.

To analyze the signal obtained from the subtracted photo current, we can use either a time-resolving device, e.g. a data acquisition card or analyze the spectral power density with a spectrum analyzer.

4. Demonstration of a 10 dB quantum-noise squeezed interferometer

The purpose of laser interferometers is to continuously monitor small relative phase changes of an optical path with respect to a reference path. In practice, it splits a beam of a coherent light wave into two partial beams on a balanced beam splitter. They propagate along different paths afterward and eventually let them superimpose again. At this point superposition causes the phenomenon of interference, which produces intensity variations of the output light.

For the performance of any interferometric measurement, the spatial overlap of the interfering beams, which determines the contrast (visibility) of the interferometer, as well as noise arising from power fluctuations of the input light are important factors. Likewise, back scattered light inside the interferometer and mirror surface displacements in terms of thermal loads are essential to detect the interferometers signal with a minimum amount of loss. However, to analyze the fundamental precision of monitoring the phase difference between the paths arising in interferometric measurements in a purely classical way is not possible. In particular within its description, where both the light and detection process is treated purely classical, the intensity of light is precisely determined. The measurement of the intensity reaches arbitrary precision that also allows to measure arbitrary small phase shifts in an interferometric experiment. In reality we have to consider a semi-classical theory in which the light interferes as classical waves, but the detection process are quantized [24]. Instead of measuring continuous intensity of light, the number of energy quanta (photons) is being measured in photo-electric detection. The absorption process reveal a stochastic character due to the random number n of photons arriving at the photodiode in each measurement interval per unit time. This is described by the standard Poissonian counting statistic (cf. chapter 2). The uncertainty of the distribution is the *photon counting noise* of mutually independent photons and usually referred to as *shot noise*. With particular focus on the signal-to-noise ratio SNR$= N/\sqrt{N} = \sqrt{N}$, it becomes clear that the ratio increases with the square root of the total number N of photons captured. Although the shot noise increases in absolute terms, its relative fraction is less at higher signal levels. Consequently, it is substantially more relevant for less signal captured.

Modern versions of interferometers range from length measurements in spectroscopic interferometric experiments [54, 55] to the most prominent examples including the gravitational wave detectors (GWD). The latter are Michelson-type laser interferometers operating close to the dark fringe. The differential change of the phase quadrature between the two arms is transferred into an amplitude quadrature change of the interferometer's output light. Consequently the power change at the output is detected by a single photodiode.

In GWDs the signal-to-shot noise ratio has been reduced by increasing light power, while at the same time technical noise sources were reduced to very low levels. Nevertheless it is still required to further reduce the shot noise. But achieving higher sensitivities by increasing the light power is already challenging due to optical heating processes, stray light and radiation pressure noise [56]. One way to surpass the shot noise limit can be achieved by using quantum correlations, as first proposed by C.M. Caves in 1981 [23]. Injecting a squeezed vacuum state through the shot noise dominated interferometer's output port increases the sensitivity without increasing the laser power.

The application of squeezed light in gravitational-wave detectors is already used and intensively studied in GEO600 since 2011 [25, 26], and was more recently also implemented in advancedLIGO [28] and VIRGO [29]. This resulted in gravitational-wave observations with higher sensitivities since April 2019. All current GWDs are operated with high-power and quasi-monochromatic continuous wave laser light at a wavelength of 1064 nm. For the next generation of future cryogenic GWD, e.g. the Einstein-telescope, it will be necessary to go to longer wavelengths, where 1550 nm laser light [57–59] is a seminal candidate. High squeezing values of 13 dB in the regime of MHz frequencies at 1550 nm, and about 10 dB in the audio band have been realized in [21]. Especially the technique of squeezed light injection is essential for the design of the low frequency interferometer of the Einstein-Telescope (1 Hz-250 Hz). To reduce the thermo-optical noise of the interferometer's optical components to an acceptable level in this low frequency band, it will operate at cryogenic temperatures. Even low residual absorption of the dielectric mirror coatings deposits a significant amount of thermal energy in the mirrors. Due to the seismic isolation (suspension of the mirrors) it is difficult to dissipate the heat. This imposes a limit to the maximum circulating optical power, which is planned to be 18 kW in the arm cavities. Because of its excellent mechanical and thermal properties, silicon has been proposed as one candidate for the test mass materials. When silicon is used in the interferometer, the operational wavelengths has to be at 1550 nm as used here.

In this part of my thesis I experimentally show the quantum enhancement by applying squeezed light to a Mach-Zehnder interferometer (MZI) and demonstrates that high squeezing values are indeed realistic in interferometric measurements operating at wavelengths at 1550 nm.

4.1. Quantum-enhanced Mach-Zehnder interferometer

In the first instance, we will explore the fundamental limit in high-precision interferometric phase-sensing measurements in the theoretical framework of the semi-classical model. We will restrict ourselves to the conventional MZI's two particularly relevant situations with coherent light and the quantum enhancement due to applying squeezed light. Afterwards the theoretical prediction will be experimentally verified.

The discussion here is based on [60] and [61], and starts with the conventional MZI using coherent light. Figure 4.1 illustrates the MZI configuration, where an intense coherent field enters one input and is separated into two parts after passing a balanced beam splitter (BS). At the second input, the ground-state uncertainty of the overlapping mode enters and the phases ϕ_{a} and ϕ_{b} (corresponding to rotation in phase space) are assigned to both parts. By superimposing both parts on a second

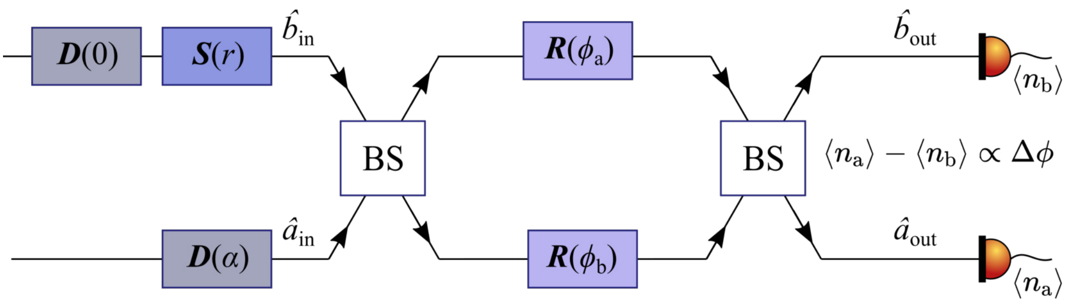

Figure 4.1.: Principle of phase-sensing measurement based on a Mach-Zehnder interferometer. The MZI transforms the two input states $\hat{a}_{\mathrm{in}}$ and $\hat{b}_{\mathrm{in}}$ into the output states $\hat{a}_{\mathrm{out}}$ and $\hat{b}_{\mathrm{out}}$, where the photon numbers $\langle n_{\mathrm{a}}\rangle$ and $\langle n_{\mathrm{b}}\rangle$ per time window (time-frequency mode) are measured with two single photodiodes, respectively. The difference of the photocurrents is proportional to the interferometer signal (without noise). In the standard configuration, the input mode $\hat{a}_{\mathrm{in}}$ is an intense coherent field $\boldsymbol{D}(\alpha)$, while vacuum $\boldsymbol{D}(0)$ (no squeezing $\boldsymbol{S}(r) = \mathbb{1}$) is entering the second input port of the balanced beam splitter BS. Inside the MZI each mode experience a phase shift according to a rotation $\boldsymbol{R}(\phi_{\mathrm{a}})$ and $\boldsymbol{R}$ (ϕ_{b}).

beam splitter, the average photon numbers $\langle n_{\mathrm{a}}\rangle = \langle \hat{a}_{\mathrm{out}}\hat{a}_{\mathrm{out}}{}^{\dagger}\rangle$ and $\langle n_{\mathrm{b}}\rangle = \langle \hat{b}_{\mathrm{out}}\hat{b}_{\mathrm{out}}{}^{\dagger}\rangle$ of the outgoing fields at the interferometers output are measured with two single photodiodes. The smallest detectable phase difference between the two arms is proportional to the difference of the measured average photon numbers. In general, the input and output relation of the annihilation operator is described by the combined action of the beam splitter and the phase shifts transformation, like:

$$\begin{aligned}\begin{pmatrix}\hat{a}_{\mathrm{out}}\\ \hat{b}_{\mathrm{out}}\end{pmatrix} &= \frac{1}{2}\begin{pmatrix}1 & i\\ i & 1\end{pmatrix}\begin{pmatrix}e^{i\phi_{\mathrm{a}}} & 0\\ 0 & e^{i\phi_{\mathrm{b}}}\end{pmatrix}\begin{pmatrix}1 & -i\\ -i & 1\end{pmatrix}\begin{pmatrix}\hat{a}_{\mathrm{in}}\\ \hat{b}_{\mathrm{in}}\end{pmatrix}\\ &= e^{i(\phi_{\mathrm{a}}+\phi_{\mathrm{b}})/2}\begin{pmatrix}\cos(\phi/2) & -\sin(\phi/2)\\ \sin(\phi/2) & \cos(\phi/2)\end{pmatrix}\begin{pmatrix}\hat{a}_{\mathrm{in}}\\ \hat{b}_{\mathrm{in}}\end{pmatrix},\end{aligned} \tag{4.1}$$

where $\phi = \phi_{\mathrm{a}} - \phi_{\mathrm{b}}$ is the differential phase shift between the two arms (here a phase shift of $-\pi/2$ or $\pi/2$ on each beam splitter is considered). The common phase has no relevance for further discussion here and will be therefore omitted. In the recent literature the standard configuration of the MZI is related to the group of SU(2) and is therefore called a SU(2)-interferometer [60–62]. Consequently, the action of the beam splitter and phase shifters on arbitrary states can be visualized by rotations in an abstract three dimensional vector space, spanned by the hermitian Jordan-Schwinger operators

$$\hat{J}_{\mathrm{x}} = \frac{1}{2}(\hat{a}^{\dagger}\hat{b} + \hat{b}^{\dagger}\hat{a}), \tag{4.2a}$$

$$\hat{J}_{\mathrm{y}} = \frac{i}{2}(\hat{b}^{\dagger}\hat{a} - \hat{a}^{\dagger}\hat{b}), \tag{4.2b}$$

$$\hat{J}_{\mathrm{z}} = \frac{1}{2}(\hat{a}^{\dagger}\hat{a} + \hat{b}^{\dagger}\hat{b}), \tag{4.2c}$$

in direct analogy to the mathematical concept of spin algebra in atomic physics. This representation allows describing spin squeezed states, which are also a powerful quantum resource to enhance atom interferometers' precision [63–65]. However, our focus relies on the description in optical interferometry.

The operators satisfy the commutation relation in terms of two bosonic operators $[\hat{J}_i, \hat{J}_j] = i\varepsilon_{ijk}\hat{J}_k$. In the $\hat{J}_i$ representations the effect of an MZI on the two input states transforms according to the unitary matrix U = exp(-i $\alpha\hat{\mathbf{J}}$), where $\hat{\mathbf{J}}$ = $\{\hat{J}_{\mathrm{x}}, \hat{J}_{\mathrm{y}}, \hat{J}_{\mathrm{z}},\}$ and α describes the angle of axis rotation, respectively. We obtain

$$\begin{aligned}
\begin{pmatrix} \hat{J}_{\mathrm{x,\,out}} \\ \hat{J}_{\mathrm{y,\,out}} \\ \hat{J}_{\mathrm{z,\,out}} \end{pmatrix} &= \begin{pmatrix} 1 & 0 & 0 \\ 0 & 0 & 1 \\ 0 & -1 & 0 \end{pmatrix} \begin{pmatrix} \cos(\phi) & -\sin(\phi) & 0 \\ \sin(\phi) & \cos(\phi) & 0 \\ 0 & 0 & 1 \end{pmatrix} \begin{pmatrix} 1 & 0 & 0 \\ 0 & 0 & -1 \\ 0 & 1 & 0 \end{pmatrix} \begin{pmatrix} \hat{J}_{\mathrm{x,\,in}} \\ \hat{J}_{\mathrm{y,\,in}} \\ \hat{J}_{\mathrm{z,\,in}} \end{pmatrix} \\
&= \begin{pmatrix} \cos(\phi) & 0 & \sin(\phi) \\ 0 & 1 & 0 \\ -\sin(\phi) & 0 & \cos(\phi) \end{pmatrix} \begin{pmatrix} \hat{J}_{\mathrm{x,\,in}} \\ \hat{J}_{\mathrm{y,\,in}} \\ \hat{J}_{\mathrm{z,\,in}} \end{pmatrix},
\end{aligned} \tag{4.3}$$

from which follows that in particular the balanced beam splitter performs a $\pi/2$-rotation around the x- axis, while the phase shift correspond to a rotation around the z- axis by an angle ϕ. Overall the sequence of all operations is a rotation of $\hat{\mathbf{J}}$ around the y- axis by an angle ϕ.

In this formalism the difference of photon numbers detected by the two single photodiodes is related to a measurement of $\hat{J}_\mathrm{z} = (\hat{n}_\mathrm{a} - \hat{n}_\mathrm{b})/2$, which allows us to estimate the uncertainty of the phase precision. In order to access the phase sensitivity, it is necessary to calculate the mean value of $\hat{J}_\mathrm{z}$ in dependence of the input states, that is

$$\langle \hat{J}_{\mathrm{z,\,out}} \rangle = \cos(\phi)\,\langle \hat{J}_{\mathrm{z,\,in}} \rangle - \sin(\phi)\,\langle \hat{J}_{\mathrm{z,\,in}} \rangle\,, \tag{4.4}$$

with variance

$$\begin{aligned}\Delta^2 \hat{J}_{\mathrm{z,\,out}} = \sin^2(\phi)\,\langle {\hat{J}^2}_{\mathrm{z,\,in}} \rangle + \cos^2(\phi)\,\langle {\hat{J}^2}_{\mathrm{z,\,in}} \rangle \\ - \sin(\phi)\cos(\phi)(\langle \hat{J}_{\mathrm{x,\,in}} \hat{J}_{\mathrm{z,\,in}} + \hat{J}_{\mathrm{z,\,in}} \hat{J}_{\mathrm{x,\,in}} \rangle - 2\,\langle \hat{J}_{\mathrm{x,\,in}} \rangle\,\langle \hat{J}_{\mathrm{z,\,in}} \rangle)\,.\end{aligned} \tag{4.5}$$

The last term describes the correlation between the input states of the interferometer which are assumed to be uncorrelated and therefore equal to zero. The phase uncertainty $\Delta\phi$ can be quantified by error propagation theory via the formula

$$\Delta\phi = \frac{\Delta \hat{J}_\mathrm{z}}{\left|\frac{d\langle \hat{J}_\mathrm{Z} \rangle}{d\phi}\right|}\,. \tag{4.6}$$

This simple approach provides a good approximation for the performance of interferometers and thus can be consider to analyze the effect of different input states on the phase fluctuation in general.

4.1.1. Coherent light interferometer

In the conventional configuration of the interferometer, a coherent field with complex amplitude α is injected in one input port of the beam splitter, while the second input is unused and only vacuum fluctuations are entering the interferometer. Using the equations 4.4 and 4.5 to calculate the relevant quantities

$$\langle \hat{J}_{\mathrm{z,\,in}} \rangle = \frac{1}{2}|\alpha|^2 \quad \text{and} \quad \langle \hat{J}_{\mathrm{x,\,in}} \rangle = 0\,, \tag{4.7}$$

with variances

$$\Delta^2 \hat{J}_{\mathrm{z,\,in}} = \Delta^2 \hat{J}_{\mathrm{x,\,in}} = \frac{1}{4}|\alpha|^2\,, \tag{4.8}$$

we obtain the information about the phase uncertainty from equation 4.6

$$\Delta\phi = \frac{\frac{1}{2}|\alpha|}{\frac{1}{2}|\alpha|^2|\sin(\phi)|} = \frac{1}{\sqrt{\langle N\rangle}|\sin(\phi)|}, \tag{4.9}$$

where the complex amplitude is replaced by the average photon number $\langle N\rangle = |\alpha|^2$ of the coherent input field. For phases $\phi = \pi/2$ and $\phi = 3\pi/2$ equation 4.9 represents the shot noise limit of the phase uncertainty in high precision phase-sensing. It depends on the average number of quanta in the input mode, which is following a Poissonian probability distribution. The precision $\Delta\phi$ is the smallest phase difference that is resolvable with a signal-to-noise ratio of 1 when using $\langle N\rangle$ mutually independent photons per measuring time interval. Therefore it is essential for an ideal precise measurements of the phase to use as much quanta as possible as a consequence of the shot noise scaling $1/\sqrt{\langle N\rangle}$. For this reason GWDs use as much laser power in the arms as possible [24].

4.1.2. Coherent light interferometer with squeezed light

One strategy to surpass the shot noise limit in equation 4.9 and to enhance the phase sensitivity is to use quantum correlated photons. In practice this is realized by injecting squeezed light into the unused port of the interferometer [23]. To see that, we require the same quantities as shown in equation 4.7 and 4.8 before. Also we have to take into account that a squeezed vacuum state (r > 0) has always a non-zero photon number. Overlapping a squeezed vacuum state with a coherent displacement further adds photons on average. Thus we have the average photon number [60]

$$\langle \hat{N}\rangle = |\alpha|^2 + \sinh^2(r)\,, \tag{4.10}$$

where the relevant quantities now read

$$\langle J_{\mathrm{z,\,in}}\rangle = \frac{1}{2}\left(|\alpha|^2 - \sinh^2(r)\right) \quad \text{and} \quad \langle J_{\mathrm{x,\,in}}\rangle = 0\,, \tag{4.11}$$

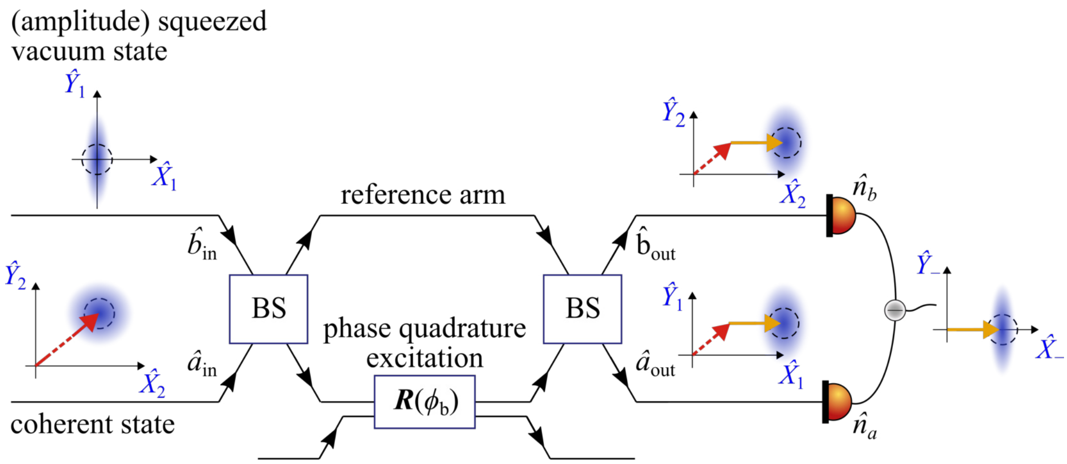

Figure 4.2.: Squeezed light enhanced Mach-Zehnder interferometer. Shown is the concept of a quantum enhanced MZI and phase space pictures with quantum uncertainty at the in- and output ports of the interferometer. Superimposing a (amplitude) squeezed vacuum state at the beam splitter (BS) with an intense coherent state generates quantum correlations between the two output ports. The quantum noise in the two arms are entangled with each other and therefore cancel out. Thus, after recombination at the second beam splitter and detecting the path difference with a signal reveals an improved signal-to-noise ratio of the interferometer. Both output ports are detected with a photodiode, respectively. The actual interferometers signal (yellow arrows) is provided by the difference photo-voltage with an amplitude squeezed noise characteristic as the phase space picture with $\hat{X}_-$ and $\hat{Y}_-$ shows.

with the respective variances

$$\begin{aligned}\Delta^2 J_{\text{z, in}} &= \frac{1}{4}\left(|\alpha|^2 + \frac{1}{2}\sinh^2(2r)\right),\\ \Delta^2 J_{\text{x, in}} &= \frac{1}{4}\left(|\alpha|^2\cosh(2r) - \operatorname{Re}\left(\alpha^2\right)\sinh 2(r) + \sinh^2(r)\right).\end{aligned} \tag{4.12}$$

By choosing the phase of the coherent light, such that $\alpha = \operatorname{Re}\left(\alpha^2\right)$ is maximized, the variance $\Delta J_{\text{x, in}}$ gets minimized at the same moment. This is equivalent to the case where the phase of the coherent light is pointed in the direction in which the squeezed vacuum state possesses its lowest variance. According to this ideal scenario the expression of equation 4.6 provides the lower bound for the phase precision:

$$\Delta\phi = \frac{\sqrt{\cot^2(\phi)\left(|\alpha|^2 + \frac{1}{2}\sinh^2(2r)\right) + |\alpha|^2 e^{-2r} + \sinh^2(r)}}{\left||\alpha|^2 - \sinh^2(r)\right|}, \tag{4.13}$$

where by an appropriate selection of the phase $\phi = n\pi/2$, the first term under the square root vanishes and thus again indicates the optimal operation point of the interferometer for the phase estimation.

To compare the conventional interferometer with the quantum enhanced interferometer with squeezed light, the total average number of photons $\langle N \rangle$ entering the interferometer should be set to a fixed value. The majority of photons are dedicated to the coherent light. In the regime of $\langle N \rangle \gg 1$ the equation 4.13 complies approximately:

$$\Delta\phi = \frac{\sqrt{|\alpha|^2 e^{-2r} + \sinh^2(r)}}{\left||\alpha|^2 - \sinh^2(r)\right|} = \frac{\sqrt{e^{-2r} + \frac{\sinh^2(r)}{|\alpha|^2}}}{|\alpha| - \frac{\sinh^2(r)}{|\alpha|^2}} \approx \frac{1}{\sqrt{\langle N \rangle} e^r}, \tag{4.14}$$

where indeed the result shows that injecting squeezed light into a Mach-Zehnder interferometer returns an improved phase sensitivity compared to the shot noise scaling, as depicted in figure 4.3.

4.2. Demonstration of a quantum enhanced Mach-Zehnder interferometer

To demonstrate the improvement of the Mach-Zehnder interferometer due to squeezed states of light, the following experimental setup was implemented as illustrated in figure 4.4.

The structure of the interferometer itself consists of two balanced beam splitters and two highly reflective mirrors. Both arms had the same length of 37.5 cm. One input of the balanced beam splitter is used to inject coherent light into the interferometer with a light power of about P = 10.5 mW, while a squeezed vacuum state enters through the second input. The generated squeezed light at a wavelength

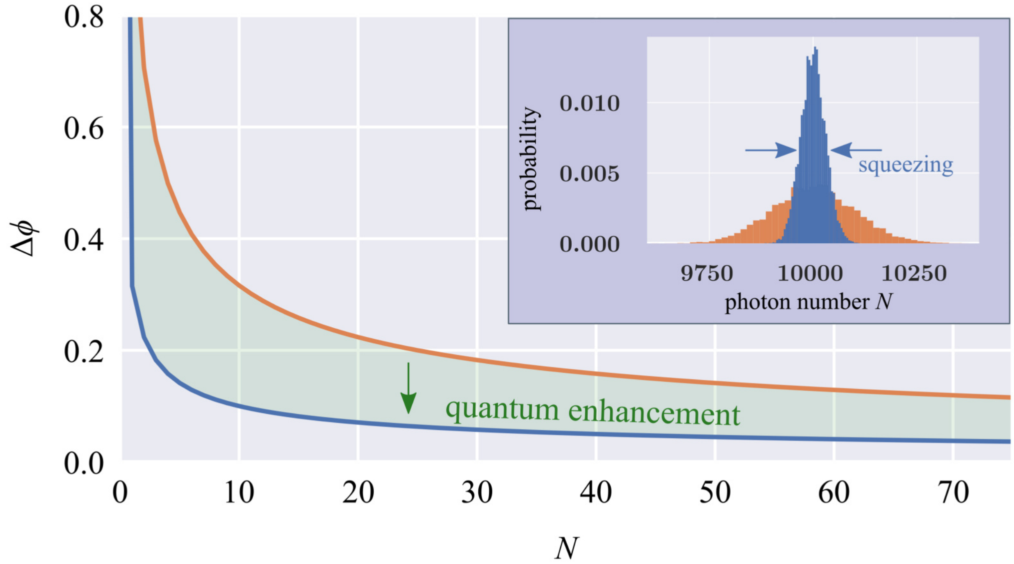

Figure 4.3.: Comparison of the phase precision scaling between the conventional and squeezed light enhanced interferometer. The phase uncertainty of the conventional interferometer scales with $\Delta\phi \propto 1/\sqrt{\langle N \rangle}$. By applying squeezed states of light, a better scaling of $\Delta\phi \propto 1/(\langle N \rangle\, \mathrm{e}^r)$ is achieved. The inset shows the counting statistics for a fixed average number of $\langle N \rangle = 10000$ per measurement time interval. The squeezed light (10dB) enhanced interferometer shows a standard deviation $\sqrt{10}$-smaller than $\pm\sqrt{N}$.

of 1550 nm was provided by one of the squeezed light sources outlined in chapter 3.

Figure 4.4 shows the schematic of the quantum enhanced Mach-Zehnder interferometer. Both arms contain a phase shifter (a highly reflective mirror attached to a piezo-electric transducer). In the upper arm, $\mathrm{PS}_{\phi_{\mathrm{MZI}}}$ enables the possibility to control the relative phase ϕ_{MZI} of the interferometer arms with a feedback loop. An error signal for the relative phase was generated by scanning the phase ϕ_{MZI}. The interferometer was locked to mid-fringe using the DC-output of the balanced detection. The mid-fringe corresponds to a phase $\phi_{\mathrm{MZI}} = \pi/2$ at which the interferometer is most sensitive for phase changes (see equation 4.9). Typically we use EOMs to produce modulation frequencies in the MHz regime of a light field. Due to its rather high optical loss this is not appropriate when squeezed light is used. Instead the phase

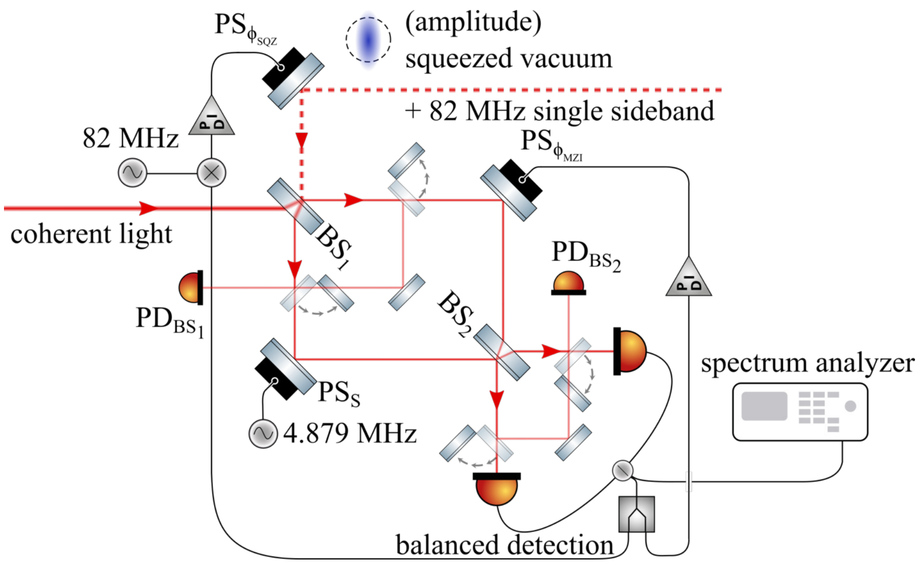

Figure 4.4.: Schematics of the quantum enhanced MZI. Squeezed light is injected into one port of the balanced beam splitter BS_1. To stabilize the phase ϕ_{SQZ} of the squeezed vacuum to the amplitude quadrature, a feedback loop with a single sideband at 82 MHz was implemented. The coherent light with a power of P = 10.5 mW is injected into the second input. A *signal* is generated at a Fourier frequency of f = 4.879 MHz with a piezo-actuated highly reflective mirror PS_S. By scanning the interferometers relative phase ϕ_{MZI} with the phase shifter $\mathrm{PS}_{\phi_{\mathrm{MZI}}}$ a lock was implemented. Therefore an error-signal is generated from the DC-output of the balanced detection, to lock the interferometer to mid-fringe ($\phi = \pi/2$). To analyze the signal at the output, both states in the arms are superimposed on a second balanced beam splitter (BS_2) and impinged on a PIN-photodiode. Their subtracted photo current was measured at the spectrum analyzer, providing directly the variance of the *signal*. The auxiliary $\mathrm{PD}_{\mathrm{BS}_1}$ and $\mathrm{PD}_{\mathrm{BS}_2}$ are used to balance both beam splitters to a splitting ratio of 50:50.

shifter PS_S placed in the lower arm generates a *signal* (phase modulation) at a frequency of f = 4.879 MHz to generate an artificial signal. To excite photons into these high frequency mode is much more difficult, as compared to using an EOM. A piezo-actuator has resonances up to hundreds of kHz and by which one cannot expect to let it carry out excessive movements at higher frequencies. Furthermore,

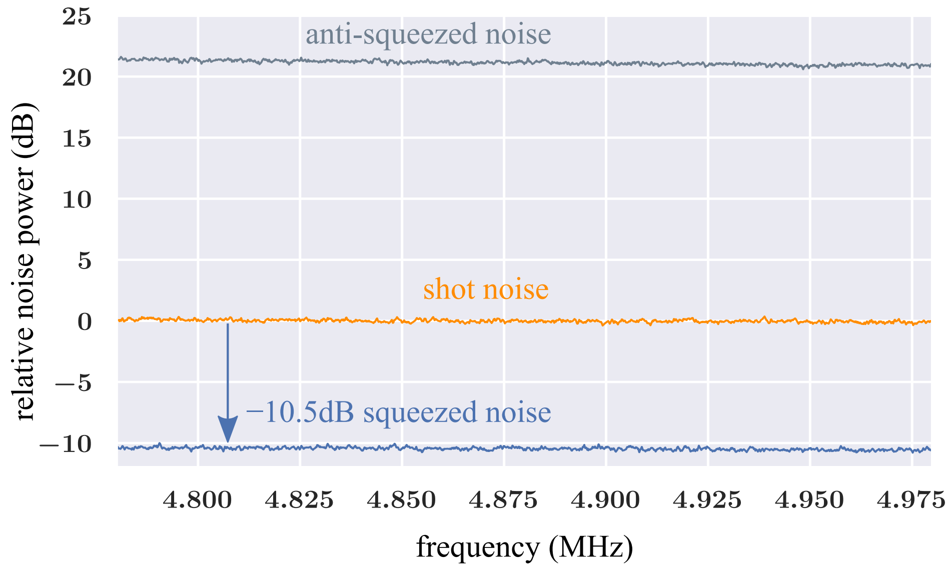

Figure 4.5.: 10 dB - squeezed light enhanced MZI. Shown are the noise power spectra measured at the interferometer output with balanced detection. The traces correspond to the spectra of quadrature amplitude normalized to the shot noise level using 10 mW input power. The shot noise (orange trace) is normalized to unity and serves as the reference level (0 dB). The measured variances correspond to the amplitude quadrature with squeezed variance (blue trace) of $\Delta^2 X_{\mathrm{SQZ}}$ = -10.5 dB and anti-squeezing (grey trace) of $\Delta^2 X_{\mathrm{ASQZ}}$ = 21.1 dB, respectively. The slight slope of all traces are due to the decreasing transfer function of the homodyne detector. All traces were recorded with a resolution bandwidth of $\Delta\Omega/2\pi$ = 5 kHz, a video bandwidth of 100 Hz, and were averaged seventy-five times.

a piezo-actuator's electrical behavior can be described as a capacitive load, whose power consumption is proportional to the applied frequency. Therefore a trade-off between a sufficiently strong signal and the applied voltage to the piezo-actuator was necessary.

The fringe visibility of the interferometer was measured to $\mathcal{C}_{\mathrm{min}} = 0.992 \pm 0.001$. To reach such high values, one arm was blocked, while the mode in the other arm was guided to a diagnostic mode cleaner via a flipping mirror placed at one output and matched to it and vice versa. The auxiliary photodiodes $\mathrm{PD}_{\mathrm{BS}_1}$ and $\mathrm{PD}_{\mathrm{BS}_2}$ are used to balance both beam splitters to a splitting ratio of 50:50. That is necessary to get the strongest correlation between the arms of the interferometer and to cancel out the quantum noise. Otherwise, an unbalancing introduces decoherence, which reduces the strength of entanglement and therefore the sensitivity improvement. Figure 4.5 shows the non-classical noise reduction with squeezed light in the frequency range from 4.78 MHz to 4.98 MHz without a *signal* generated in the interferometer. The spectrum presented here is the variance of the amplitude quadrature measured with balanced detection at the interferometers outputs as shown in figure 4.4. The obtained anti-squeezed variance is $\Delta^2 X_{\mathrm{ASQZ}}$ = 21.1 dB and the squeezed variance is $\Delta^2 X_{\mathrm{SQZ}}$ = -10.5 dB. From three such individual measurements the total average detection efficiency is calculated to be $\eta = 0.922 \pm 0.002$. After applying a sinusoidal voltage to $\mathrm{PS_S}$ with a frequency of f = 4.879 MHz some photons in the lower arm were excited and the light field carried a pure phase modulation at this frequency. This modulation is converted into a pure amplitude modulation (with the same frequency) at the second beam splitter $\mathrm{BS_2}$. Therefore the spectrum analyzer measures the amplitude quadrature at the interferometers output, in which the *signal* appears. Figure 4.6 shows the performance of the quantum enhanced MZI. This is demonstrated using different modulation strengths, resulting from changing the peak-to-peak voltage applied to $\mathrm{PS_S}$ to 50 mV, 100 mV, 200 mV, and 400 mV, respectively. The directly observed non-classical sensitivity improvement in all panels is about (10.5 $\pm$ 0.1) dB. The improvement of the signal-to-noise ratio is equivalent of a 11.2-fold increase in coherent light power, which is a factor of $\sqrt{11.2} = 3.35$. The result of a strong phase modulation shows the panel (a) in figure 4.6. The signal is visible in both cases; the shot noise limited interferometer (orange trace) as well as with squeezed light injection (blue trace).

Because the spectrum analyzer measures the sum of the noise and signal variance, the noise contribution of the squeezed state to the total variance is much less then of shot noise. Therefore the signal height is also lower. By decreasing the strength of the phase modulation (panels (b) - (d)), the signal decreases as well. In panel (d) the advantage of squeezed light injection is clearly demonstrated. For the shot noise limited interferometer (orange trace) no modulation signal is visible at an excitation voltage of 50 mV.

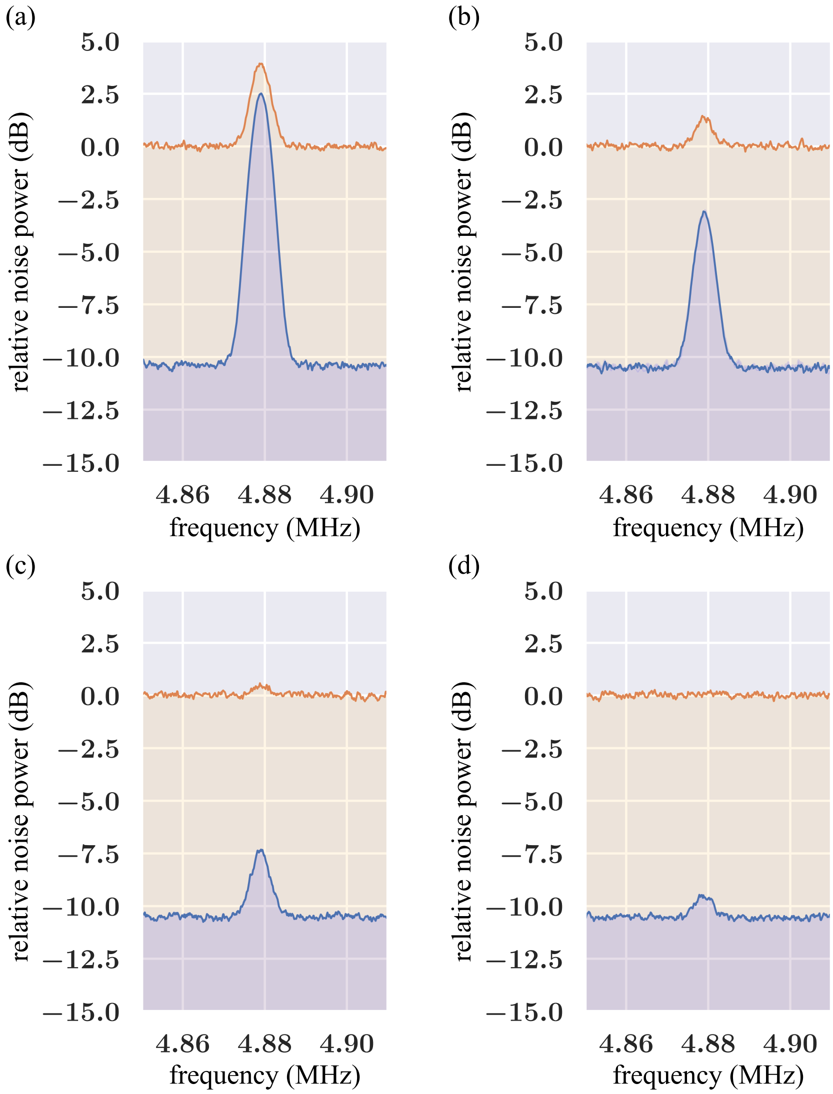

Figure 4.6.: Performance of the quantum enhance MZI. The orange traces show the measured variance spectrum of the signal modulation at a Fourier frequency of f = 4.879 MHz without squeezed light input. With squeezed light, the blue traces show a noise reduction by about 10.5 dB compared to vacuum noise, revealing an improved signal-to-noise ratio by a factor of $\sqrt{11.2} = 3.35$. The phase sensitivity improves by the equivalent of a 11.2-fold increase in coherent light power. The panels (a) to (d) shows an applied peak-to-peak voltage to the piezo-actuator of 400 mV, 200 mV, 100 mV, 50 mV respectively. All traces were recorded with a resolution bandwidth of 5 kHz, a video bandwidth of 100 Hz, and averaged seventy-five times. The dark noise clearance was about 23 dB below the shot noise.

If we use instead quantum correlations, e.g. squeezed states of light, a signal is clearly visible in the spectrum. For the same light power the signal-to-noise ratio is significantly improved. In conclusion, I have demonstrated experimentally, that it is feasible to achieve strong non-classical correlations in a Mach-Zehnder interferometer at wavelengths of 1550 nm to eliminate quantum shot noise. I showed that the squeezed light enhanced interferometer is superior to the conventional operation with coherent light only. Thereby, I achieved a (10.5 ± 0.1) dB reduction of shot noise of an artificial signal at a Fourier frequency of 4.879 MHz. As the equation 4.9 shows, the shot noise contributes with the inverse of the optical power. Accordingly, injecting strong squeezed light is the only possibility to reach a higher sensitivity of the interferometer without increasing the light power.

5. Low-intensity absorption measurement based on quantum correlated light

Optical absorption measurements are an important tool for characterization of the properties of optical materials. In practice, the light power for certain applications is limited. In particular it is highly relevant in biological systems, where biological samples are often highly photosensitive [66]. Here, optical damage is a limiting factor and it is necessary to either reduce the photon flux or reduce the exposure time (or both at the same time). An example are living cells, which are observed with light that could damage or even cause cell death. By illuminating light-sensitive probes with bright light, optical damage can be caused by *optical heating* and *photochemical effects*. It is possible to overcome these constraints by employing quantum correlated states, such as entangled photons, to enhance the precision with less exposure [67–69].

Optical absorption measurements are usually performed by direct measurement of sample's transmission. In this case photodiodes need to be calibrated. For that, several properties of the photodetectors have to be taken into account: linearity, stability, spectral responsivity and detection efficiency.

In this chapter I present a novel approach for low-intensity absorption measurements in a Mach-Zehnder interferometer. While overcoming the influence of the photodiodes' efficiency and the need for absolute calibration in absorption measurements, this new method may also be a powerful tool for measuring light-sensitive samples. It is based on the theoretical consideration by Mikhail Korobko, which is here experimentally realized in a proof-of-principle experiment. We adapted the setup presented already in the previous chapter 4.

5.1. Absorption measurement using single party squeezed light

The simplest approach to detect absorption (loss) of an unknown sample is illustrated in figure 5.1. In general this is a relative measurement, i.e. a two-step measurement: One with and one without the sample, to determine the relative absorption. The absorptive material is represented by the beam splitter $\mathrm{BS}_{\mathcal{A}}$, which is illuminated by the incident light $\hat{a}_1$. The transmitted light $\hat{b}_1$ passing the sample is measured with a photodiode PD_{A}, which converts the intensity into photocurrent and is subsequently analyzed to determine the absorption $\mathcal{A}$. In a realistic detection scheme, any measurement is corrupted by various sources of loss due imperfections of the setup.

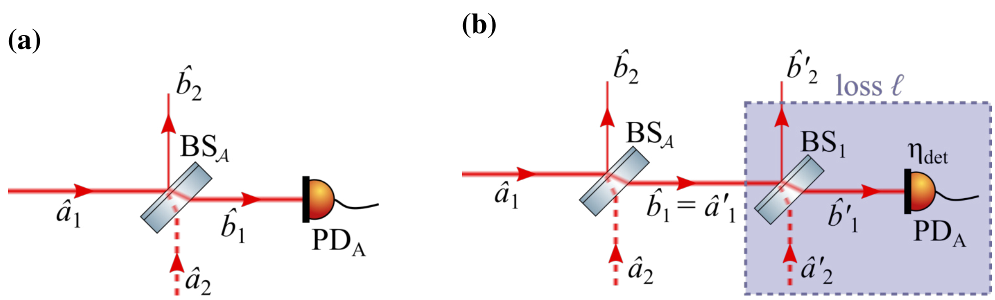

Figure 5.1.: Detection scheme of direct absorption measurement (a) shows an ideal absorption measurement $\mathcal{A}$ of the light field $\hat{b}_1$. The transmitted light is passing the sample, which is represented by $\mathrm{BS}_{\mathcal{A}}$. The only loss is due to the sample's absorption, which is measured by detecting light with the photodiode PD_{A}. In (b) the detection process is not perfect, because of the imperfect detection efficiency $\eta_{\mathrm{det}} < 1$ of the photodiode itself. This can be seen as an additional loss to the measured field $\hat{b}'_1$ visualized by the virtual beam splitter BS_1. Usually, drifts emerge in the setup due to laser power fluctuation or optomechanical instabilities when the sample is measured; Hence, the absorption $\mathcal{A}$ can only be evaluated if the detection efficiency of all photodiodes is precisely known. Thus each photodiode needs to be calibrated.

In the case of figure 5.1 (b) additional loss ℓ is introduced by the quantum efficiency $\eta_{\mathrm{det}} < 1$ of the photodiode. To estimate the absolute absorption $\mathcal{A}$ of a sample as precise as possible, however, it is necessary to know the quantum efficiency beforehand and to calibrate all measurements that is required for comparison in sensing and monitoring. In principle the precise calibration of the photodiodes efficiency could be realized based on continuous-wave squeezed light. To describe a direct measurement of the quadrature field $\hat{b}'_1$ including a detection efficiency η_{det} we consider the transfer matrix

$$\begin{pmatrix} \hat{b}'_1 \\ \hat{b}'_2 \end{pmatrix} = \begin{pmatrix} \sqrt{\eta_{\mathrm{det}}} & \sqrt{1-\eta_{\mathrm{det}}} \\ -\sqrt{1-\eta_{\mathrm{det}}} & \sqrt{\eta_{\mathrm{det}}} \end{pmatrix} \begin{pmatrix} \hat{a}'_1 \\ \hat{a}'_2 \end{pmatrix}, \tag{5.1}$$

where $\eta_{\mathrm{det}} = 1 - \ell$ with a certain power reflectivity ℓ, equivalent to some loss coupling in vacuum fluctuations through the beam splitter BS_1 as pictured in the grey box of figure 5.1(b). The two input quadrature fields $\hat{a}'_1$ and $\hat{a}'_2$ are converted into the output quadrature states $\hat{b}'_1$ and $\hat{b}'_2$. As we are interested in the absorption of the sample, we measure the transmission of the resulting field $\hat{b}'_1$ and get a superposition according to the transfer matrix

$$\hat{b}'_1 = \sqrt{\eta_{\mathrm{det}}}\,\hat{a}'_1 + \sqrt{1-\eta_{\mathrm{det}}}\,\hat{a}'_2. \tag{5.2}$$

Detecting this field, we get the photodiodes intensity related to a power noise spectrum $S_{b'b'} = \langle \hat{b}'\hat{b}'^{\dagger} \rangle$

$$\begin{aligned} S_{b'b'} &= \langle (\sqrt{\eta_{\mathrm{det}}}\,\hat{a}'_1 + \sqrt{1-\eta_{\mathrm{det}}}\,\hat{a}'_2)(\sqrt{\eta_{\mathrm{det}}}\,\hat{a}'^{\dagger}_1 + \sqrt{1-\eta_{\mathrm{det}}}\,\hat{a}'^{\dagger}_2) \rangle \\ &= \langle \eta_{\mathrm{det}}\hat{a}'_1\hat{a}'^{\dagger}_1 + \sqrt{\eta_{\mathrm{det}}(1-\eta_{\mathrm{det}})}(\hat{a}'_1\hat{a}'^{\dagger}_2 + \hat{a}'_2\hat{a}'^{\dagger}_1) + (1-\eta_{\mathrm{det}})\hat{a}'_2\hat{a}'^{\dagger}_2 \rangle \,. \end{aligned} \tag{5.3}$$

Assuming $\hat{a}'_1$ is a squeezed state with $\langle \hat{a}'_1\hat{a}'^{\dagger}_1 \rangle = e^{-2r}$ and $\hat{a}'_2$ is in its ground state with $\langle \hat{a}'_2\hat{a}'^{\dagger}_2 \rangle = 1$, the mixing terms are averaging to zero $\langle \hat{a}'_1\hat{a}'^{\dagger}_2 \rangle = \langle \hat{a}'_2\hat{a}'^{\dagger}_1 \rangle = 0$ and the measured spectrum is given by

$$S_{b'b'} = \eta_{\mathrm{det}} e^{-2r} + (1-\eta_{\mathrm{det}}). \tag{5.4}$$

Equation 5.4 shows that using the quantum correlation of a single squeezed state of light is valuable to characterize the detection efficiency η_{det}. The effect of loss is equal to additional contribution of vacuum field to the squeezed quadrature. Thus, by decreasing the detection efficiency (increasing loss) for a given squeeze parameter r, the spectrum gets closer to the shot noise level. Therefore it can be used for absolute calibration of the quantum efficiencies of photodiodes where a calibrated standard for the incident light power is not necessary [22]. Here the used technique required the measurements of the squeeze and the corresponding anti-squeeze levels. Additionally, the precise determination of all the losses induced by imperfect optical components is required beforehand. This includes the optical loss from dielectric coatings, the OPA escape efficiency and also the homodyne visibility. Those values have to be known very precisely, which is not always practical when precise measurements are required on demand. To avoid the need for absolute calibration we suggest in the following section a novel approach with bipartite squeezed light.

5.2. Absorption measurement with bipartite squeezed light

The basic idea of the bipartite squeezed light absorption measurement is to measure one part of a squeezed state relative to another where the loss occurs. In a setup that satisfies the condition of the self-referenced measurement of squeezing no calibration of the photodiode is necessary. We consider a Mach-Zehnder interferometer as depicted in figure 5.2 with one squeezed vacuum state entering one input port and an absorber $\mathcal{A}$ in one arm, introducing some loss. It will be useful for the analysis to restrict the formulation to the specific case of interest. Therefore we will omit unbalancing of the beam splitter and loss in the arms from imperfections of optical parts or misalignment that basically reduces the contrast of the interferometer.

5.2.1. Theoretical consideration

From the action of different parts in the interferometer, we get a set of linear equations separated into the phase and amplitude quadrature, respectively. We denote the respective superscripts of the states with p for phase or a for amplitude. For the corresponding fields inside the MZI we find for the phase and amplitude quadrature operators:

$$
\begin{aligned}
\hat{c}_1^p &= \frac{1}{\sqrt{2}}(\hat{a}_2^p - \hat{a}_1^p) & \hat{c}_1^a &= \frac{1}{\sqrt{2}}(\hat{a}_2^a - \hat{a}_1^a) \\
\hat{c}_2^p &= \hat{c}_1^p \cos(\phi) - \hat{c}_1^a \sin(\phi) & \hat{c}_2^a &= \hat{c}_1^p \sin(\phi) + \hat{c}_1^a \cos(\phi) \\
\hat{c}_3^p &= \frac{1}{\sqrt{2}}(\hat{a}_2^p + \hat{a}_1^p) & \hat{c}_3^a &= \frac{1}{\sqrt{2}}(\hat{a}_2^a + \hat{a}_1^a) \\
\hat{c}_4^p &= \sqrt{\eta_s}\,\hat{c}_3^p + \sqrt{1-\eta_s}\,\hat{v}_s & \hat{c}_4^a &= \sqrt{\eta_s}\,\hat{c}_3^a + \sqrt{1-\eta_s}\,\hat{v}_s\,,
\end{aligned}
$$

where ϕ is the relative phase between the two arms, η_s corresponds to the absorption of the sample and $\hat{v}_s$ is related to the in coupled vacuum due to the loss. For the output fields of the MZI we find

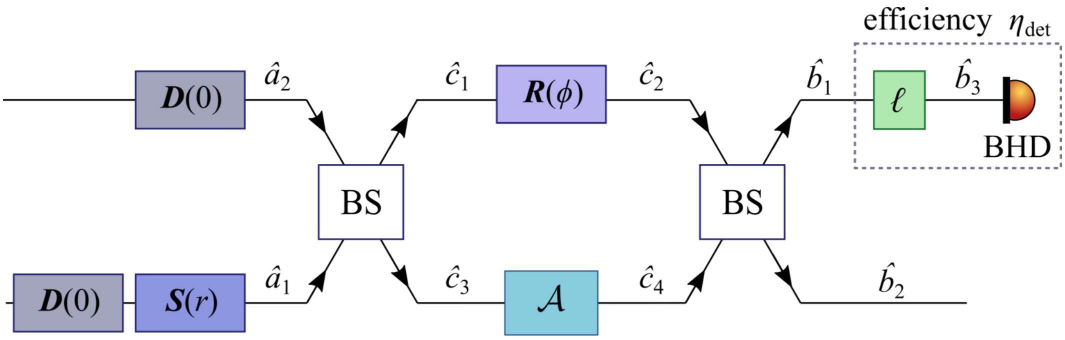

Figure 5.2.: Concept of absorption measurements with bipartite squeezed light. The demonstration uses a Mach-Zehnder interferometer configuration to measure the absorption $\mathcal{A}$ in one arm relative to the other arm. To measure the superposition at the second beam splitter (BS), one output is used to detect the outgoing field with a balanced homodyne detector (BHD). Additionally, an extra channel with loss ℓ is introduced that represent the imperfect photodiodes detection efficiency η_{det}. The block diagram visualizes the denominations used in the derivation of the measured photodiodes intensities. $\boldsymbol{S}(r)$: squeezing; $\boldsymbol{D}(0)$: vacuum; $\boldsymbol{R}(\phi)$: rotation; BS: beam splitter.

$$\hat{b}_1^p = \frac{1}{2}(\hat{c}_2^p + \hat{c}_4^p) = \frac{1}{2}\left[(\hat{c}_1^p \cos(\phi) - \hat{c}_1^a \sin(\phi)) + (\sqrt{\eta_s}\,\hat{c}_3^p + \sqrt{1-\eta_s}\,\hat{v}_s)\right], \quad (5.5)$$

$$\hat{b}_1^a = \frac{1}{2}(\hat{c}_2^a + \hat{c}_4^a) = \frac{1}{2}\left[(\hat{c}_1^p \sin(\phi) + \hat{c}_1^a \cos(\phi)) + (\sqrt{\eta_s}\,\hat{c}_3^a + \sqrt{1-\eta_s}\,\hat{v}_s)\right]. \quad (5.6)$$

Now introducing additional loss ℓ at the output, we obtain the field $\hat{b}_3$. Inserting the operators $\hat{c}_1^p$, $\hat{c}_1^a$, $\hat{c}_3^p$ and $\hat{c}_3^a$ we get

$$\begin{aligned}
\hat{b}_3^p &= \sqrt{\eta_{\mathrm{det}}}\,\hat{b}_2^p + \sqrt{1-\eta_{\mathrm{det}}}\,\hat{v}_1 \\
&= \frac{\sqrt{\eta_{\mathrm{det}}}}{\sqrt{2}}\left[\cos(\phi)\left(\frac{1}{\sqrt{2}}(\hat{a}_2^p - \hat{a}_1^p)\right) + \sin(\phi)\left(\frac{1}{\sqrt{2}}(\hat{a}_2^a - \hat{a}_1^a)\right)\right. \\
&\qquad\qquad \left. + \frac{\eta_s}{2}(\hat{a}_2^p + \hat{a}_1^p) + \sqrt{1-\eta_s}\,\hat{v}_s\right] + \sqrt{1-\eta_{\mathrm{det}}}\,\hat{v}_1 \\
&= \frac{\sqrt{\eta_{\mathrm{det}}}}{2}\Big[\hat{a}_2^p(\cos(\phi) + \sqrt{\eta_s}) - \hat{a}_1^p(\cos(\phi) - \sqrt{\eta_s}) \\
&\qquad\qquad - \hat{a}_2^a \sin(\phi) + \hat{a}_1^a \sin(\phi) + \sqrt{2(1-\eta_s)}\,\hat{v}_s\Big] + \sqrt{1-\eta_{\mathrm{det}}}\,\hat{v}_1\,,
\end{aligned} \quad (5.7)$$

and for the amplitude quadrature correspondingly:

$$\begin{aligned}
\hat{b}_3^a &= \sqrt{\eta_{\mathrm{det}}}\,\hat{b}_2^a + \sqrt{1-\eta_{\mathrm{det}}}\,\hat{v}_1 \\
&= \frac{\sqrt{\eta_{\mathrm{det}}}}{\sqrt{2}}\left[\sin(\phi)\left(\frac{1}{\sqrt{2}}(\hat{a}_2^p - \hat{a}_1^p)\right) + \cos(\phi)\left(\frac{1}{\sqrt{2}}(\hat{a}_2^a - \hat{a}_1^a)\right)\right. \\
&\qquad\qquad \left. + \frac{\eta_s}{2}(\hat{a}_2^a + \hat{a}_1^a) + \sqrt{1-\eta_s}\,\hat{v}_s\right] + \sqrt{1-\eta_{\mathrm{det}}}\,\hat{v}_1 \\
&= \frac{\sqrt{\eta_{\mathrm{det}}}}{2}\Big[\hat{a}_2^a(\cos(\phi) + \sqrt{\eta_s}) - \hat{a}_1^a(\cos(\phi) - \sqrt{\eta_s}) \\
&\qquad\qquad - \hat{a}_2^p \sin(\phi) + \hat{a}_1^p \sin(\phi) + \sqrt{2(1-\eta_s)}\,\hat{v}_s\Big] + \sqrt{1-\eta_{\mathrm{det}}}\,\hat{v}_1\,.
\end{aligned} \quad (5.8)$$

Again we assume that $\langle \hat{a}_2^p \hat{a}_2^{p\dagger} \rangle = \langle \hat{a}_2^a \hat{a}_2^{a\dagger} \rangle = \langle \hat{v}_1 \hat{v}_1^\dagger \rangle = \langle \hat{v}_s \hat{v}_s^\dagger \rangle = 1$. Furthermore the phase quadrature is in a squeezed state $\langle \hat{a}_1^p \hat{a}_1^{p\dagger} \rangle = e^{-2r}$ and the amplitude quadrature is in a anti-squeezed state $\langle \hat{a}_1^a \hat{a}_1^{a\dagger} \rangle = e^{2r}$. Thus the measured spectra $S_{bb} = \langle \hat{b} \hat{b}^\dagger \rangle$ of the respective quadrature field are:

$$S_{bb}^p = \frac{1}{4} e^{-2r} \Big[\eta_{\text{det}} (\sqrt{\eta_s} - \cos(\phi))^2 - e^{2r} (-4 + \eta_{\text{det}} + \eta_{\text{det}} \eta_s - 2\sqrt{\eta_s} \eta_{\text{det}} \cos(\phi)) \\ + e^{4r} \eta_{\text{det}} \sin^2(\phi) \Big] , \tag{5.9}$$

$$S_{bb}^a = \frac{1}{4} e^{-2r} \Big[e^{4r} \eta_{\text{det}} (\sqrt{\eta_s} - \cos(\phi))^2 - e^{2r} (-4 + \eta_{\text{det}} + \eta_{\text{det}} \eta_s - 2\sqrt{\eta_s} \eta_{\text{det}} \cos(\phi)) \\ + \eta_{\text{det}} \sin^2(\phi) \Big] . \tag{5.10}$$

The spectra depend on the detection efficiency η_{det}, η_s, the squeeze parameter r and the relative phase ϕ between the two arms of the Mach-Zehnder interferometer. The top of figure 5.3 shows the relative position of the bipartite squeezed states at the second beam splitter. The interference of the correlated squeezed vacuum states at different phase angles ϕ results in the noise spectra of amplitude and phase quadrature as plotted from equation 5.9 and 5.10 without losses and considering a perfect detection efficiency. The correlation between the squeezed states is indicated by the crosses. If the length of both arms are equal ($\phi = 0$) the measured (anti-) squeezing is maximal. Changing the length of one arm reduces the (anti-) squeeze factor. At phase $\phi = \pi/2$ the contribution of the rotated squeezed state, such that in both spectra anti-squeezing occurs. The correlation at a phase $\phi = \pi$ results in a partially squeezed vacuum state in both quadratures. Since the detection is based on the measurement of one squeezed vacuum state relative to another, the correlation can be exploited to estimate the absorption $\mathcal{A}$ that appears in one arm of the interferometer.

From these spectra of the phase and quadrature we can derive a function which is independent of the detection efficiency η_{det}. Therefore we have to calculate first the difference between the spectrum at phase ϕ and a shifted phase $\phi + \zeta$, thus:

$$S_{\text{diff}}(\phi) = S_{bb}(\phi) - S_{bb}(\phi + \zeta) . \tag{5.11}$$

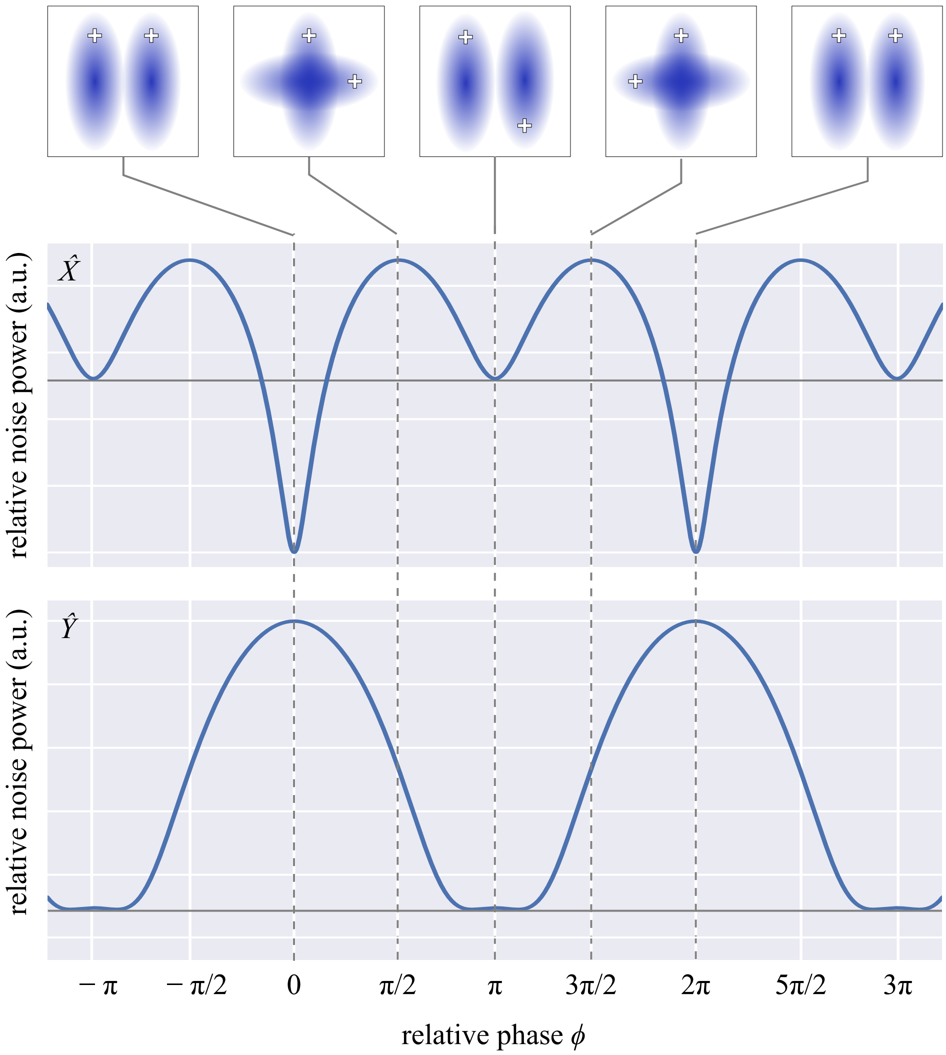

Figure 5.3.: Spectra of phase and amplitude quadrature. From top to bottom: The upper figure shows the correlation of the bipartite (phase) squeezed vacuum states at several instances of the relative phase ϕ between the two arms of the Mach-Zehnder interferometer. The correlation is indicated by the crosses. The resulting interference at the second beam splitter depends on the orientation of squeezed states to each other while scanning the phase. For comparison the solid black line represents the reference (vacuum noise). The middle plot shows the noise spectrum of the amplitude quadrature calculated with equation 5.9. The lower plot shows the noise spectrum of the phase quadrature calculated from equation 5.10. For both plots I considered no loss and a perfect detection efficiency.

Choosing $\zeta = \pi/2$ for both, the squeezed and the anti-squeezed spectrum, we obtain the following spectra:

$$S^{p}_{\text{diff}}(\phi) = -\,\eta_{\text{det}}\frac{1}{4}e^{-2r}(e^{2r}-1)\Big[(1+e^{2r})\cos(2\phi) - 2\sqrt{\eta_s}(\cos(\phi)+\sin(\phi))\Big]\,, \tag{5.12}$$

$$\begin{aligned} S^{a}_{\text{diff}}(\phi) = -\,\eta_{\text{det}}(\cos(\phi)+\sin(\phi))\sinh(r)\Big[&\cosh(r)(\sqrt{\eta_s}-\cos(\phi))+\sin(\phi) \\ &+\sqrt{\eta_s}\sinh(r)\Big]\,. \end{aligned} \tag{5.13}$$

Both spectra have the photodiodes inefficiency η_{det} as a common factor, which could be eliminated by taking the ratio $S^{\text{ratio}}_{\zeta_a,\zeta_p}$ with the shifted phases $\zeta_a = \zeta_p = \pi/2$:

$$S^{\text{ratio}}_{\pi/2,\pi/2} = \frac{S^{p}_{\text{diff}}(\phi)}{S^{a}_{\text{diff}}(\phi)} = \frac{N}{D} - 1\,, \tag{5.14}$$

with

$$\begin{aligned} N &= 2(e^{2r}-1)\sqrt{\eta_s}\,, \\ D &= e^{2r}(2\sqrt{\eta_s}-\cos(\phi)+\sin(\phi))+\sin(\phi)-\cos(\phi)\,, \end{aligned}$$

which is still dependent on the squeeze parameter r and the absorption of interest included in η_s, but not on the photodiodes detection efficiency η_{det}. In this approach we compare the interference of the two squeezed states at the second balanced beam splitter before reaching the homodyne detector. All the loss that happens afterwards, e.g. the quantum efficiency of the photodiodes at the homodyne detector is common to the result of the interference and can be factored out. To demonstrate the detection efficiency's independence in this new method, we applied additional loss before the measurement device. As a result, this artificially reduced the detection efficiency of the detector, which is confirmed in the following.

5.2.2. Experimental demonstration

The schematics of our experiment is presented in figure 5.4. The interferometer was operated with continuous-wave laser beam at a wavelength of 1550 nm. The balanced beam splitter BS_1 (50:50) splits the (phase) squeezed vacuum state into two partial squeezed states. One part serve as reference, while the other part probe the loss of 1% appearing at the 99:1 beam splitter BS_A. This will be denoted in the following as the 'signal' arm of the interferometer. It represents the material to be studied, e.g. a photosensitive biological sample. To extract the loss value, the superposition of both partial beams at different phases ϕ were measured at one output of BS_2 with balanced homodyne detection. To change the relative phase continuously we used a phaseshifter (PS_ϕ) and applied a ramp with a frequency of $f = 700$ mHz. Because of that we could not use directly the fixed phase relation of the SSB and the squeezed quadrature to lock the homodyne angle. This is different to the chapters 4 and 6 and it was necessary to implement an additional phase lock between an auxiliary local oscillator field and the SSB, which was independent of the Mach-Zehnder phase ϕ. We used the 1% transmission of the beam splitter BS_A and superimposed it with an auxiliary field of about 1 mW light power. The detected light at the photodiode PD_{82} was demodulated at a frequency of 82 MHz, and the sinusoidal error signal was fed back to the piezo-actuated mirror phase shifter (PS_{aux}) in the path of the auxiliary field. A phase lock between the SSB and the auxiliary field was established. Since the phase of the SSB (and thereby to the squeeze angle) has a fixed phase relation to the squeezed field, this lock immediately established a fixed phase relation between the auxiliary field and the squeezed quadrature. The electro-optical modulator (EOM) generated sidebands at a frequency of 78 MHz in the same path, but before PS_{aux}. The 1% transmission of sidebands were sent to the homodyne detector and the signal was demodulated at 78 MHz to get an error signal for the squeezed light phase look as depicted in figure 5.4. Thus the implemented locking scheme allowed us to stably control the relative phase between the local oscillator LO of the homodyne detector either at zero (amplitude quadrature) or ninety degrees (phase quadrature). Furthermore it allowed us to lock the quadrature independent of the relative phase ϕ between the two arms of the Mach-Zehnder interferometer.

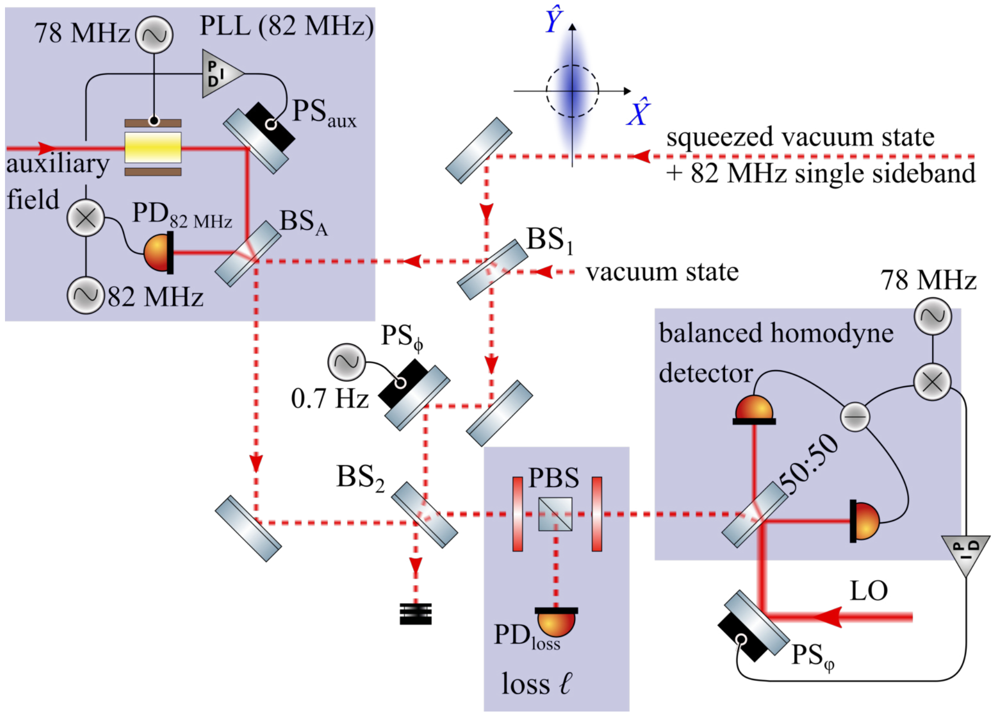

Figure 5.4.: Schematics of the experimental setup. Shown are the optical paths of laser light. The balanced beam splitter BS_1 (50:50) splits the (phase) squeezed vacuum state into two partial squeezed states. The transmitted part serves as a reference, while the reflected part probe the loss of 1% from the 99:1 beam splitter BS_A. To extract the loss value, the superposition of both partial beams at different phases ϕ are measured at one output of BS_2 with balanced homodyne detection. The relative phase was continuously changed with phaseshifter (PS_ϕ) by applying a frequency of $f = 700\,\text{mHz}$. An auxiliary field of 1 mW was overlapped at the BS_A with the single sideband at a frequency of 82 MHz. The generated error signal was fed back to PS_{aux}, creating a fixed phase relation to the squeezed vacuum state. The electro-optical modulator (EOM) generates sidebands at a frequency of 78 MHz in the same path. The 1% transmission of sidebands overlapped at the homodyne detectors 50:50 beam splitter with the local oscillator (LO) for stable locking the BHD to squeezed or anti-squeezed vacuum for all phases $\phi \in [0, 2\pi]$. A combination of a half-wave plates and a polarization beam splitter (PBS) introduces additional loss ℓ, to demonstrate that the absorption is independent on the detection efficiency η_{det} of the BHD.

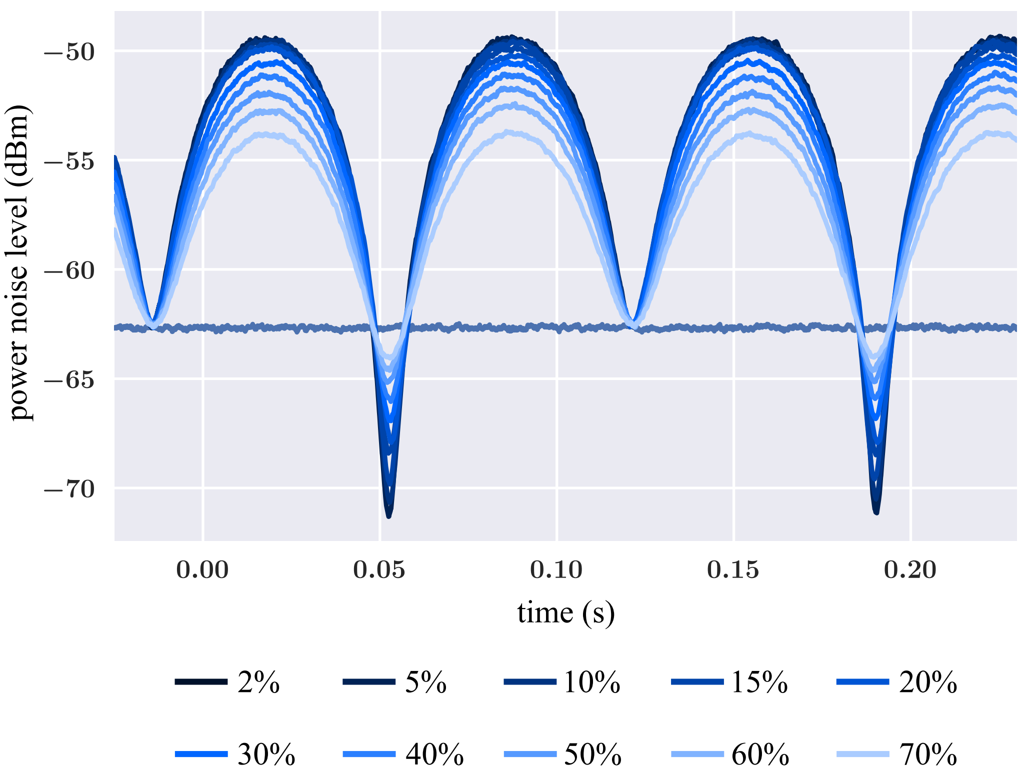

Figure 5.5.: Measured phase quadrature of the (phase) squeezed vacuum state with balanced homodyne detection. The measurement shows the noise power spectrum at a Fourier frequency of $\Omega/2\pi = 5\,\text{MHz}$ measured at one output port of the MZI. Ten different loss values $\ell = (2\,\%, 5\,\%, 10\,\%, 15\,\%, 20\,\%, 30\,\%, 40\,\%, 50\,\%, 60\,\%, 70\,\%)$ were used. For each loss value the phase ϕ of the MZI was periodically scanned. Depending on certain phases, the squeezed vacuum rotates in phase space relative to the other and interfere such that the noise is above the shot noise level, resulting in anti-squeezed state. The constant line at -62.5 dBm corresponds to the shot noise level. All traces were recorded with a resolution bandwidth of $\Delta\Omega/2\pi = 300\,\text{kHz}$, a video bandwidth of 300 Hz and were averaged twenty times.

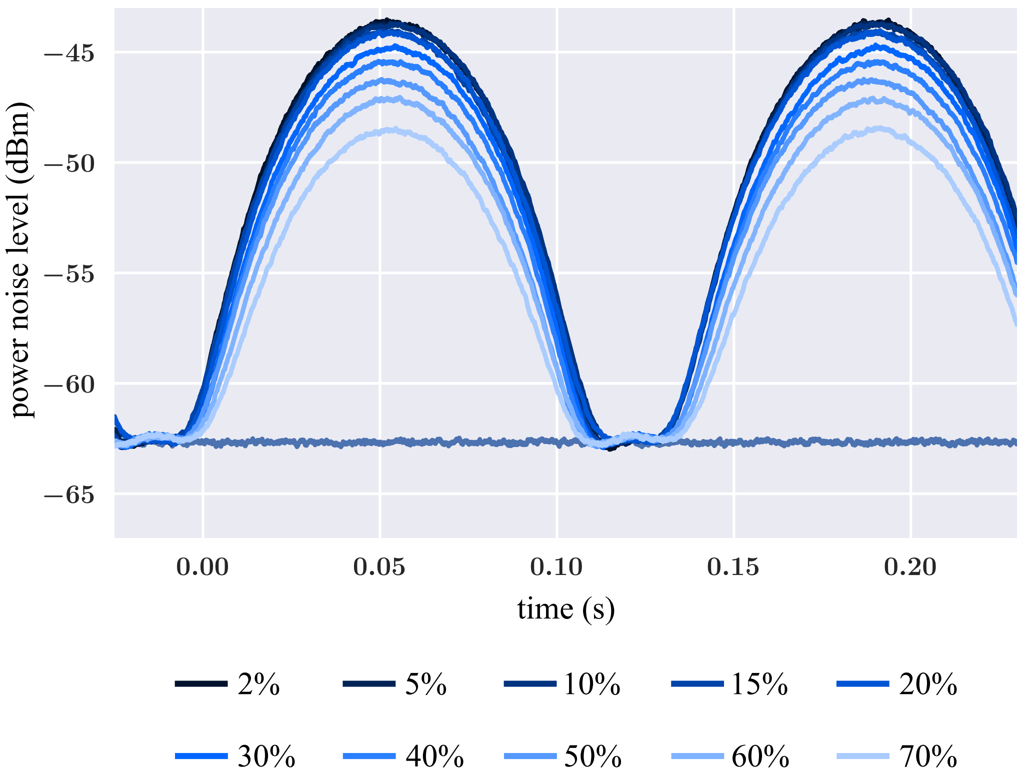

Figure 5.6.: Measured amplitude quadrature of the (phase) squeezed vacuum state with balanced homodyne detection. The measurement shows the noise power at a Fourier frequency of $\Omega/2\pi = 5\,\text{MHz}$ measured at one output port of the MZI. Ten different loss values $\ell = (2\,\%, 5\,\%, 10\,\%, 15\,\%, 20\,\%, 30\,\%, 40\,\%, 50\,\%, 60\,\%, 70\,\%)$ were used. The constant line at -62.5 dBm corresponds to the shot noise level. For each loss value the phase ϕ of the MZI was periodically scanned. Depending on the relative phase, the minimum noise power does not fall below the shot noise level. All traces were recorded with a resolution bandwidth of $\Delta\Omega/2\pi = 300\,\text{kHz}$, a video bandwidth of 300 Hz and were averaged twenty times.

Independence on detection efficiency

To demonstrate the advantage of our approach, we placed a combination of half-wave plates ($\lambda/2$) and a polarization beam splitter (PBS) in front of the balanced homodyne detector to introduced additional loss ℓ between 2% and 70%. The loss value was measured by detecting light with the photodiode PD_{loss}. For each loss value, we measured the spectrum of the amplitude (or phase) quadrature with a spectral analyzer while scanning the phase ϕ. The result is shown in figure 5.5 and figure 5.6, respectively, and are consistent with the calculated spectrum of equation 5.9 and 5.10. The figure 5.5 shows the obtained spectra of the phase quadrature measurement. Although the homodyne detector measures the squeezed noise variance, at certain phases the noise goes above vacuum noise level ('shot noise'). This is due to the relative rotation of the squeezed vacuum in phase space in the reference arm with respect to the 'signal' arm. At phases $\phi = \pi/2$ and $\phi = 3\pi/4$ the interfering states at the beam splitter result in an outgoing state that exceeds the shot noise level. Its maximum value of approximately -44 dBm results in an anti-squeezed state.

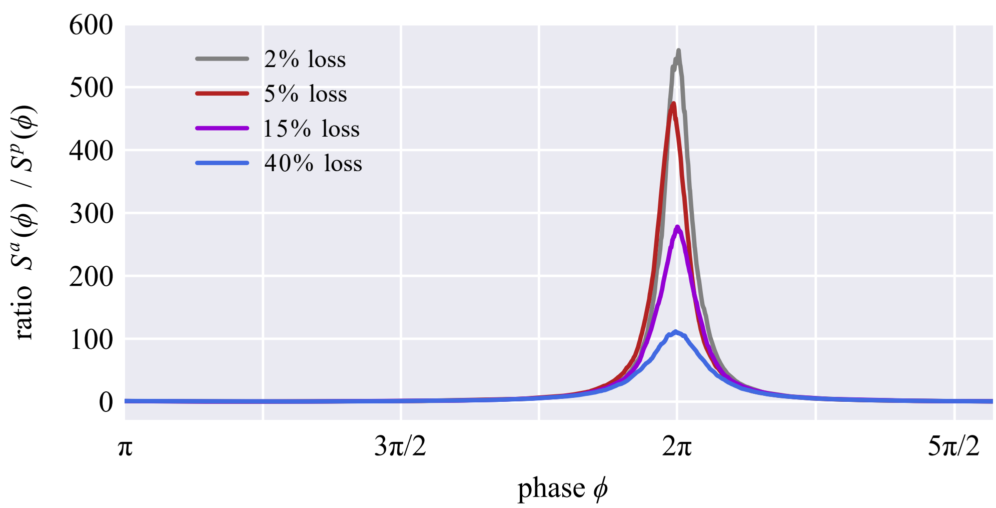

Figure 5.7.: Detection dependence on the photodiodes quantum efficiency in usual absorption measurements schemes. The figure displays the ratio $S^{\text{ratio}} = S^a/S^p$ comparable to a single party squeeze measurement without taking advantage of the phase ϕ as an additional degree of freedom. The plotted curves correspond to four different measured detection loss values ℓ = (2 %, 5 %, 15 %, 40 %). Therefore the measurement device shows a significant dependence on the induced loss, resulting in different peak heights of the ratio.

Similarly we measured the amplitude quadrature for the same loss values. The resulting output spectra shows the figure 5.6 and, as expected, the traces varied between the maximum anti-squeezed noise level and the shot noise level. For all loss values the difference between the squeezed noise power spectra at 5 MHz of S^p_{diff} and the anti-squeezed spectra S^a_{diff} are calculated in accordance to equation 5.12 and 5.13. To illustrate the benefit of our measurement scheme, I first plot the ratio $S^{\text{ratio}} = S^a / S^p$ of the squeezed and anti-squeezed quadrature in the figure 5.7. This can be interpreted as the equivalent experimental setup of the absorption measurement discussed in section 5.1 utilizing a conventional setup.

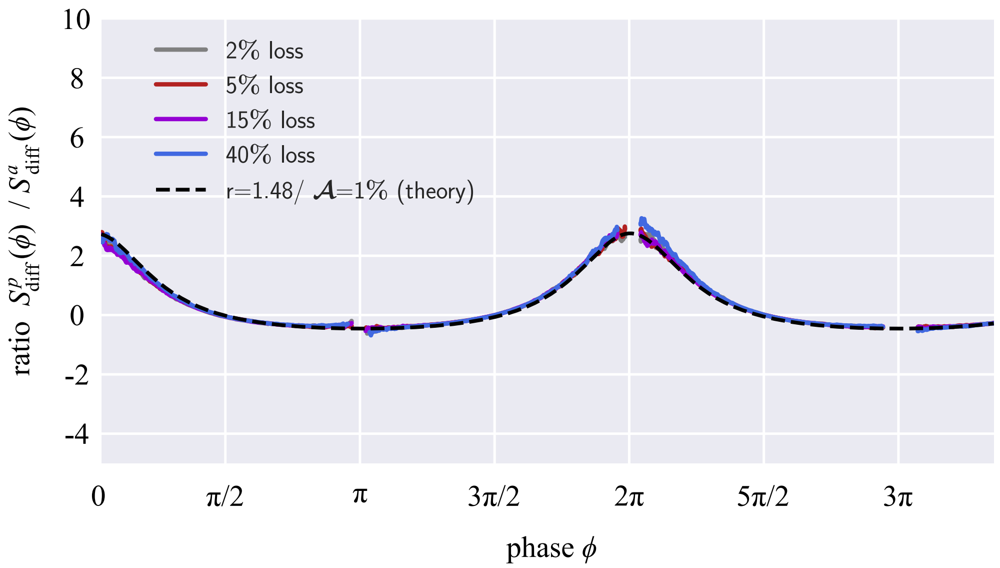

Figure 5.8.: Demonstration of the independence on the photodiodes quantum efficiency with bipartite squeezed light. The ratio $S^{\text{ratio}}_{\pi/2,\pi/2}$ calculated for the same four different measured detection loss values ℓ = (2 %, 5 %, 15 %, 40 %) as in figure 5.7 of the relative measurement for the squeezed light using equation 5.14. All traces coincidence over the plotting range and therefore entail the independence on detection loss, but depending solely on the light absorptive material. The data at phases $\phi = n\pi$ were removed, since the curves show at these points large noise due to experimental instabilities in the setup of the Mach-Zehnder phase. The absorption can be deduced from the traces. The theoretical prediction shows the dashed black curve for a initial squeeze parameter $r = 1.48$ and an absorption of $\mathcal{A} = 1\%$.

The plotted curves correspond to a detection loss $\ell = (2\%, 5\%, 15\%, 40\%)$ introduced at the PBS before the squeezed light reaches the balance homodyne detector. A significantly difference of the curves is visible at a phase $\phi = 2\pi$, which is the case of equal arm length of the MZI. This operation point complies with the full squeeze or anti-squeeze factor. The emulated detection efficiencies show different peak heights. With increasing detection loss the peak decreases, and vice versa. If we use our novel approach instead and take advantage of relative measurements, we can completely avoid the effect of detection efficiency. The result is presented in figure 5.8. Therefore the noise spectra of the ratio $S^{\text{ratio}}_{\pi/2,\pi/2}$ shows no dependence on the induced loss at the output port of the interferometer. All traces are overlapping over the full range and therefore entail the independence on the detection loss. At phases of $\phi = \pi$ and $\phi = 2\pi$ the curves are noisy. The data are excluded at those points to show the important feature. Additionally, the theoretical prediction for the 1 % absorption sample with an initial squeeze factor of $r = 1.48$ is plotted. Although the measurement are corrupted by large noise, the excepted theoretical plot is in good agreement with the experimental data.

5.3. Conclusion

In this proof-of-principle experiment we demonstrated that absolute photodiode calibration in direct absorption measurement can be fully avoided when using a relative measurement scheme with bipartite squeezed light. Our approach uses state of the art squeezed light sources that provided about 9 dB of squeezing, in combination with a Mach-Zehnder interferometer. We performed a sensing measurement on the transmission of a 99:1 beam splitter in the signal arm with 10 different loss values added at the output port (ranging from 2 % to 70 %) corresponding to different detection efficiencies, respectively. As no need for calibration is necessary, also misalignment in the setup (for example the visibility of homodyne detector) is in principle irrelevant as long as the Mach-Zehnder interferometer itself remains stable.

Therefore our approach has potential for quantum interferometric measurements of photosensitive samples in changing environments, where the alignment is prone to its detrimental effects, e.g. in bio sensing, with integrated quantum photonic devices

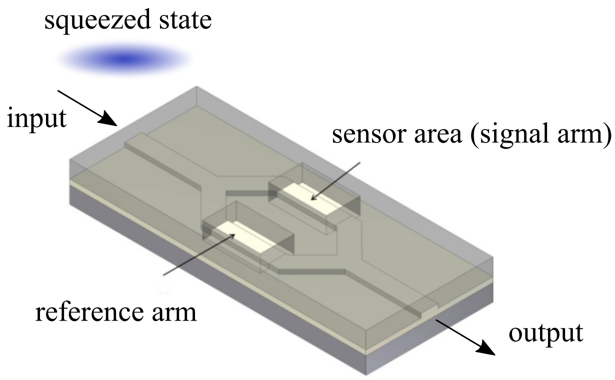

Figure 5.9.: On-Chip integrated Mach-Zehnder interferometer. The squeezed light is injected into the MZI and split into a signal arm with the sensor area and a reference arm. The light propagating through the two arms, interfere in a single output. Figure adapted from [70].

(see figure 5.9). Those are combining the stability of integrated optics for high visibility, low loss and interference of quantum correlation to reach high precision. Such devices can be fabricated cost-effectively and especially their compactness and the simple operation makes them attractive as reliable diagnostic sensors.

We demonstrated the proof-of-principle operation of the concept. Further research is needed to understand the influence of various imperfections in the setup (imbalance of the beam splitter, additional loss in the reference and signal arm), as well as finding the optimal reference combinations of spectra.

6. Surmounting Heisenberg's indeterminacy in sensing

It is widely accepted that Heisenberg's uncertainty relation sets a fundamental limit to the precision of measurements of fields, motions and forces. This often leads to the miss-interpretation that displacement measurement can not assign arbitrary precise information to a pair of canonical conjugate quantities simultaneously and even suggests that quantum trajectories always have quantum indeterminacy. As pointed out by Einstein, Podolsky and Rosen (EPR) [12], according to quantum theory, there are pairs of quantum systems whose properties with respect to each other can be determined arbitrarily precisely. A wide range of well-engineered quantum experiments took advantage of such EPR-entangled states, which allows for predictions of measurement results with a phase space uncertainty product smaller than that of the measured system's ground state. It is the resource for quantum teleportation [71–73] as well as for high-precision quantum measurements [74, 75].

None of the previous experiments targeted the question whether a system can be measured to have a time-dependent evolution in phase space (a 'trajectory') that is precisely 'determined' (in the sense of 'defined') with respect to another quantum system. In this chapter, I investigate whether this is possible in the case of two systems that are not coupled to the environment.

6.1. Quantum-enhanced sensing and monitoring

In general, quantum sensing pursue the purpose of measuring the properties of an quantum object. In the previous chapters 4 and 5 we were solely interested in a single quantity of our investigated System. Therefore we improved the sensitivity of our detector for the respective quantity. For many applications in metrology such an approach is sufficient [27, 76–78]. In contrast our intention will be in the following to obtain information about orthogonal observables at the same time that are related to our system. To perform such measurements I consider the scenario depicted in figure 6.1 and bring our system S in contact with two independent detectors 1 and 2. They produces measurement outcomes according to probability distributions. Furthermore, let both detectors do not mutually influence each other. The information we collect from an acquired dataset of each sub-ensemble is combined in a two-dimensional probability distribution $\mathrm{P}(A,B)$ spanned by the eigenvalues of the operators $\hat{A}$ and $\hat{B}$. From these measurement we are able to extract the expectation values of the observables, which are related to physical properties. The precision of the uncertainty is evaluated from the standard deviation of the A-variable and B-variable of the system. Usually repetitive measurements are performed on an ensemble, where each ensemble member is prepared in the same initial state. This is essential to make statements about the width of the distribution.

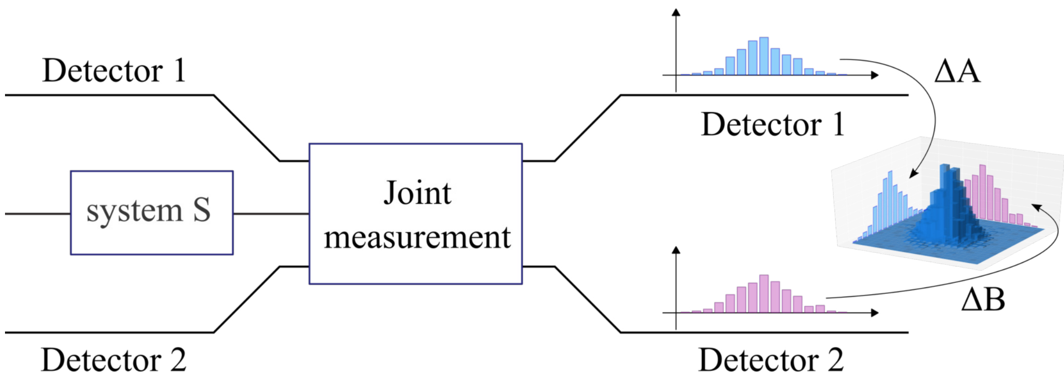

Figure 6.1.: Joint measurement on system S. The standard deviation of the A-variable and B-variable of the investigated system S are obtained from the probability distribution $\mathrm{P}(A,B)$ after a series of measurements. In order to reconstruct the distribution $\mathrm{P}(A,B)$ it is essential to repeat the measurements for a reasonable large ensemble, that is prepared in the same initial state. Only then we can estimate the expectation values concerning physical properties.

In practice, the only way to influence an experiment is by appropriate state preparations and choose measurements. Furthermore, the only observations we can make are the particular outcomes of these measurements and their respective statistics. Thereby, it will be necessary to take care of the measurement setup's individual design that always implies a relative measurement to another system, classical or quantum. From this perspective, the following line of argumentation for sub-Heisenberg indeterminacy is based on probability distributions of the measurement outcomes that refers to a relative measurement between two systems. I will start the discussion by considering the limitations of a 'classical device' that serve as a global measurement reference.

6.1.1. Limitations of semi-classical reference measurements

In their rather terse article from 1965, Arthurs and Kelly [79] theoretically investigated whether the precision limit [24]

$$\Delta\hat{X}\Delta\hat{Y} \geq 1\,, \tag{6.1}$$

for the phase and amplitude quadrature of a Gaussian wave packet can be actually achieved in a simultaneous measurement. The lower bound in equation 6.1 can experimentally be achieved, if an ensemble of a pure state is available and measurements of $\hat{X}$ and $\hat{Y}$ are 'ideal', i.e. sequentially performed on respective sub-ensembles. From the marginal distributions we can obtain the maximal information of the wave packet represented by the Wigner function introduced in chapter 2. Then the product of the distributions widths $\Delta\hat{X}$ and $\Delta\hat{Y}$ satisfies the Heisenberg uncertainty relation of equation 6.1.

In order to observe both quadratures simultaneously at times t, Arthurs and Kelly devised the following measurement procedure: Each member of an ensemble of identically prepared Gaussian states, is divided symmetrically into two sub-ensembles on a balanced beam splitter. The amplitude quadrature is measured on one half and the phase quadrature on the other half with two balanced homodyne detectors. Combining the two data sets we directly obtain the well-known phase space probability distribution $\mathrm{Q}(X,Y)$ of the Gaussian wave packet, which parses all possible values of X and Y. The Q-function is essentially introduced by K. Husimi in 1940 [80].

The gain of knowledge comes with some disadvantage. Due to the splitting, an unit of vacuum uncertainty enters the detection and the simultaneous measurements need to cope with doubled minimal quantum uncertainties. The splitting reduces the signal-to-noise ratio in comparison with ideal measurements. Instead of the sharper inequality 6.1 we get the inequality

$$\Delta\hat{X}\Delta\hat{Y} \geq 2\,. \tag{6.2}$$

The width of the marginal distributions standard deviations increases by the factor $\sqrt{2}$. The above inequality represents the fundamental precision limit when amplitude and phase quadrature of Gaussian wave packets are measured simultaneously on a single system with respect to reference values of a classical measurement device. Similar inequalities limit the simultaneous measurement of position and momentum of a particle.

This remarkable result shows the physical importance of sensing the time evolution of both quantities simultaneously of continuously changing signals. In order to show this I will consider the case of phase space trajectories of phase and amplitude modulations of quasi-monochromatic carrier light. In accordance with Arthurs and Kelly analyzes, the optimal experimental setup for a simultaneous measurement of quadratures is visualized in figure 6.2. A phase space displacement $\hat{D}(\alpha)$ can be experimentally achieved by overlapping a state $\hat{a}$ with a strong coherent field $\hat{a}_s$ on a high reflectivity beam splitter. The resulting outgoing state is excited by a pure classical phase and amplitude modulation signal with an amplitude $\alpha(t) = \alpha(\sin(\phi t) + \cos(\phi t))$, where the phase ϕ is unknown. Moreover, $\alpha(t)$ is the 'scientific signal' of interest of the interrogated system, whose time evolution is tracked.

The corresponding input state vector of the investigated system in figure 6.2 is

$$\begin{pmatrix} \hat{X}(t) \\ \hat{Y}(t) \end{pmatrix} = \begin{pmatrix} \hat{a}_1 + \alpha\sin(\phi t) \\ \hat{a}_2 + \alpha\cos(\phi t) \end{pmatrix}, \tag{6.3}$$

where the probe state $\hat{a}$ and the classical modulation signal are separated in the amplitude and phase quadrature parts. Subsequently the system is balanced splitted

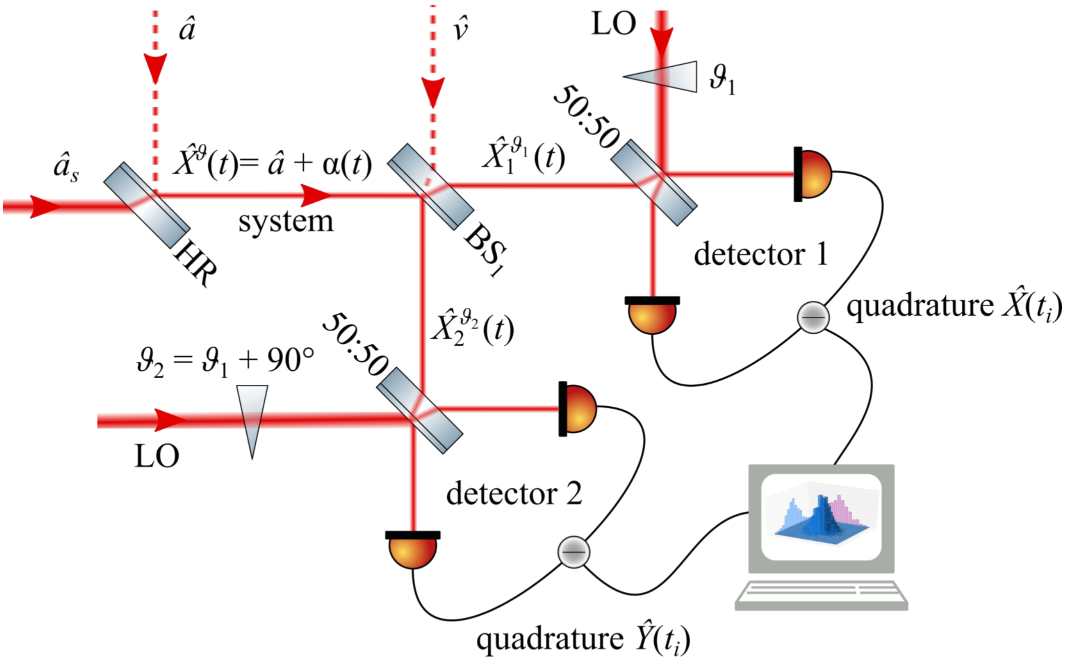

Figure 6.2.: Simultaneous measurement of amplitude and phase quadrature. To observe the phase and amplitude quadrature of a coherent displacement $\alpha(t)$ ('scientific signal') simultaneously at times t_i, it is necessary splitting the input state $\hat{X}^{\vartheta}(t)$ equally into two parts at the beam splitter BS$_1$. Each sub-ensemble is subsequently measured with two independent measurement devices; balanced homodyne detector 1 and 2. The splitting reduces the signal-to-noise ratio compared to an ideal measurement (see main text). It can be described as opening a new port through which another unit of vacuum noise $\hat{v}$ enters the detection stage.

on the beam splitter BS$_1$. Both outputs are measured with two homodyne detectors, respectively. The detected generic quadratures at each homodyne detector are

$$\begin{pmatrix} \hat{X}_1^{\vartheta_1}(t) \\ \hat{X}_2^{\vartheta_2}(t) \end{pmatrix} = \frac{1}{\sqrt{2}} \begin{pmatrix} (\hat{X}(t)+\hat{v})\cos(\vartheta_1) + (\hat{Y}(t)+\hat{v})\sin(\vartheta_1) \\ (\hat{X}(t)-\hat{v})\cos(\vartheta_2) + (\hat{Y}(t)-\hat{v})\sin(\vartheta_2) \end{pmatrix}. \tag{6.4}$$

Here vacuum $\hat{v}$ is coupled in through the 50:50 beam splitter BS$_1$. The respective quadrature is determined by the readout angle $\vartheta_{1,2}$ of the homodyne detectors. Let now on one joint output continuously measures the amplitude quadrature of the system ($\vartheta_1 = 0°$), while on the second output, the phase quadrature ($\vartheta_2 = \vartheta_1 + 90°$)

is continuously measured. Therefore, we measure the quadrature components of the signal:

$$\begin{pmatrix} \hat{X}_1(t) \\ \hat{Y}_2(t) \end{pmatrix} = \frac{1}{\sqrt{2}} \begin{pmatrix} \hat{X}(t) + \hat{v} \\ \hat{Y}(t) - \hat{v} \end{pmatrix}. \tag{6.5}$$

The photodiodes' intensities are given by the expectation value of the detected quadrature fields, which are

$$\langle \hat{X}_1 \hat{X}_1^\dagger \rangle (t) = \frac{1}{2}(\Delta^2 \hat{a}_1 + \Delta^2 \hat{v}_1 + |\alpha \sin(\phi t)|^2), \tag{6.6}$$

and

$$\langle \hat{Y}_2 \hat{Y}_2^\dagger \rangle (t) = \frac{1}{2}(\Delta^2 \hat{a}_2 + \Delta^2 \hat{v}_2 + |\alpha \cos(\phi t)|^2). \tag{6.7}$$

The detected fields hold a signal part and noise part in it. The combined signal-to-noise ratio (SNR) is defined as:

$$\mathrm{SNR} = \frac{|\alpha^2|(\sin^2(\phi t) + \cos^2(\phi t))}{(\Delta^2 \hat{a}_2 + \Delta^2 \hat{v}_2 + \Delta^2 \hat{a}_1 + \Delta^2 \hat{v}_1)} \geq \frac{|\alpha^2|}{4}, \tag{6.8}$$

for vacuum noise normalized to unity. Surprisingly, the SNR of the simultaneous measurement is four times larger than expected from the commutation relation of equation 2.7 for the phase and amplitude quadrature. The physical origin of this disadvantage is the following: each detector only determine half of the signal, while the other part is not measured. Adding both signals together, resulting just in a unity of signal power of $|\alpha^2|(\sin^2(\phi t) + \cos^2(\phi t)) = |\alpha^2|$, but whereas all four noise inputs fully contribute to the SNR.

So far, in this approach we do not consider a squeezed state. I will briefly show, why squeezed light would serve no purpose in this measurement scheme. If we choose an amplitude squeezed vacuum state with squeeze parameter r for the initial probe state $\hat{a}$, the quantum noise contribution to the detection is

$$\Delta^2 \hat{a}_1 + \Delta^2 \hat{a}_2 = e^{-2r} + e^{+2r} = 2\cosh(2r). \tag{6.9}$$

Therefore the best SNR is achieved for $r = 0$. Even though squeezed light enhances the SNR for a single variable, it does not for two conjugate variables simultaneously.

A single squeezed state is restricted to measurements with a known phase ϕ of the signal in advance. This was demonstrated and exploited in chapter 4, where the signal solely appeared in the amplitude quadrature.

6.1.2. Limitations of entanglement-enhanced measurements

To surpass the limit of inequality 6.2, the detector must be designed in a way such that the intrinsic uncertainty is not visible and only the observables are monitored.

In contrast to the measurement of the interrogated system's displacement as described above, it is now considered that the phase space displacement is measured with respect to another quantum system (providing the reference for the measurement device). The corresponding quadrature components are $\hat{X}_i$ and $\hat{Y}_j$ and fulfill the typically commutation relation

$$[\hat{X}_i, \hat{Y}_j] = 2i\delta_{ij}. \tag{6.10}$$

Furthermore, the global system encompasses two systems that are associated to a pair of canonical conjugate variables $(\hat{X}_1, \hat{Y}_1)$ and $(\hat{X}_2, \hat{Y}_2)$. Nevertheless, in the description of such a mechanical systems (classical or quantum), the variables can always be replaced by new conjugate variables $(\hat{X}_A, \hat{Y}_A)$ and $(\hat{X}_B, \hat{Y}_B)$, respectively, by an usual orthogonal transformation. This transformation corresponds to a rotation around an angle Θ in the two-dimensional phase space of $(\hat{X}_1, \hat{X}_1)$ and $(\hat{Y}_1, \hat{Y}_2)$. The new position and momentum coordinates are then given by [81]:

$$\begin{aligned}
\hat{X}_1 &= \hat{X}_A \cos(\Theta) - \hat{X}_B \sin(\Theta) \qquad & \hat{Y}_1 &= \hat{Y}_A \cos(\Theta) - \hat{Y}_B \sin(\Theta) \\
\hat{X}_2 &= \hat{X}_A \sin(\Theta) + \hat{X}_B \cos(\Theta) \qquad & \hat{Y}_2 &= \hat{Y}_A \sin(\Theta) + \hat{Y}_B \cos(\Theta)
\end{aligned}$$

Note that this does not change the properties of the systems, and therefore maintain the original variables. While the non-zero commutator $[\hat{X}_A, \hat{Y}_A] = [\hat{X}_B, \hat{Y}_B] = 2i$ leads to inequalities 6.1 and 6.2 that restrict the precision of classical measurements, the same commutator mathematically leads to the zero-commutator $[\hat{X}_A \pm \hat{X}_B, \hat{Y}_A \mp \hat{Y}_B] = 0$. It is a well-known fact that the commutator of a difference and sum of non-commuting observables of two quantum systems is zero, from which follows that those quantities are simultaneously precisely determined to each other. Since, moreover, it results from above expressions in terms of $(\hat{X}_1, \hat{Y}_1)$ and $(\hat{X}_2, \hat{Y}_2)$ we get

$$\hat{X}_A = \hat{X}_1 \cos(\Theta) + \hat{X}_2 \sin(\Theta)\,, \tag{6.11}$$

$$\hat{Y}_B = -\hat{Y}_1 \sin(\Theta) + \hat{Y}_2 \cos(\Theta)\,. \tag{6.12}$$

If we now construct a detector, that combines the measurements at angles $\Theta = 0°$ and $\Theta = 90°$ we can measure either the quantities $\hat{X}_A = \hat{X}_1$ and $\hat{Y}_B = \hat{Y}_2$ or the quantities $\hat{X}_A = \hat{X}_2$ and $\hat{Y}_B = -\hat{Y}_1$ simultaneously with arbitrary precision. Employing a suitable reference system thus allow for the measurement of a phase space trajectory with sub-Heisenberg indeterminacy. In particular, it results in

$$\Delta(\hat{X} \pm \hat{X}_0)\Delta(\hat{Y} \mp \hat{Y}_0) \geq 0 \tag{6.13}$$

from which follows that $\hat{X}$ and $\hat{Y}$ of a system are simultaneously precisely determined with respect to the corresponding quantities $\hat{X}_0$ and $\hat{Y}_0$ of a reference system. To create the condition required for a noiseless quadrature measurement we have to consider the case presented in figure 6.3. It is based on quadrature entanglement generated by two vacuum squeezed states. This is consistent with the description of the famous Gedanken-experiment by EPR, which I discussed in section 2.3.1. To enable measurements with respect to an entangled reference, two squeezed vacuum states are overlapped at a beam splitter creating an EPR-entangled state. One input is prepared in an amplitude squeezed vacuum state $(\hat{X}_1, \hat{Y}_1)$, and the second input is prepared in a phase squeezed vacuum state $(\hat{X}_2, \hat{Y}_2)$. While the interrogated systems' expectation value gets time-dependent displaced by $\alpha(t) = \langle \hat{X} \sin(\phi) + \hat{Y} \cos(\phi)(t) \rangle$, the second system serves as a reference for our measurement device (denoted with subscript '0'). Its expectation value is zero for all phases ϕ and times t; thus $\langle \hat{X}_0 \rangle = \langle \hat{Y}_0 \rangle = 0$. To measure the phase space trajectory of the interrogated system in both quadrature

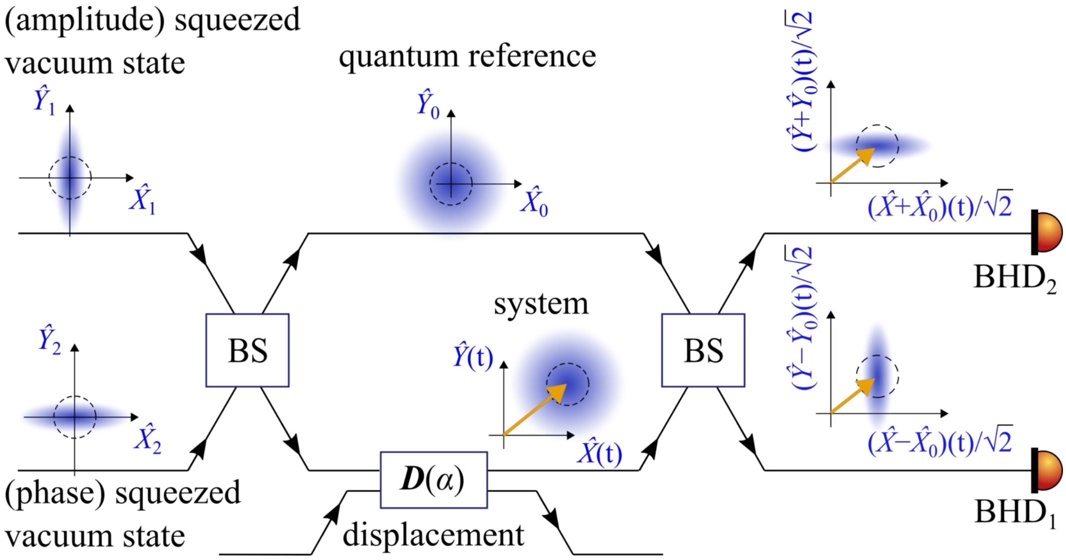

Figure 6.3.: Concept of entanglement based simultaneous measurement of displacement in orthogonal quadratures. From left to right: a beam splitter (BS) converts two squeezed vacuum states into a bipartite EPR-entangled state. One part serve as a quantum reference with zero displacement $\langle\hat{X}_0\rangle = \langle\hat{Y}_0\rangle = 0$, while the other part is excited by an time-dependent phase space displacement $\alpha(t) = \langle\hat{X}\rangle(t) + i\langle\hat{Y}\rangle(t)$. To measure the dynamics $\hat{X}(t)$ and $\hat{Y}(t)$ simultaneous at subsequent times t_i of the interrogated system, both parts of the entangled state are superimposed on a second beam splitter. Subsequently on one joint output a balanced homodyne detector BHD$_1$ measures continuously the amplitude quadrature $(\hat{X} - \hat{X}_0)(t)/\sqrt{2}$, while BHD$_2$ measures the phase quadrature $(\hat{Y} + \hat{Y}_0)(t)/\sqrt{2}$. Since their commutator vanish ($[\hat{X} - \hat{X}_0, \hat{Y} + \hat{Y}_0] = 0$), the phase space trajectory can be simultaneously precisely determined at any time t without quantum uncertainty.

simultaneously, the system is splitted in two independent subsystems at another beam splitter. The output states are given by

$$\hat{X}_1(t) = \frac{1}{\sqrt{2}}(\hat{X} + \hat{X}_0)(t) \qquad \hat{Y}_1(t) = \frac{1}{\sqrt{2}}(\hat{Y} + \hat{Y}_0)(t)$$
$$\hat{X}_2(t) = \frac{1}{\sqrt{2}}(\hat{X} - \hat{X}_0)(t) \qquad \hat{Y}_2(t) = \frac{1}{\sqrt{2}}(\hat{Y} - \hat{Y}_0)(t),$$

whereas on one joint output a balanced homodyne detector BHD_1 continuously measures the amplitude quadrature $(\hat{X} - \hat{X}_0)(t)/\sqrt{2}$. On the second output, a second BHD_2 continuously measures the phase quadrature $(\hat{Y} + \hat{Y}_0)(t)/\sqrt{2}$. The time series produced at both detectors correspond to eigenvalues of $X(t)$ and $Y(t)$, which can be interpreted as simultaneous measurements of the system's conjugate displacement time-evolution with respect to the corresponding values of the (entangled) reference. Since $\langle\hat{X}_0\rangle = \langle\hat{Y}_0\rangle = 0$, the data serves for monitoring the trajectory $(\langle\hat{X}\rangle;\langle\hat{Y}\rangle)(t)$.

However, to alleviate the lack of indeterminism of phase space sensing requires entanglement between two parties A (system) and B (reference). If the strength of entanglement between the parties is maximal, the entangled state satisfies the following correlations $\hat{X}_A = \hat{X}_B$ and $\hat{Y}_A = -\hat{Y}_B$. In that case the dynamics of the displacement values correspond to those of $\hat{X}(t)$ and $\hat{Y}(t)$, which are given by

$$\begin{aligned}\begin{pmatrix}\hat{X}(t)\\ \hat{Y}(t)\end{pmatrix} &= \frac{1}{\sqrt{2}}\begin{pmatrix}\hat{X}_A + \alpha\sin(\phi t) - \hat{X}_B\\ \hat{Y}_A + \alpha\cos(\phi t) + \hat{Y}_B\end{pmatrix}\\ &= \frac{1}{\sqrt{2}}\begin{pmatrix}\alpha\sin(\phi t)\\ \alpha\cos(\phi t)\end{pmatrix},\end{aligned} \tag{6.14}$$

without quantum noise. Thus, no noise contributes to the detection and only the displacement signal appears in the measured quadratures. Therefore, we attain

$$\Delta\hat{X}(t)\Delta\hat{Y}(t) = 0, \tag{6.15}$$

and achieve in principle an unlimited precision of our measurement device. Of course the idealized case reveals nothing about the improvement of the SNR with finite amount of squeezing. To analyze this we need to transform the input (squeezed) vacuum states $(\hat{X}_{1,2}, \hat{Y}_{1,2})$ into the entangled states $\hat{X}_{A,B}$ and $\hat{Y}_{A,B}$ using the Bogoliubov transformation

$$
\begin{aligned}
\hat{X}_A &= \hat{X}_1 \cosh(r_1) + \hat{X}_2 \sinh(r_2)\,,\\
\hat{Y}_A &= \hat{Y}_1 \cosh(r_1) - \hat{Y}_2 \sinh(r_2)\,,\\
\hat{X}_B &= \hat{X}_1 \cosh(r_2) + \hat{X}_2 \sinh(r_1)\,,\\
\hat{Y}_B &= \hat{Y}_1 \cosh(r_2) - \hat{Y}_2 \sinh(r_1)\,,
\end{aligned}
$$

from which follows similar to equation 6.14 the detected quadratures

$$
\begin{aligned}
\hat{X}(t) &= \frac{1}{\sqrt{2}}(\hat{X}_A + \alpha \sin(\phi t) - \hat{X}_B)\\
&= \frac{e^{-r_1}}{\sqrt{2}}(\hat{X}_1 + \hat{X}_2) + \frac{1}{\sqrt{2}}\alpha \sin(\phi t), \qquad (6.16)
\end{aligned}
$$

$$
\begin{aligned}
\hat{Y}(t) &= \frac{1}{\sqrt{2}}(\hat{Y}_A + \alpha \cos(\phi t) + \hat{Y}_B)\\
&= \frac{e^{-r_2}}{\sqrt{2}}(\hat{Y}_1 - \hat{Y}_2) + \frac{1}{\sqrt{2}}\alpha \cos(\phi t). \qquad (6.17)
\end{aligned}
$$

As before we need to calculate the photodiodes' intensities and find

$$\langle \hat{X}\hat{X}^\dagger \rangle (t) = \frac{e^{-2r_1}}{2}(\Delta^2\hat{X}_1 + \Delta^2\hat{X}_2) + \frac{1}{2}\alpha \sin(\phi t), \qquad (6.18)$$

$$\langle \hat{Y}\hat{Y}^\dagger \rangle (t) = \frac{e^{-2r_2}}{2}(\Delta^2\hat{Y}_1 + \Delta^2\hat{Y}_2) + \frac{1}{2}\alpha \cos(\phi t). \qquad (6.19)$$

Similar to equation 6.8 the noise power of the signal to the intrinsic noise in the combined SNR is:

$$
\begin{aligned}
\mathrm{SNR} &= \frac{|\alpha^2|(\sin^2(\phi t) + \cos^2(\phi t))}{e^{-2r_1}(\Delta^2\hat{X}_1 + \Delta^2\hat{X}_2) + e^{-2r_2}(\Delta^2\hat{Y}_1 + \Delta^2\hat{Y}_2)} \qquad (6.20)\\
&= \frac{|\alpha^2|}{2(e^{-2r_1} + e^{-2r_2})}, \qquad (6.21)
\end{aligned}
$$

where $\Delta^2\hat{X}_1 = \Delta^2\hat{X}_2 = \Delta^2\hat{Y}_1 = \Delta^2\hat{Y}_2 = 1$. Starting with finite squeezing of 10 dB for the two input states, the SNR is improved by 4 dB compared to shot noise level. From this perspective the limit of simultaneous readout for the product of the standard deviation is given by

$$\Delta\hat{X}(t)\Delta\hat{Y}(t) = 4\,e^{-2(r_1+r_2)}, \tag{6.22}$$

depending solely on the squeezed input parameter r_1 and r_2. Nevertheless for the sum of the squeeze parameters $r_1 + r_2 > 0.689$ we surpass the best achievable sensitivity for a classical reference measurement device of inequality 6.2.

6.2. Demonstration of phase space trajectories with 10 dB-reduced quantum uncertainty

The following section reports the first experimental demonstration that even the dynamics of quantum systems, i.e. phase space trajectories, can be precisely measured when employing another quantum system as reference.

In direct analogy to figure 6.3 the experimental setup presented here utilize quadrature EPR-entangled states of light to perform high sensitivity measurements on phase and amplitude modulations of quasi- monochromatic carrier light that appears in one arm of a Mach-Zehnder interferometer, which dynamics are continuously and unconditional monitored in both quadratures at the same time.

10 dB bipartite Gaussian entanglement

The strong stationary continuous-variable entangled light is produced as presented in chapter 2 and therefore an electro-optical phase control of the squeezed fields are implemented. The foundations of these experimental technique is mainly developed in [20] and a detailed description of the entanglement source is given in [82]. To create quadrature entanglement the two vacuum squeezed states are superimposed with a variable phase φ_{ent} at a 50:50 beam splitter (BS_1), as illustrated in figure 6.4. To achieve maximum entanglement, a bipartite single-sideband control loop is employed, locking the relative phase to ($\varphi_{\mathrm{ent}} = \pi/2$) between the input states.

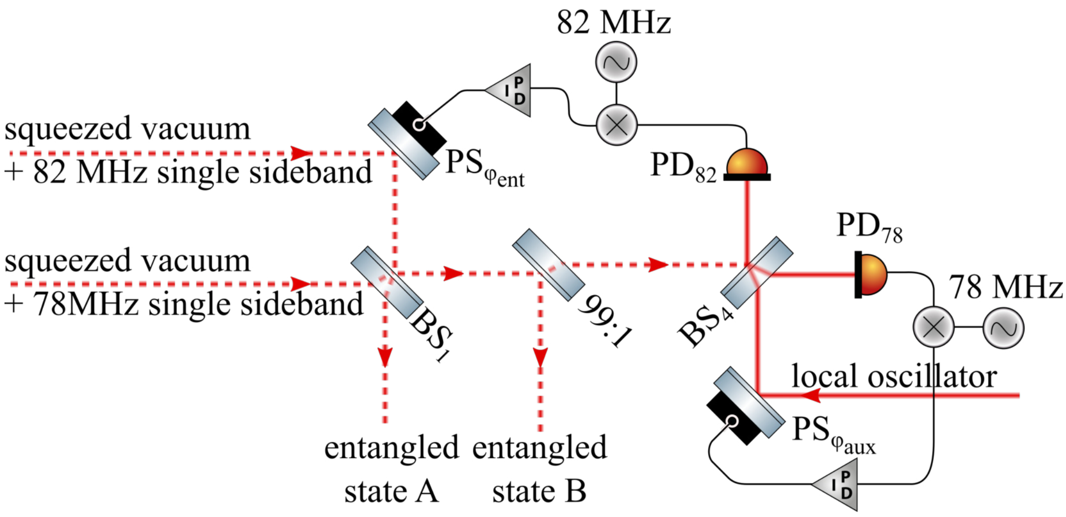

Figure 6.4.: Bipartite single-sideband control scheme for quadrature entanglement. To control the relative phase φ_{ent} between the input squeezed vacuum states at a 50:50 beam splitter (BS_1), a fraction of 1 % is tapped off from one output state and superimposed on another 50:50 beam splitter (BS_4) with a strong auxiliary local oscillator with about 8 mW of laser power. This increases the detected beat signal by the two resonant photodiodes at 78 MHz (PD_{78}) and 82 MHz (PD_{82}), respectively. Demodulating PD_{78}'s signal at 78 MHz established a permanent phase reference φ_{aux} for the entanglement phase lock. The latter was demodulated at 82 MHz and fed back to the phase shifter $\mathrm{PS}_{\varphi_{\mathrm{ent}}}$ in the path of the 82 MHz single sideband. Maximum entanglement is achieved for a phase relation of $\varphi_{\mathrm{ent}} = \pi/2$ between the input states. A similar figure was published in [20].

Since the squeezed states accompanied by the frequency shifted light with respective frequencies of 78 MHz and 82 MHz and light powers of a few μW, those are used to implement a phase lock loop. For this purpose a fraction of 1 % is tapped off from one output state. To ensure a strong error signal the tapped off beam is superimposed on another BS_4 with an auxiliary local oscillator of about 8 mW laser power. Two resonant photodiodes at 78 MHz (PD_{78}) and 82 MHz (PD_{82}) detected the beat signal in each output port, respectively. Demodulating PD_{78}'s signal at 78 MHz established a permanent phase reference φ_{aux} for the desired phase lock at the entanglement beam splitter BS_1. The latter is demodulated at 82 MHz providing the error signal that is fed back to the phase shifter ($PS_{\varphi_{ent}}$) in the path of the 82 MHz single sideband. This is to prevent for unwanted mutual influence between the phase lock and the auxiliary local oscillator.

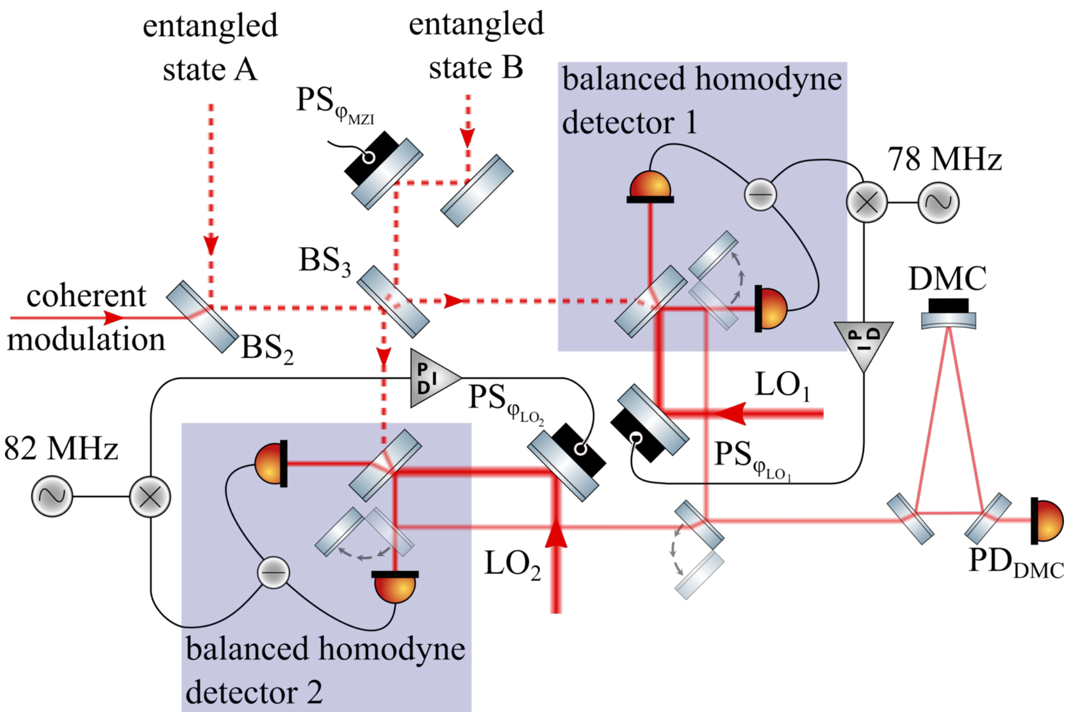

Figure 6.5.: Dual balanced homodyne detection of Mach-Zehnder interferometer outputs. Both outputs of beam splitter BS_1 were detected with balanced homodyne detectors 1 and 2. The co-propagating single sidebands (78 MHz and 82 MHz) maintain as reference for locking to squeezed uncertainty and were demodulated at the respective frequencies. The generated error signals for the readout angles ϑ of the homodyne detectors, were fed back to the phase shifters $PS_{\varphi_{LO_1}}$ and $PS_{\varphi_{LO_2}}$ in the local oscillator paths, respectively. Applying voltage to phase shifter $PS_{\varphi_{MZI}}$ the relative path could be fine adjusted. To inject a coherent modulation (displacement) it was guided through BS_S into the MZI. The diagnostic modecleaner (DMC) served as a spatial mode reference onto all laser beams propagating in different path were matched. This guaranteed a high interference contrast at the beam splitters.

After locking the relative phase between the two input vacuum states to $\varphi = \pi/2$, the existing entangled state between the outputs constitute the arms of a balanced MZI. Figure 6.5 presents the dual balanced homodyne detection to measure the two outputs simultaneously, after converting back the entangled state to two squeezed states. at the second 50:50 beam splitter (BS_3) of MZI. The co-propagating single sidebands (78 MHz and 82 MHz) maintain as reference for locking to squeezed uncertainty. Beating with the local oscillator (LO) at the 50:50 beam splitter and demodulating the electronic signal at the respective frequencies, generates an error signals for the readout angles ϑ of the balance homodyne detectors 1 and 2. Those are fed back to the phase shifter $PS_{\varphi_{LO_1}}$ and $PS_{\varphi_{LO_2}}$ in the local oscillator paths, respectively. Therefore we could either measure the phase or amplitude quadrature at the outputs. To achieve equality of the arm length in the MZI, an additional phase shifter ($PS_{\varphi_{MZI}}$) is placed in one arm. By applying voltage to the piezo-actuator, fine tuning of the relative paths are possible. Essentially high interference contrast at each beam splitter is achieved by using a diagnostic mode cleaner that serves as a spacial mode reference. All beams propagating to the homodyne detectors are matched to this cavity, provided a spatial overlapped along the paths. Nevertheless, due to necessarily imperfect interference contrasts at the two beam splitters, the final squeeze factors could only be lower than the initial squeeze factors of the input states (subscripts 1 and 2 in figure 6.6). Figure 6.6 shows the schematics of the table-top experiment. Two continuous-wave fields A and B that carried entangled quantum noise of the modulations at frequency of $\Omega/2\pi \pm \Delta\Omega/2\pi = 5\,\text{MHz} \pm 20\,\text{kHz}$ are produced from squeezed vacuum states. To demonstrate monitoring of dynamical phase space trajectories with sub-Heisenberg indeterminacy, the interrogated system is overlapped with a time-dependent displacement $\alpha(t) = \langle\hat{X}\rangle(t) + i\langle\hat{Y}\rangle(t)$. To achieve that, the respective beam is superimposed with another one that carried a coherently excited modulation at 5MHz at the highly reflectivity mirror BS_2 (R = 99.99 %). The high reflectivity minimized decoherence, i.e. optical loss to the entanglement. The actual displacement $\alpha(t)$ corresponded to the small transmitted fraction of the coherent beam.

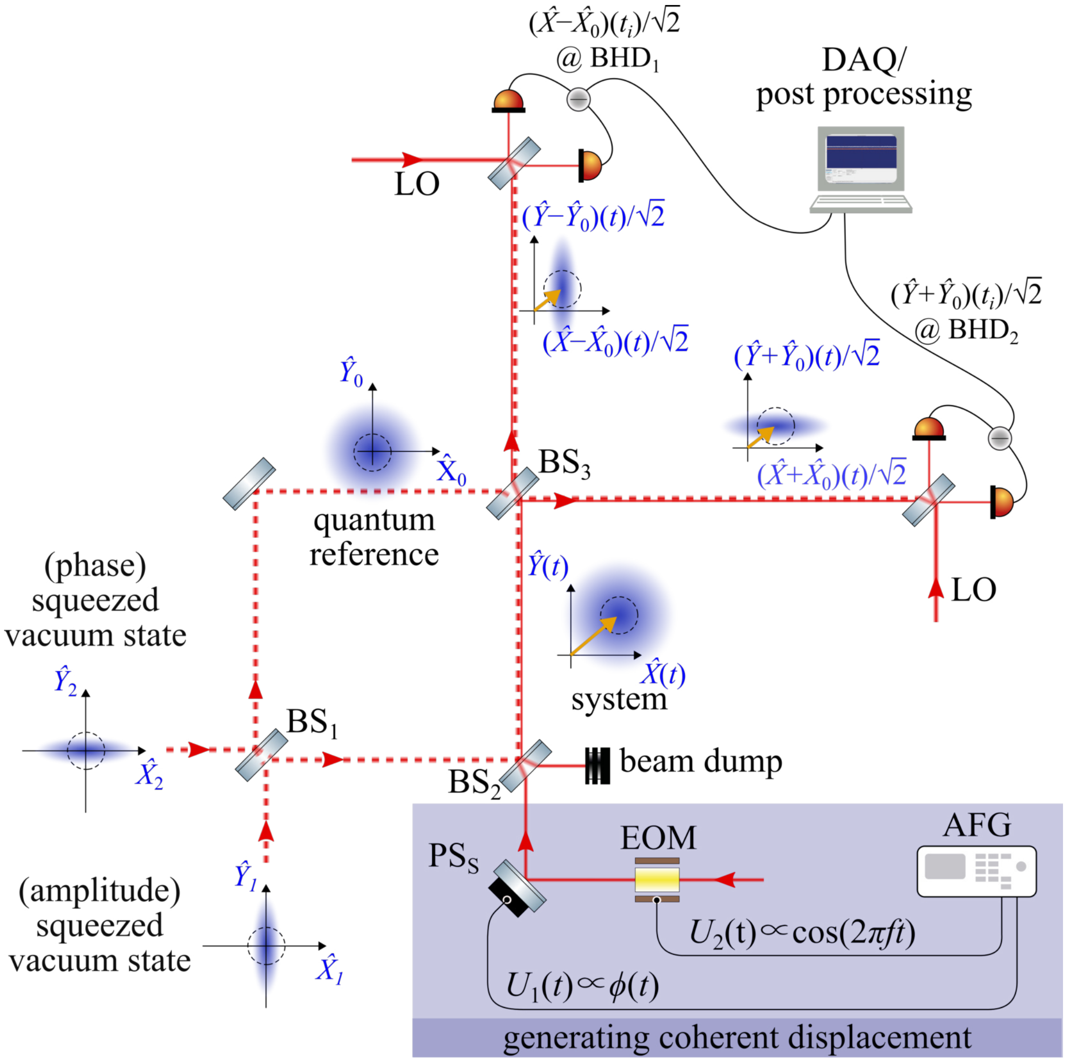

Figure 6.6.: Schematics of the experimental setup. The phase space pictures show the quantum uncertainties of the laser beams' modulations at $\Omega/2\pi = 5MHz$ at several instances. From bottom left to top right: balanced beam splitter BS$_1$ converted two squeezed vacuum states into a bipartite EPR entangled state. One part served as a quantum reference (subscript 0). The other part was displaced by $(\langle \hat{X} \rangle ; \langle \hat{Y} \rangle)(t)$ (illustrated by the arrow) by overlapping modulated light transmitted through BS$_2$. The two projections of the arrow were simultaneous monitored with respect to the entangled reference system by superposition at BS$_3$ and by detecting the outputs with balanced homodyne detectors. BHD$_1$ provided eigenvalues of $(\hat{X} - \hat{X}_0)(t_i)/\sqrt{2}$, while BHD$_2$ provided eigenvalues of $(\hat{Y} + \hat{X}_0)(t_i)/\sqrt{2}$, with $\langle \hat{X}_0 \rangle = \langle Y \rangle_0 = 0$. EOM: Electro-Optical Modulator, AFG: Arbitrary Function Generator, DAQ: Data AcQuisition, LO: Local Oscillator.

Changing the peak voltage to the electro-optical modulator (EOM, as shown in figure 6.6), changed the absolute value of the displacement $|\alpha|$. Changing the DC voltage to the piezo-actuated phase-shifter (U_1) changed the differential excitation in $\langle \hat{X} \rangle (t)$ and $\langle \hat{Y} \rangle (t)$. Therefore the *type* of modulation is continuously varied in time by varying the relative phase angle ϕ at which the fields were combined at BS_2.

Data Acquisition

For recording the data the electronic signals of the homodyne detectors are splitted and sent to a spectrum analyzer and to a two-channel data acquisition card (DAQ). Primarily, the spectrum analyzers serve as monitoring, to verify that the read out phase is stable during the measuring time. The voltages from the BHD's are recorded with a sampling frequency of 200 MHz for each channel of the DAQ. To avoid aliasing effects an analog lowpass-filter with a cut-off frequency of $f_{-3dB} = 50\,\text{MHz}$ is applied before each channel. Post processing is done with a self-written python script (see Appendix A.1), which is used to digitally demodulate the data of the signal frequency at 5 MHz and subsequent FIR-lowpass-filtering with a cut off frequency of 10 kHz. To avoid correlation in the data set after lowpass-filtering, every 1500th-data point is used.

The measurement sequence to track the phase space trajectory of displacement is divided into the following parts:

1. Precondition: preparing the entangled state as described above (cf. figure 6.4) and lock both homodyne detectors to squeezed uncertainty, whereby one continuously measures the phase quadrature $\hat{Y}(t_i)$ and the other the amplitude quadrature $\hat{X}(t_i)$.

2. set the amount of samples that can be acquired during the full ramp only on the positive slope, which is simply: $\text{samples}_{\text{tot}}$ = sampling frequency [Hz]/ (ramping frequency/2) [Hz]

3. the data acquisition starts when the DAQ-card receive the external TTL-trigger from the arbitrary function generator (AFG), which is phase locked to the

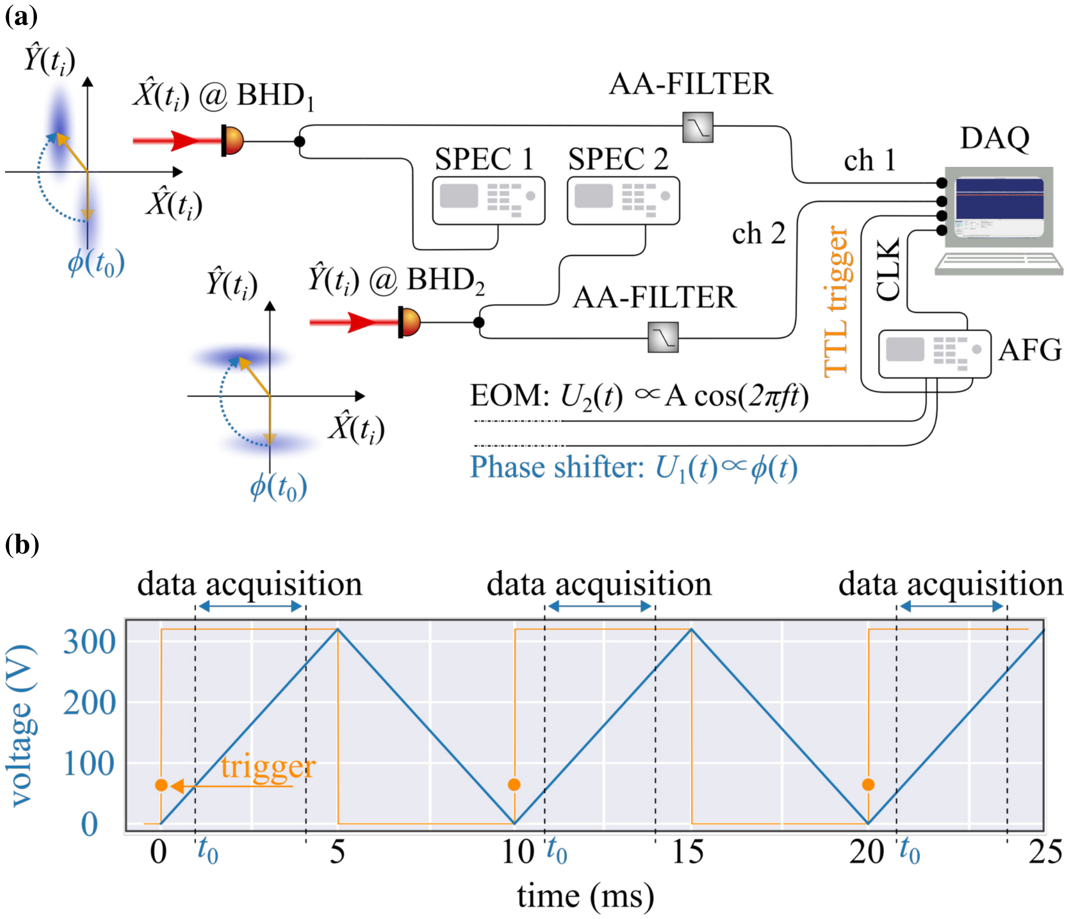

Figure 6.7.: Data acquisition of measurement sequence. (a) The measured voltage at times t_i from the detector's BHD_1 and BHD_2 were buffered, splitted and send to a spectral analyzer (SPEC 1, SPEC 2) and to the two-channel data acquisition card (DAQ). To avoid aliasing effects (sampling rate 200 MHz) a suitable analog anti-aliasing filter (AA-Filter) with a cut-off frequency of $f_{-3dB} = 50\,\mathrm{MHz}$ was added before each input channel. Synchronizing between generating and sampling the signal was achieved by using the functions generator clock (clk) as reference for the data acquisition card. To extract the actual signal the demodulation was done digital in post processing. (b) Sequence of measurement starts, when the DAQ-card receive the external TTL-trigger from AFG.

ramp voltage applied to the phase shifter (PS_s) rotating the signal around $\phi(t)$ in phase space.

4. recording the samples was done after a certain delay time (defined by pre-trigger samples) at t_0, to ensure linear behavior of the piezo-actuator of PS_s.

5. repeat the measurement sequence after each trigger event, until a certain amount of samples is recorded and thus gives an average of the trajectory.

6.2.1. Experimental results

The results of the experiment are presented in the following. The orthogonality of the readout quadratures is validated during the measurement process with two spectrum analyzers as shown in figure 6.7. To evaluate the strength of the entanglement between the two parties of the bipartite entangled system (Two-mode squeezed state), is possible by comparing simultaneous measurement results of the two output states at the balanced homodyne detectors. They reveal strong correlations which surpass the limit by the EPR-Reid criterion 2.56.

The Figure 6.8 shows the variance of $X(t_i)$-data and $Y(t_i)$-data, which are simultaneously taken with respect to the entangled reference. The limit correspond to twice the systems ground state uncertainty. By how much this limit is beaten, is immediately a measure of the entanglement strength and demonstrates a violation of the inequality 6.2. Here the uncertainty product is $\Delta(\hat{X}(t_i))\Delta(\hat{X}(t_i)) \approx 0.2$, which is a factor 10 better compared to any classical measurement device without entanglement.

The case of a sub-Heisenberg stationary displacement (not time-dependent) show the green data points in figure 6.9. The data are sampled with the data acquisition card at subsequent times t_i. Every simultaneous measurement of the phase and amplitude quadrature is performed on a single time window; subsequent simultaneous measurements are performed on subsequent time windows. Plotted are individual measuring points $(X(t_i);Y(t_i))$ taken every 5 ns with respect to the quantum reference system. The blue dots are individual data points from simultaneous measurements of $(X-X_0)(t_i)$ and $(Y+Y_0)(t_i)$, when the entanglement source

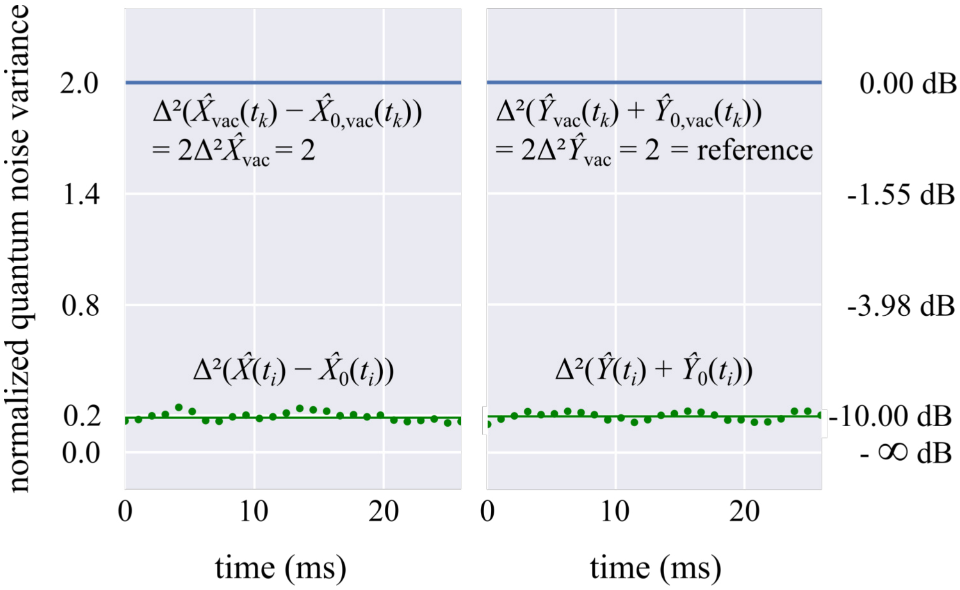

Figure 6.8.: Sub-Heisenberg indeterminacy of a stationary state in time domain. Variances of $X(t_i)$-data (left) and $Y(t_i)$-data (right), which was simultaneously taken with respect to the entangled reference. Shown is the example of stationary zero displacement, i.e. $\langle \hat{X}(t) \rangle = \langle \hat{Y}(t) \rangle = 0$. Solid lines correspond to the variance of 2600 measuring points each, without entanglement (top lines) and with entanglement (bottom lines). The latter corresponds to 10dB two-mode squeezing. The two types of modulations can be measured simultaneously with an uncertainty product of $\Delta(\hat{X}(t_i))\Delta(\hat{X}(t_i)) \approx 0.2$ violating inequality 6.2 by a factor of 10. Here, $\Omega/2\pi$ = 5 MHz and $\Delta\Omega/2\pi$ = 20 kHz. Dots represent variances calculated over 260 consecutive measuring points.

was switched off and the modulations $\langle \hat{X} \rangle$ and $\langle \hat{Y} \rangle$ set to zero. These data points accumulated around the phase space origin and is used to derive the factor by which the inequalities 6.1 and 6.2 are surpassed. The corresponding probability density is the Q function, which marginal statistical distribution P($X(t_i)$) and P($Y(t_i)$) of the respective quadratures are shown together with the stationary displacement using an entangled reference in the outer panels. From these distributions the standard deviations are determined. The orange circle encloses the standard deviation of the displacement around $(\langle \hat{X} \rangle ; \langle \hat{Y} \rangle) = (0.6/\sqrt{2};-2.4\sqrt{2})$.

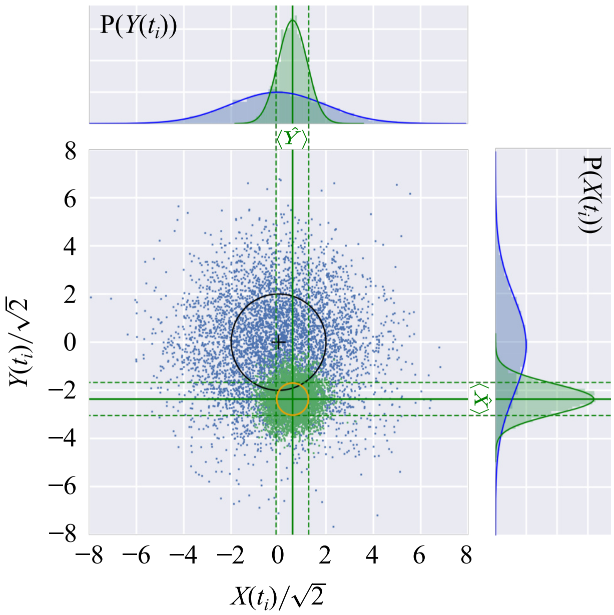

Figure 6.9.: Sub-Heisenberg indeterminacy of a stationary displacement. Using the setup in figure 6.6, I performed a time continuous measurement on an ensemble of identically prepared Gaussian wave packets. The outer panels show two statistical results from simultaneous $\hat{X}$ and $\hat{Y}$ measurements, respectively. The central picture is the corresponding Q-function. The broader distributions are measurements with respect to a classical reference and fulfill HUR. The narrow distributions are measurements results using an entangled reference. In this case no HUR applies. The variances of $\hat{X}$ and $\hat{Y}$ were both a factor of 10 below the lowest possible classical variances. The expectation values are $\langle\hat{X}\rangle = 0.6/\sqrt{2}$ and $\langle\hat{Y}\rangle = -2.4/\sqrt{2}$ with a standard deviation enclosed by the orange circle. Measurements were performed at a frequency of $\Omega/2\pi = 5$ MHz with $\Delta\Omega/2\pi = 20$ kHz on continuous-wave light.

Figure 6.10 shows two phase space trajectories $((\langle\hat{X}\rangle;\langle\hat{Y}\rangle)(t)$ (solid lines) measured with a precision surpassing inequalities 6.1 and 6.2 . Added are individual data points from simultaneous measurements of$(X - X_0)(t_i)$ and $(Y + Y_0)(t_i)$, when the interrogated system is entangled with the reference system. The standard deviations in $(X - X_0)(t_i)$ and $(Y + Y_0)(t_i)$ around the actual phase space trajectories $((\langle\hat{X}\rangle;\langle\hat{Y}\rangle)(t)$ (solid line) are reduced by more than $\sqrt{10}$ in comparison to the

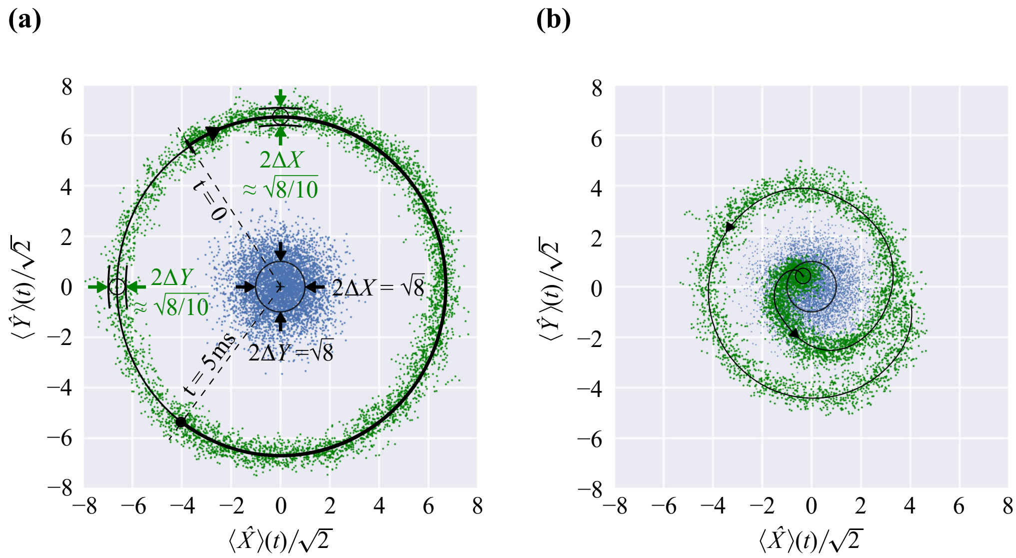

Figure 6.10.: Measured trajectories with sub-Heisenberg indeterminacy. The example phase space trajectories of about 5ms length measured with sub-Heisenberg indeterminacy (solid line surrounded by green dots) in comparison to measurements on ground states (centered, blue dots). The dots represent single measurements $((X - X_0)(t_i); (Y + Y_0)(t_i))$ performed at subsequent times t_i , with $t_{i+1} - t_i = 7.5\,\mu s$. To increase the number of points I superposed 8 identical measurements, respectively. The spreads of the data points in the two phase space directions represent the relevant standard deviations of quantum noise in estimating the trajectories. The sub-Heisenberg uncertainty area is revealed by comparing the small circles to larger ones in the centers, which represent the lower bound in inequality 6.2. The latter is surpassed by a factor of about ten. The trajectory in (a) represents a changing type of modulation at constant modulation depth. The one in (b) additionally shows a continuously decreasing modulation depth.

standard deviation around the phase space origin when the entanglement source is switched off. This factor is highlighted by the different radii of the small circles. The phase space trajectories shown in figure 6.10 are thus tracked with an uncertainty product that violated inequality 6.2 by slightly more than a factor of 10 and inequality 6.1 by slightly more than a factor of 5. As expected, the factor by which Heisenberg's uncertainty limit is surpassed directly corresponded to the strength of the entanglement. Increasing the entanglement strength requires further reduction of optical loss, including further increase of photo-electric detection efficiency. The figure 6.10 (a) shows a trajectory with constant modulation depth, but the kind of modulation continuously changed. The system had a pure amplitude modulation when $\langle\hat{Y}\rangle(t) = 0$ and a pure phase quadrature modulation when $\langle\hat{X}\rangle(t) = 0$. The amplitude of the AC voltage at the EOM (U_2) is constant and just the DC voltage at the piezo actuator (U_1) continuously changed. The trajectory started at about $(\langle\hat{X}\rangle;\langle\hat{Y}\rangle)$ = (-3/$\sqrt{2}$;5.8$\sqrt{2}$), completed almost two full cycles and stopped at about $(\langle\hat{X}\rangle;\langle\hat{Y}\rangle)$ = (-4/$\sqrt{2}$;-5.5$\sqrt{2}$). The figure 6.10 (b) shows another example trajectory, whose modulation depth also changed, resulting in a phase and amplitude dependent trajectory. My setup would provide the same relative reduction in quantum measurement uncertainty for arbitrary trajectories including random walks.

6.3. Discussion and conclusion

In conclusion, my experiment proved the principle that time-dependent phase space trajectories $(\langle X\rangle;\langle Y\rangle)(t)$ can be monitored with a precision strongly surpassing Heisenberg's uncertainty relation. The lower bound of inequality 6.1 is surpassed by a factor of five. The measured uncertainty area is even ten-times below the more relevant bound of inequality 6.2 that limits phase space monitoring with respect to a classical reference. The factors of five and ten are given by the strength of the entanglement between interrogated system and the reference system. The factors achieved are of practical significance and support the emergent field of quantum sensing. This experiment quantitatively confirms that in principle a phase space trajectory can be precisely monitored on the basis of a single simultaneous measurement of conjugate observables on one copy at a time. Thus I conclude that the often quoted interpretation of Heisenberg's uncertainty relation 'two non-commuting observables of a quantum system cannot be measured simultaneously with arbitrary precision' is incorrect. In light of the experiment, the statement becomes correct, if completed by '...with respect to a reference system that has been coupled to the environment'. In this case the reference system cannot be quantum correlated. Furthermore the experiment confirms the inherent determinism of the

Schrödinger equation [83], since the results show that trajectories of freely evolving physical systems are precisely determined if they are decoupled from the environment. From this perspective Heisenberg's uncertainty relation arises because a classical measurement device can at best use a reference of close to zero temperature. In this view, quantum uncertainties are associated with the measurement references but not with the system being measured.

7. Conclusion and prospect

To this day, the development of modern quantum technologies in optical measurements relies on quantum correlated states of light. Therefore, well engineered light sources that are precisely controllable enable a broad range of new applications in sensing and monitoring of various signals. On the other hand, a deep understanding of the fundamental principles of quantum physics background is necessary to take full advantage of those new technologies. While as a whole, the focus of my thesis is on the investigation of quantum uncertainty in measurements, it encompasses one part of true technological application with squeezed light in quantum sensing and the other part of the fundamental role of the Heisenberg uncertainty relation.

To study these aspects, I have set up two squeezed light sources consisting of resonator-enhanced degenerate type-0 optical-parametric amplification in periodically poled potassium titanyl phosphate at a wavelength of 1550 nm. In principle, each device had the capability to produce squeezed light with a noise reduction in the squeezed quadrature of more than 10 dB compared to the vacuum noise at the sideband frequency of around 5 MHz.

In this work, I present the experimental realization on the application of squeezed states of light in interferometric measurements. To my best knowledge, I have achieved the strongest non-classical sensitivity improvement in a Mach-Zehnder interferometer with continuous-wave squeezed light. When the (amplitude) squeezed vacuum was injected into the interferometer's signal port, the directly observed noise power reduction in the output of the Mach-Zehnder interferometer was (-10.5 ± 0.1) dB compared to a vacuum input. In this case, the artificial signal was detected with an improved signal-to-noise ratio by a factor of 3.35, equivalent to an 11.2-fold increase of coherent light power. The corresponding anti-squeezed quadrature shows a noise power of (21.2 ± 0.1) dB above the vacuum noise, by which a total loss of $(7.8 \pm 0.2)\,\%$ can be inferred. This result contributes to mitigate the quantum noise of laser light in next generation of gravitational wave detectors. For example the planned Einstein-telescope will most likely operate at a wavelength of 1550 nm as used here. In principle, even higher squeezing values can be reached, when a doubly resonant squeezed-light source and sophisticated phase-matching temperature control are used instead, as in [21] for example.

Further, an analysis of a new concept to estimate absorption of photosensitive samples in the Mach-Zehnder interferometer is presented. In this proof-of-principle we have shown that the loss of a 99:1 beam splitter is independent of the detection efficiency η_{det} of the used photodiodes. This new approach may lead to applications for on-chip based measurements of photosensitive biological samples. Moreover, absolute calibration of the photodiodes is not necessary. We derived a simplified model of the measured noise power spectra in the amplitude and phase quadrature describing the interference of the correlated bipartite squeezed light for different relative phases of the Mach-Zehnder interferometer. In a future experiment it will be useful to probe for different absorption values inserted into one arm of the interferometer and compare these results with the theoretical prediction. On the theoretical side a complete (theoretical) model of this new technique would be desirable, which also includes other imperfections, e.g. additional loss in the arms and the unbalance of the beamsplitters.

Measurements of conjugate quantities with classical devices reveal a limit on the achievable precision for a simultaneous single measurement based on Heisenberg's uncertainty relation. I have achieved the first demonstration of a continuous and unconditional monitoring of dynamical phase space trajectories measured with sub-Heisenberg indeterminacy. The implemented continuous-variable EPR-entangled state from the two squeezed light sources enables the possibility to observe the canonical conjugate amplitude and phase field quadratures simultaneously with a precision higher than feasible for any quantum mechanical system without quantum correlations. Since the time-evolution of the interrogated system was measured with respect to an entangled quantum reference, I was able to track the trajectory $(\langle\hat{X}\rangle\,;\langle\hat{Y}\rangle)(t)$ with a precision more than a factor of 5 better compared to an ideal measurement (cf. inequality 6.1). More importantly, the precision was ten-times below the relevant bound that limits phase space monitoring with respect to a classical reference (cf. inequality 6.2). The factor by which Heisenberg's uncertainty limit is surpassed directly correspond to the strength of entanglement. This property indeed allows for arbitrarily precise measurement values simultaneously performed on conjugate quantities. Thus, I conclude that the often quoted interpretation of Heisenberg's uncertainty relation 'two non-commuting observables of a quantum system cannot be measured simultaneously with arbitrary precision' is incorrect. The statement becomes correct, if completed by '...with respect to a reference system that has been coupled to the environment'. If the interrogated system is maximally entangled with the reference system, and thereby perfectly decoupled from the environment, the precision in every pair of simultaneous measurements at any time t is unlimited. This provides a perfectly determined phase space trajectory as in classical physics. From this perspective quantum uncertainties are associated with measurement references, but not with the measured system.

In practice, limitations occur due to decoherence in terms of photon loss, which reduces the strength of the entanglement. From that, I show a lower bound for the precision in the uncertainty relation $\Delta\hat{X}(t)\Delta\hat{Y}(t) \geq e^{2(r_1+r_2)}$, where r_1 and r_2 correspond to strength of the squeeze factors of the input states.

Moreover, the scientific results are of practical significance and thus support the emergent field of quantum sensing based on entanglement. At the frontier of the foundations of quantum mechanics, these experiments have demonstrated the prospects of quantum correlations for new technological capabilities. On the other hand it shows impressively that specific properties of quantum systems, that were entitled by A. Einstein as 'spooky interaction at the distance' hundred years ago, are well controllable and understood today.

A. Appendix

A.1. Data analysis and post processing for sub-Heisenberg trajectories

To acquire the data of chapter 6, I used a fast dual channel data acquisition card *PX14400A* from Signatec, wich could acquire up to 400 MS/s on each channel with a resolution of 14-bit. The card saved the recorded data directly into a binary file, which was buffered by the onboard RAM and transferred via the PCIe interface to the host PC. To process the data in the post processing it was necessary to convert the raw data from the stored binary to the corresponding voltage value. The following python code shows the post processing of the acquired data sets.

```python
import os
import numpy as np
import matplotlib.pyplot as plt
from nqlab import io
import scipy
import scipy.signal
from nqlab.analysis.fft import *
import array
import pandas as pd


def binary_to_integer(files, divider = 4):

```

```
     output=[ ]
 ### get size of the file in Bytes
 Nbytes = os.path.getsize(files)

 with open(files, 'rb') as source:

  for Mbyte in range(int(Nbytes/1048576)):
      ### Read 1 Megabyte from the file at a time
      ### and process that
      buffer = source.read(1048576)
      for index in range(int(1048576/2)):
         measPoint = int.from_bytes(
                    buffer[2*index:2*index+2],
                    byteorder = 'little',signed=False
                    )//divider
                   #divide by 4 (b100) to get only
                   #the upper 14bits. Last 2bits always zero
               output.append(measPoint)
        return output

def convert_int_to_voltage(output, Umax = 220):
        if type(output) is list:
            output = np.array(output)

        return (output-8192)*(Umax/2**14)


data = {} #creates a dictionary

### path to data
path='\lab_026\measurements\19.03.2019\Time domain'
os.chdir(path)
```

```
### acquired data from data acquisition card PX1440
files = ['trajectory.rd16','vacuum.rd16']

for f in files:
    file = binary_to_integer(f)
    data[f.split('.')[0]] = convert_int_to_voltage(file)

    dataset = pd.DataFrame(data)

    channel_1 = dataset.iloc[0::2].reset_index(drop=True)
    channel_2 = dataset.iloc[1::2].reset_index(drop=True)

### setting parameters for digitial demodulation
fs=200e6 #sampling rate DAQ
phi=0      #phase Local oscillator
A=10.   #amplitude Local oscillator
f=5e6      # demodulating frequency
t=np.arange(len(channel_1))/fs #time

### defining the Local oscillator for demodulating
LO = A*np.sin(2*np.pi*f*t + phi)

demodulated_signal_1 = channel_1.mul(LO,axis=0)
demodulated_signal_2 = channel_2.mul(LO,axis=0)

### avoiding correlations in dataset
lowpass = (scipy.signal.firwin(10000,10e3,window="blackman",
                                                    nyq= fs/2), 1.0)

data_new_1 = scipy.signal.lfilter(lowpass[0],lowpass[1],
                     demodulated_signal_1, axis=0)[0::1500]
```

```
data_new_2 = scipy.signal.lfilter(lowpass[0],lowpass[1],
                        demodulated_signal_2, axis=0)[0::1500]
```

In figure A.1, I plotted the data processed with the python code shown above, corresponding to the result obtained in section 6.2.1. The phase quadrature is obtained from ‘data_new_2’ and the amplitude quadrature from ‘data_new_1’.

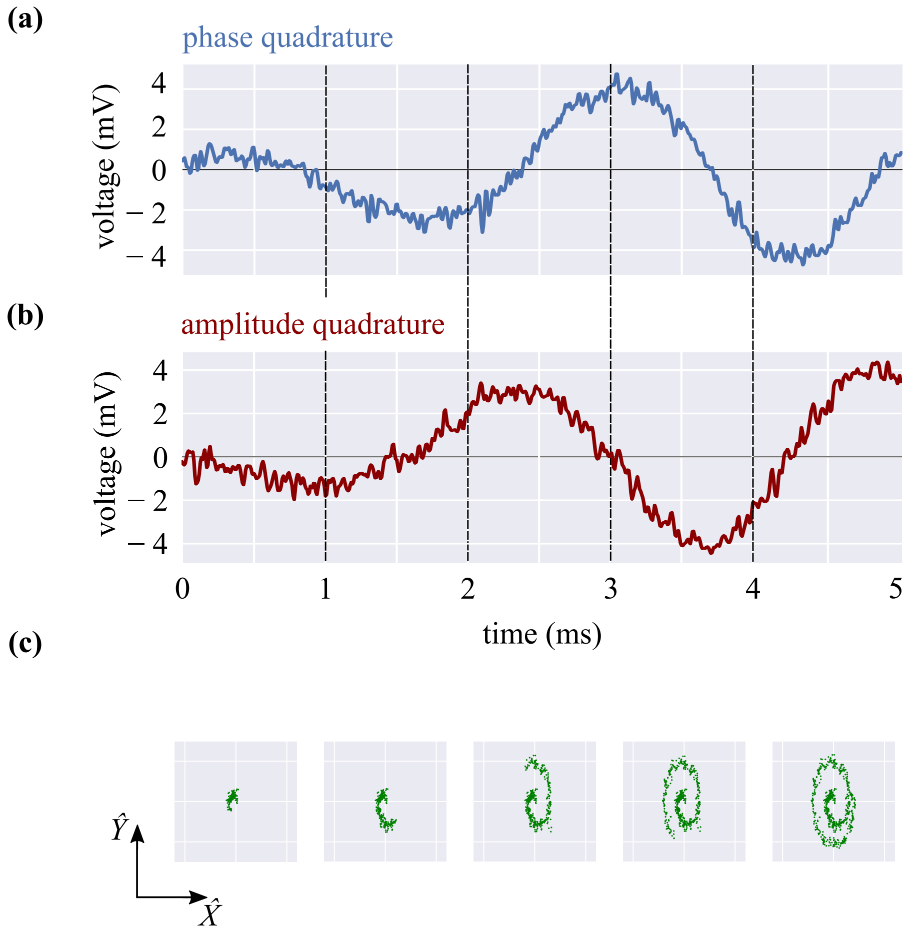

Figure A.1.: Time-evolution of sample trajectory. Plotted are the time-evolution of the phase quadrature (a) and the amplitude quadrature (b) acquired with the data acquisition card for a single passage of 5 ms duration. In (c) the covered phase space trajectory after each segment (vertical dashed line in (a) and (b)) in steps of 1 ms is displayed.

Synchronization of data acquisition card

The figure A.2 shows the demodulated signal at different demodulation frequencies around the generated signal's frequency f = 5 MHz. When the data acquisition card was not synchronized with the function generator, the phase between the generated signal and the acquired data drifted apart and showing an elongated trace. This was later avoided by using the function generators reference clock as external clock for the data acquisition card.

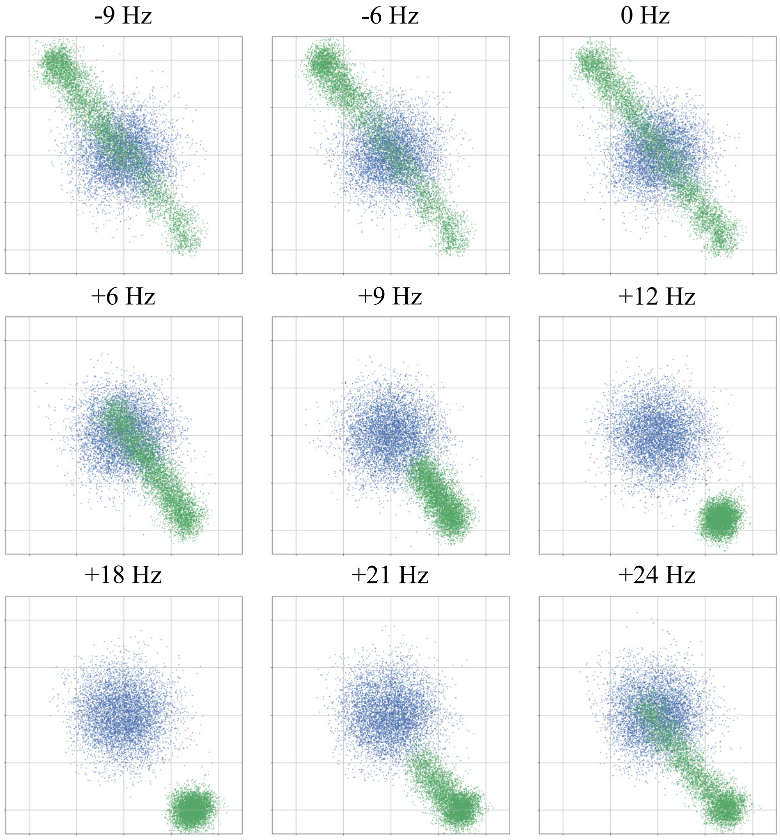

Figure A.2.: Different demodulation frequencies around the signal's frequency f = 5 MHz. The demodulation frequency was changed in a range between f_{dem} = f - 9 Hz and f_{dem} = f + 24 Hz, while the data acquistion card was not synchronized with the function generator. In each plot the horizontal axis correspond to the amplitude quadrature and the vertical axis to the phase quadrature.

A.2. Frequency domain of sub-Heisenberg stationary signal

The frequency domain plots in figure A.3 show the stationary signal, whose time domain is presented in figure 6.9. The signal was simultaneously measured with a spectrum analyzer. In both quadratures the signal appears at a frequency of 5 MHz with a noise power reduction of more than 10 dB (green) compared to the vacuum noise level (blue).

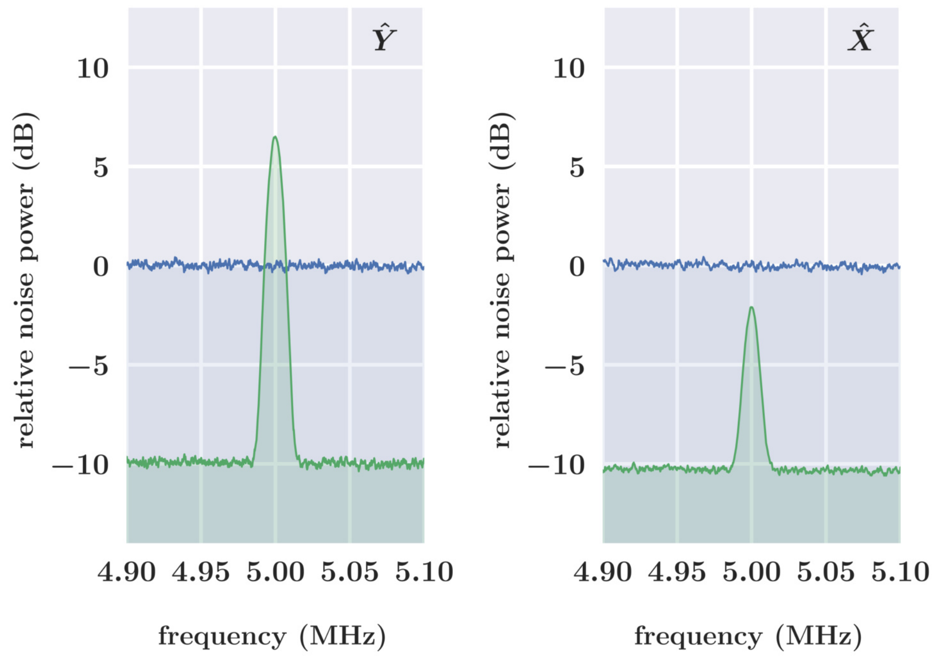

Figure A.3.: Sub-Heisenberg indeterminacy of a stationary state in frequency domain. The blue traces show vacuum fluctuations, when the signal port of the homodyne detectors were blocked. The green traces show the normalized simultaneously squeezed quadrature noise power spectra of the signal's variance $\Delta^2 Y = (-10.1 \pm 0.1)$ dB and $\Delta^2 X = (-10.3 \pm 0.1)$ dB at a modulation frequency of $\Omega/2\pi = 5$ MHz. The slight slope of the traces is due to the decreasing transfer function of the homodyne detectors. All traces were recorded with a resolution bandwidth of $\Delta\Omega/2\pi = 10$ kHz, a video bandwidth of 30 Hz.

A.3. Theoretical calculation of detection loss dependency in absorption measurement

For completeness, this short section shows the corresponding calculated ratio S^{ratio} from the theoretical spectra obtained by the equation 5.9 and 5.10. The ratio is given by

$$S^{\text{ratio}} = \frac{S^a(\phi)}{S^b(\phi)} = \frac{A}{B}, \tag{A.1}$$

with

$$\begin{aligned}
A =& e^{4r}\eta_{det}(\sqrt{\eta_s} - \cos(\phi))^2 \\
& - e^{2r}(-4 + \eta_{det} + \eta_{det}\eta_s - 2\sqrt{\eta_s}\eta_{det}\cos(\phi)) + \eta_{det}\sin^2(\phi), \\
B =& \eta_{det}(\sqrt{\eta_s} - \cos(\phi))^2 \\
& - e^{2r}(-4 + \eta_{det} + \eta_{det}\eta_s - 2\sqrt{\eta_s}\eta_{det}\cos(\phi)) + e^{4r}\eta_{det}\sin^2(\phi).
\end{aligned}$$

Equation A.1 is dependent on the detection efficiency η_{det}, which is plotted in figure A.4. The theoretical prediction is also in good agreement with experimental data (cf. figure 5.7), and shows that the simple assumption made are sufficient to describe experimental results.

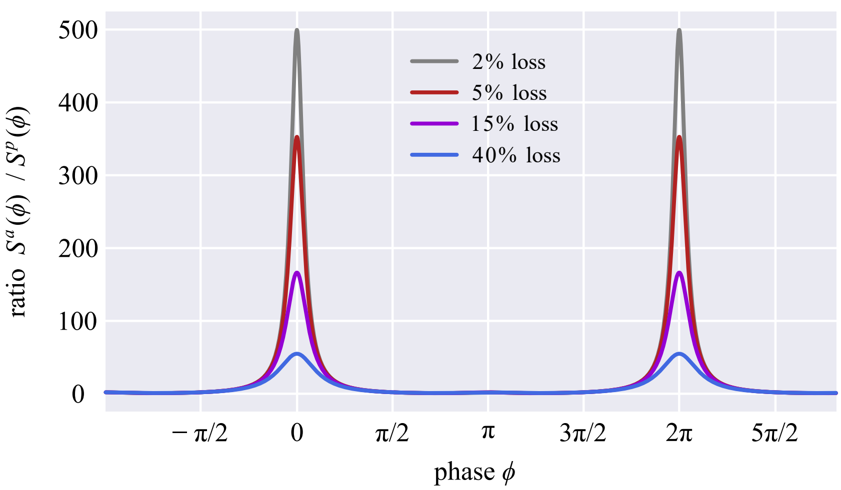

Figure A.4.: Theoretical plot of S^{ratio}.

Danksagung

Und plötzlich ist da am Ende noch so viel zu sagen. Denn am Ende fällt der Blick auf den zurückgelegten Weg. Das schönste daran sind natürlich die Erinnerungen an die verrückten, großartigen und faszinierenden Augenblicke. Tage, in denen alles klappt und vor allem Tage, wo einfach nichts zu funktionieren scheint. Jene Momente, wo alles auf einmal glasklar ist und dann einem wieder alles nebulös vorkommt. Jeder dieser Momente war einzigartig; einzigartig wurde es durch die Menschen, die Teil daran hatten und mit denen ich die letzten Jahre viel Zeit verbringen durfte. Deshalb bin ich richtig glücklich. Denn das, was am Ende wirklich bleibt, sind meine Kollegen, Freunde und Kollegenfreunde (Habe ich gerade erfunden). Und das wichtigste im Leben, meine Familie. Das alles bedeutet viel für mich. Umso schwerer ist es Danke zu sagen, für die Unterstützung, unentbehrliche Hilfe und mühevolle Geduld zu jeder Zeit. Aber ich versuchs mal kurz.

Zunächst bedanke ich mich bei meinem Doktorvater Roman Schnabel, der mir die wunderbare Möglichkeit gab in einer tollen Arbeitsgruppe, an einem interessanten Thema zu arbeiten. Danke Roman für die zahlreichen Diskussionen, in denen Deine Intuition, und diese auch in begreiflichen Bildern umzusetzen, mir stets neue Perspektiven und Verständnis für die physikalischen Zusammenhänge eröffnet haben. Ich habe viel von Dir gelernt.

Henning Moritz möchte ich darüber hinaus nicht nur für das Zweitgutachten danken, sondern auch für seine Begeisterung an der Physik, und seine Fähigkeiten diese an andere lebhaft weiterzugeben. Nicht zuletzt auch an mich.

Der lange Weg bis hierher, die alltägliche Laborarbeit und das Verfassen dieser Arbeit wäre ohne die “Kenner und Könner” nicht möglich gewesen. Danke Jan, Daniela, Axel, Mikhail, Amrit, Lisa, Sebastian, Julian und Pascal. Ohne Euch wäre es niemals so großartig gewesen und trotz kritischer Zeiten habt ihr immer dazu

beigetragen meine gute Laune aufrecht zu erhalten. Ich danke Euch besonders auch dafür, dass Ihr mir den Einstieg als der erste Hamburger in die Arbeitsgruppe so leicht gemacht habt.

Mein ganz besonderer Dank jedoch gilt meiner wundervollen Frau Jasmin. Von ganzem Herzen Danke ich Dir für sehr viel Verständnis und liebevolle Geduld, sowie unglaubliche Unterstützung über all die Jahre. Und damit die Freiheit, das zu tun, was ich tun möchte.

Das soll es fast gewesen sein. Daher nur noch in gewohnter Norddeutscher Zurückhaltung, oder vielmehr das Talent trotz dessen das Wesentliche mit größter Herzlichkeit einsilbig, manchmal auch zweisilbig, auszudrücken:

Danke!

Eidesstattliche Versicherung/ Declaration on oath

Hiermit versichere ich an Eides statt, die vorliegende Dissertationsschrift selbst verfasst und keine anderen als die angegebenen Hilfsmittel und Quellen benutzt zu haben.

Die eingereichte schriftliche Fassung entspricht der auf dem elektronischen Speichermedium.

Die Dissertation wurde in der vorgelegten oder einer ähnlichen Form nicht schon einmal in einem früheren Promotionsverfahren angenommen oder als ungenügend beurteilt.

Hamburg, den 27. Februar 2021

Jascha Zander

Bibliography

[1] W. Heisenberg. “Über quantentheoretische Umdeutung kinematischer und mechanischer Beziehungen”. In: *Zeitschrift für Physik* 33 (1925), pp. 879–893.

[2] E. Abbe. “Beiträge zur Theorie des Mikroskops und der mikroskopischen Wahrnehmung”. In: *Archiv für Mikroskopische Anatomie* 9.1 (Dec. 1873), pp. 413–468. DOI: 10.1007/BF02956173.

[3] M. Born and P. Jordan. “Zur Quantenmechanik”. In: *Zeitschrift für Physik* 34.1 (Dec. 1925), pp. 858–888. DOI: 10.1007/BF01328531.

[4] M. Born, W. Heisenberg, and P. Jordan. “Zur Quantenmechanik. II.” In: *Zeitschrift für Physik* 35.8 (Aug. 1926), pp. 557–615. DOI: 10.1007/BF01379806.

[5] E. H. Kennard. “Zur Quantenmechanik einfacher Bewegungstypen”. In: *Zeitschrift für Physik* 44.4 (Apr. 1927), pp. 326–352. DOI: 10.1007/BF01391200.

[6] H. Weyl. *Gruppentheorie und Quantenmechanik*. S. Hirzel, 1928.

[7] H. P. Robertson. “The Uncertainty Principle”. In: *Phys. Rev.* 34 (1 July 1929), pp. 163–164. DOI: 10.1103/PhysRev.34.163.

[8] E. Schrödinger. “Zum Heisenbergschen Unschärfeprinzip”. In: *Sitzungsberichte der Preussischen Akademie der Wissenschaften, Physikalisch-mathematische Klasse* 14 (1930), pp. 296–303.

[9] R. Schnabel. ““Quantum Weirdness” in Exploitation by the International Gravitational-Wave Observatory Network”. In: *Annalen der Physik* 532.3 (Jan. 2020), p. 1900508. DOI: 10.1002/andp.201900508.

[10] V. B. Braginsky, Y. I. Vorontsov, and K. S. Thorne. “Quantum Nondemolition Measurements”. In: *Science* 209.4456 (1980), pp. 547–557. DOI: 10.1126/science.209.4456.547.

[11] V. B. Braginsky, F. Y. Khalili, and K. S. Thorne. *Quantum Measurement*. Cambridge University Press, 1992. DOI: 10.1017/CBO9780511622748.

[12] A. Einstein, B. Podolsky, and N. Rosen. “Can Quantum-Mechanical Description of Physical Reality Be Considered Complete?” In: *Phys. Rev.* 47 (10 May 1935), pp. 777–780. DOI: 10.1103/PhysRev.47.777.

[13] J. S. Bell. “On the Einstein Podolsky Rosen paradox”. In: *Physics* 1.3 (1964), pp. 195–200. DOI: 10.1103/PhysicsPhysiqueFizika.1.195.

[14] A. Aspect, J. Dalibard, and G. Roger. “Experimental Test of Bell’s Inequalities Using Time-Varying Analyzers”. In: *Phys. Rev. Lett.* 49 (25 Dec. 1982), pp. 1804–1807. DOI: 10.1103/PhysRevLett.49.1804.

[15] E. Schrödinger. “Die gegenwärtige Situation in der Quantenmechanik”. In: *Naturwissenschaften* 50 (Dec. 1935), pp. 844–849. DOI: 10.1007/BF01491987.

[16] G. M. D’Ariano, P. Lo Presti, and M. G. A. Paris. “Using Entanglement Improves the Precision of Quantum Measurements”. In: *Phys. Rev. Lett.* 87 (27 Dec. 2001), p. 270404. DOI: 10.1103/PhysRevLett.87.270404.

[17] R. E. Slusher, L. W. Hollberg, B. Yurke, J. C. Mertz, and J. F. Valley. “Observation of Squeezed States Generated by Four-Wave Mixing in an Optical Cavity”. In: *Phys. Rev. Lett.* 55 (22 Nov. 1985), pp. 2409–2412. DOI: 10.1103/PhysRevLett.55.2409.

[18] L.-A. Wu, H. J. Kimble, J. L. Hall, and H. Wu. “Generation of Squeezed States by Parametric Down Conversion”. In: *Phys. Rev. Lett.* 57 (20 Nov. 1986), pp. 2520–2523. DOI: 10.1103/PhysRevLett.57.2520.

[19] H. Vahlbruch, M. Mehmet, S. Chelkowski, et al. “Observation of Squeezed Light with 10-dB Quantum-Noise Reduction”. In: *Phys. Rev. Lett.* 100 (3 Jan. 2008), p. 033602. DOI: 10.1103/PhysRevLett.100.033602.

[20] T. Eberle. "Realization of Finite-Size Quantum Key Distribution Based on Einstein-Podolsky-Rosen Entangled Light". PhD thesis. Leibniz University Hannover, 2013.

[21] A. Schönbeck, F. Thies, and R. Schnabel. "13 dB squeezed vacuum states at 1550nm from 12mW external pump power at 775nm". In: *Opt. Lett.* 43.1 (Jan. 2018), pp. 110–113. DOI: 10.1364/OL.43.000110.

[22] H. Vahlbruch, M. Mehmet, K. Danzmann, and R. Schnabel. "Detection of 15 dB Squeezed States of Light and their Application for the Absolute Calibration of Photoelectric Quantum Efficiency." In: *Physical review letters* 117 11 (2016), p. 110801.

[23] C. M. Caves. "Quantum-mechanical noise in an interferometer". In: *Phys. Rev. D* 23 (8 Apr. 1981), pp. 1693–1708. DOI: 10.1103/PhysRevD.23.1693.

[24] R. Schnabel. "Squeezed states of light and their applications in laser interferometers". In: *Physics Reports* 684 (Apr. 2017), pp. 1–51. DOI: 10.1016/j.physrep.2017.04.001.

[25] J. Abadie, B. P. Abbott, R. Abbott, et al. "A gravitational wave observatory operating beyond the quantum shot-noise limit". In: *Nature Physics* 7.12 (Dec. 2011), pp. 962–965. DOI: 10.1038/nphys2083.

[26] H. Grote, K. Danzmann, K. L. Dooley, et al. "First Long-Term Application of Squeezed States of Light in a Gravitational-Wave Observatory". In: *Phys. Rev. Lett.* 110 (18 May 2013), p. 181101. DOI: 10.1103/PhysRevLett.110.181101.

[27] R. Schnabel, N. Mavalvala, D. E. McClelland, and P. K. Lam. "Quantum metrology for gravitational wave astronomy". In: *Nature Communications* 1.1 (Nov. 2010), p. 121. DOI: 10.1038/ncomms1122.

[28] M. Tse, H. Yu, N. Kijbunchoo, et al. "Quantum-Enhanced Advanced LIGO Detectors in the Era of Gravitational-Wave Astronomy". In: *Phys. Rev. Lett.* 123 (23 Dec. 2019), p. 231107. DOI: 10.1103/PhysRevLett.123.231107.

[29] F. Acernese, M. Agathos, L. Aiello, et al. “Increasing the Astrophysical Reach of the Advanced Virgo Detector via the Application of Squeezed Vacuum States of Light”. In: *Phys. Rev. Lett.* 123 (23 Dec. 2019), p. 231108. DOI: 10.1103/PhysRevLett.123.231108.

[30] M. Taylor, J. Janousek, V. Daria, et al. “Biological measurement beyond the quantum limit”. In: *Nature Photonics* 7 (June 2012). DOI: 10.1038/nphoton.2012.346.

[31] R. Bruzaca, H. Kerdoncuff, K. Berg-Sørensen, et al. “Quantum-Enhanced continuous-wave stimulated Raman spectroscopy”. In: *Optica* 7 (Apr. 2020). DOI: 10.1364/OPTICA.386584.

[32] H. M. Wiseman, S. J. Jones, and A. C. Doherty. “Steering, Entanglement, Nonlocality, and the Einstein-Podolsky-Rosen Paradox”. In: *Phys. Rev. Lett.* 98 (14 Apr. 2007), p. 140402. DOI: 10.1103/PhysRevLett.98.140402.

[33] L. S. Madsen, V. C. Usenko, M. Lassen, R. Filip, and U. L. Andersen. “Continuous variable quantum key distribution with modulated entangled states”. In: *Nature Communications* 3.1 (Sept. 2012), p. 1083. DOI: 10.1038/ncomms2097.

[34] T. Gehring, V. Händchen, J. Duhme, et al. “Implementation of continuous-variable quantum key distribution with composable and one-sided-device-independent security against coherent attacks”. In: *Nature Communications* 6.1 (Oct. 2015), p. 8795. DOI: 10.1038/ncomms9795.

[35] B. Julsgaard, J. Sherson, J. I. Cirac, J. Fiurášek, and E. S. Polzik. “Experimental demonstration of quantum memory for light”. In: *Nature* 432.7016 (Nov. 2004), pp. 482–486. DOI: 10.1038/nature03064.

[36] K. Jensen, W. Wasilewski, H. Krauter, et al. “Quantum memory for entangled continuous-variable states”. In: *Nature Physics* 7.1 (Nov. 2010), pp. 13–16. DOI: 10.1038/nphys1819.

[37] B. Hage, A. Samblowski, J. DiGuglielmo, et al. “Preparation of distilled and purified continuous-variable entangled states”. In: *Nature Physics* 4.12 (Nov. 2008), pp. 915–918. DOI: 10.1038/nphys1110.

[38] D. Abdelkhalek, M. Syllwasschy, N. J. Cerf, J. Fiurášek, and R. Schnabel. “Efficient entanglement distillation without quantum memory”. In: *Nature Communications* 7.1 (May 2016), p. 11720. DOI: 10.1038/ncomms11720.

[39] C. Gerry, P. Knight. *Introductory Quantum Optics*. Cambridge University Press, 2005.

[40] C. M. Caves and B. L. Schumaker. “New formalism for two-photon quantum optics. I. Quadrature phases and squeezed states”. In: *Phys. Rev. A* 31 (5 May 1985), pp. 3068–3092. DOI: 10.1103/PhysRevA.31.3068.

[41] B. L. Schumaker and C. M. Caves. “New formalism for two-photon quantum optics. II. Mathematical foundation and compact notation”. In: *Phys. Rev. A* 31 (5 May 1985), pp. 3093–3111. DOI: 10.1103/PhysRevA.31.3093.

[42] S. Steinlechner. “Quantum metrology with squeezed and entangled light for the detection of gravitational waves”. PhD thesis. University of Hanover, 2013.

[43] R. J. Glauber. “Coherent and Incoherent States of the Radiation Field”. In: *Phys. Rev.* 131 (6 Sept. 1963), pp. 2766–2788. DOI: 10.1103/PhysRev.131.2766.

[44] J. J. Sakurai. *Modern quantum mechanics; rev. ed.* Reading, MA: Addison-Wesley, 1994.

[45] M. D. Reid. “Demonstration of the Einstein-Podolsky-Rosen paradox using nondegenerate parametric amplification”. In: *Phys. Rev. A* 40 (2 July 1989), pp. 913–923. DOI: 10.1103/PhysRevA.40.913.

[46] S. Chelkowski. “Squeezed Light and Laser Interferometric Gravitational Wave Detectors”. PhD thesis. University of Hanover, 2007.

[47] T. Eberle, V. Händchen, and R. Schnabel. “Stable control of 10 dB two-mode squeezed vacuum states of light”. In: *Opt. Express* 21.9 (May 2013), pp. 11546–11553. DOI: 10.1364/OE.21.011546.

[48] B. Yurke. “Use of cavities in squeezed-state generation”. In: *Phys. Rev. A* 29 (1 Jan. 1984), pp. 408–410. DOI: 10.1103/PhysRevA.29.408.

[49] G. Milburn and D. F. Walls. “Production of squeezed states in a degenerate parametric amplifier”. In: *Optics Communications* 39.6 (Nov. 1981), pp. 401–404. DOI: 10.1016/0030-4018(81)90232-7.

[50] M. J. Collett and C. W. Gardiner. “Squeezing of intracavity and traveling-wave light fields produced in parametric amplification”. In: *Phys. Rev. A* 30 (3 Sept. 1984), pp. 1386–1391. DOI: 10.1103/PhysRevA.30.1386.

[51] J. Bauchrowitz, T. Westphal, and R. Schnabel. “A graphical description of optical parametric generation of squeezed states of light”. In: *American Journal of Physics* 81.10 (Oct. 2013), pp. 767–771. DOI: 10.1119/1.4819195.

[52] M. M. Fejer, G. A. Magel, D. H. Jundt, and R. L. Byer. “Quasi-phase-matched second harmonic generation: tuning and tolerances”. In: *IEEE Journal of Quantum Electronics* 28.11 (1992), pp. 2631–2654. DOI: 10.1109/3.161322.

[53] E. D. Black. “An introduction to Pound–Drever–Hall laser frequency stabilization”. In: *Am. J. Phys.* 69.1 (Jan. 2000), pp. 79–87.

[54] Y. Arosa, E. L. Lago, L. M. Varela, and R. de la Fuente. “Spectrally resolved white light interferometry to measure material dispersion over a wide spectral band in a single acquisition”. In: *Opt. Express* 24 (15 July 2016), pp. 17303–17312. DOI: 10.1364/OE.24.017303.

[55] M. Chen, S. Xie, H. Wu, et al. “Absolute distance measurement; Diffraction gratings; Fast Fourier transforms; Light beams; Optical coherence tomography; Tunable lasers”. In: *Opt. Express* 27 (8 Apr. 2019), pp. 10553–10563. DOI: 10.1364/OE.27.010553.

[56] D. V. Martynov, E. D. Hall, B. P. Abbott, R. Abbott, and T. D. Abbott. “Sensitivity of the Advanced LIGO detectors at the beginning of gravitational wave astronomy”. In: *Physical Review D* 93.11 (June 2016). DOI: 10.1103/physrevd.93.112004.

[57] Abernathy, M. et al. *Einstein gravitational wave telecope conceptual design study*. http://www.et-gw.eu/index.php/etdsdocument. Online; accessed 21 F 2020.

[58] R. Schnabel, M. Britzger, F. Brückner, et al. “Building blocks for future detectors: Silicon test masses and 1550 nm laser light”. In: *Journal of Physics: Conference Series* 228 (May 2010), p. 012029. DOI: 10.1088/1742-6596/228/1/012029.

[59] M. Punturo, M. Abernathy, F. Acernese, et al. “The third generation of gravitational wave observatories and their science reach”. In: *Classical and Quantum Gravity* 27.8, 084007 (Apr. 2010), p. 084007. DOI: 10.1088/0264-9381/27/8/084007.

[60] R. Demkowicz-Dobrzański, M. Jarzyna, and J. Kołodyński. “Quantum Limits in Optical Interferometry”. In: *Progress in Optics* (2015), pp. 345–435. DOI: 10.1016/bs.po.2015.02.003.

[61] B. Yurke, S. L. McCall, and J. R. Klauder. “SU(2) and SU(1,1) interferometers”. In: *Phys. Rev. A* 33 (6 June 1986), pp. 4033–4054. DOI: 10.1103/PhysRevA.33.4033.

[62] C. M. Caves. “Reframing SU(1,1) Interferometry”. In: *Advanced Quantum Technologies* 3.11 (Mar. 2020), p. 1900138. DOI: 10.1002/qute.201900138.

[63] M. Kitagawa and M. Ueda. “Squeezed spin states”. In: *Phys. Rev. A* 47 (6 June 1993), pp. 5138–5143. DOI: 10.1103/PhysRevA.47.5138.

[64] D. J. Wineland, J. J. Bollinger, W. M. Itano, and D. J. Heinzen. “Squeezed atomic states and projection noise in spectroscopy”. In: *Phys. Rev. A* 50 (1 July 1994), pp. 67–88. DOI: 10.1103/PhysRevA.50.67.

[65] A. Sørensen, L.-M. Duan, J. I. Cirac, and P. Zoller. “Many-particle entanglement with Bose–Einstein condensates”. In: *Nature* 409.6816 (Jan. 2001), pp. 63–66. DOI: 10.1038/35051038.

[66] M. Taylor and W. Bowen. “Quantum metrology and its application in biology”. In: *Physics Reports* 615 (Sept. 2014). DOI: 10.1016/j.physrep.2015.12.002.

[67] E. Knyazev, F. Y. Khalili, and M. V. Chekhova. "Overcoming inefficient detection in sub-shot-noise absorption measurement and imaging". In: *Optics Express* 27.6 (Mar. 2019), p. 7868. DOI: 10.1364/oe.27.007868.

[68] P.-A. Moreau, J. Sabines-Chesterking, R. Whittaker, et al. "Demonstrating an absolute quantum advantage in direct absorption measurement". In: *Scientific Reports* 7 (Nov. 2016). DOI: 10.1038/s41598-017-06545-w.

[69] A. Crespi, M. Lobino, J. C. F. Matthews, et al. "Measuring protein concentration with entangled photons". In: *Applied Physics Letters* 100.23 (June 2012), p. 233704. DOI: 10.1063/1.4724105.

[70] S. Dante, A. B. González-Guerrero, K. Zinoviev, et al. "Towards a complete Lab-On-Chip system using integrated Mach-Zehnder interferometers". In: *Optica Pura y Aplicada* 45 (June 2012), pp. 87–95. DOI: 10.7149/OPA.45.2.87.

[71] D. Bouwmeester, J.-W. Pan, K. Mattle, et al. "Experimental quantum teleportation". In: *Nature* 390.6660 (Dec. 1997), pp. 575–579. DOI: 10.1038/37539.

[72] A. Furusawa, J. L. Sørensen, S. L. Braunstein, et al. "Unconditional Quantum Teleportation". In: *Science* 282.5389 (1998), pp. 706–709. DOI: 10.1126/science.282.5389.706.

[73] W. P. Bowen, N. Treps, B. C. Buchler, et al. "Experimental investigation of continuous-variable quantum teleportation". In: *Physical Review A* 67.3 (Mar. 2003). DOI: 10.1103/physreva.67.032302.

[74] S. Steinlechner, J. Bauchrowitz, M. Meinders, et al. "Quantum-Dense Metrology". In: *Nature Photonics* 7 (Nov. 2012). DOI: 10.1038/nphoton.2013.150.

[75] E. S. Polzik and K. Hammerer. "Trajectories without quantum uncertainties". In: *Annalen der Physik* 527.1-2 (2015), A15–A20. DOI: 10.1002/andp.201400099.

[76] D. Leibfried, M. Barrett, T. Schaetz, et al. "Toward Heisenberg-Limited Spectroscopy with Multiparticle Entangled States". In: *Science (New York, N.Y.)* 304 (July 2004), pp. 1476–8. DOI: 10.1126/science.1097576.

[77] W. Wasilewski, K. Jensen, H. Krauter, et al. "Quantum Noise Limited and Entanglement-Assisted Magnetometry". In: *Physical Review Letters* 104.13 (Mar. 2010). DOI: 10.1103/physrevlett.104.133601.

[78] C. Gross, T. Zibold, E. Nicklas, J. Estève, and M. K. Oberthaler. "Nonlinear atom interferometer surpasses classical precision limit". In: *Nature* 464.7292 (Mar. 2010), pp. 1165–1169. DOI: 10.1038/nature08919.

[79] E. Arthurs and J. L. Kelly. "B.S.T.J. briefs: On the simultaneous measurement of a pair of conjugate observables". In: *The Bell System Technical Journal* 44.4 (Apr. 1965), pp. 725–729. DOI: 10.1002/j.1538-7305.1965.tb01684.x.

[80] K. Husimi. "Some Formal Properties of the Density Matrix". In: *Proc. Phys. Math. Soc. Jpn. 22, 264* (1940).

[81] N. Bohr. "Can Quantum-Mechanical Description of Physical Reality be Considered Complete?" In: *Phys. Rev.* 48 (8 Oct. 1935), pp. 696–702. DOI: 10.1103/PhysRev.48.696.

[82] V. Händchen. "Experimental Analysis of Einstein-Podolsky-Rosen Steering for Quantum Information Applications". PhD thesis. University of Hannover, 2016.

[83] E. Schrödinger. "Quantisierung als Eigenwertproblem". In: *Annalen der Physik* 384.4 (1926), pp. 361–376.